UNIVERSITY OF CALIFORNIA
SANTA CRUZ

HIGH-PRESSURE STUDIES OF SUBDUCTION ZONE RELATED MINERAL PHASES

A dissertation submitted in partial satisfaction
of the requirements for the degree

DOCTOR OF PHILOSOPHY

in

EARTH SCIENCES

by

Earl F. O'Bannon III

September 2017

The Dissertation of Earl F. O'Bannon III is approved:

Professor Quentin Williams, chair

Professor Susan Schwartz

Associate Professor Jeremy Hourigan

Tyrus Miller
Vice Provost and Dean of Graduate Studies

List of Figures

List of Tables

Abstract

High-pressure studies of subduction zone related mineral phases

By

Earl F. O'Bannon III

Subduction zones play a fundamental role in the cycling of minerals from the surface of the Earth into the deep Earth. Minerals that are subducted experience high-pressure and temperature as they are transported to greater and greater depths. The work presented here takes advantage of pressure as a thermodynamic variable in order to gain insight into the physics and chemistry of subduction zone related mineral phases.

The experiments conducted here use the diamond anvil cell at pressures up to ~65 GPa in conjunction with synchrotron based single-crystal x-ray diffraction as well as Raman, infrared, and luminescence spectroscopy. The work is divided into three major parts (1) water bearing minerals found in subduction zones such as lawsonite [$CaAl_2Si_2O_7(OH)_2 \cdot H_2O$] and clinochlore [$Mg_5Al(AlSi_3O_{10})(OH)_8$], (2) B and F bearing minerals found in subduction zones such as topaz [$Al_2SiO_4(F,OH)_2$], and dravite variety tourmaline [$Na(Mg_3)Al_6(Si_6O_{18}(BO_3)_3(OH)_3(OH)$] and (3) mineral phases that are closely related to subduction zone minerals but not likely found in abundance in subduction zones such as beryl [$Be_3Al_2Si_6O_{18}$], and spodumene [$LiAlSi_2O_6$].

The high-pressure crystal structure of lawsonite was solved for the first time using synchrotron based single-crystal x-ray diffraction. The H-bonding environment

of the high-pressure monoclinic phase of lawsonite was also determined. High-pressure luminescence spectra of clinochlore up to ~25 GPa show that the electronic properties of this sheet silicate are complex under high-pressure conditions. High-pressure luminescence spectra of topaz up to ~55 GPa show that the deformation mechanism of topaz likely changes above ~38 GPa. A new high-pressure phase of tourmaline that is stable above ~15 GPa at room temperature was discovered and solved using synchrotron based single-crystal x-ray diffraction. Luminescence spectra suggest this phase is stable to at least ~65 GPa.

A new high-pressure phase of beryl that is stable above ~14 GPa at room temperature was discovered using luminescence and Raman spectroscopy. Experimentally our results confirm the previous theoretically predicted high-pressure soft-mode transition. Beryl is structurally related to the high-temperature phase of cordierite [$(Mg,Fe)_2Al_3(AlSi_5O_{18})$], a subduction zone mineral phase that shows extensive high-pressure polymorphism. Spodumene is certainly not abundant in the Earth's crust and upper mantle, however understanding high-pressure phase transitions in C2/c pyroxenes is important for understanding the high-pressure behavior of mantle relevant pyroxenes (e.g. hedenbergite [$CaFeSi_2O_6$] and diopside [$CaMgSi_2O_6$]). Luminescence spectra suggest that only one transition at 3.2 GPa occurs under compression from room pressure to ~15 GPa which is in contrast to previous work that suggests a second transition near 7.7 GPa.

To my parents, for all their love and support.

Acknowledgements

This is the hardest part to write primarily because I am deathly afraid that I will fail to acknowledge everyone that has made this grueling five-year task possible. I will attempt to acknowledge everyone that has helped me along the way and if I leave someone out it is not on purpose.

First and foremost, I must acknowledge everyone that ever had to listen to me talk about trona. Secondly, my advisor Quentin C. Williams, whom apparently "really hated" mineralogy in college, and if I had known that I may have chosen a different path to graduate school. Nonetheless, I started my graduate work at UCSC in Sept. of 2012 with absolutely no idea the journey I was about to embark upon. As I developed research ideas of my own (and possibly became a more annoying student) Quentin was always there to steer me in the correct direction so that I would not end up too far down a rabbit hole (although I am not sure he did so well keeping me away from luminescence studies...). I admire your dedication to any project as long as you have new spectra to look at (or drool over). Our working relationship has evolved over the last five years and your mentorship and guidance has made me a better person and scientist. Thank you.

A large portion of this work would not have been possible without the tireless support of the staff at beamline 12.2.2 at the Advanced Light Source in Berkeley CA. Christine Beavers, Martin Kunz, Jinyuan Yan, and Andrew Doran. I apologize for the late calls when things go wrong, as well as the time I drove Chi2 to zero (although that was within both hardware and software limits). I learned a lot about single-crystal

diffraction, bond valence analysis, gas loaders, and externally heated diamond anvil cells. My last two years as an ALS doctoral fellow has been key in my development as a scientist it provided me the opportunity to acquire a lot of additional beamtime as well as PhD mentoring time at the climbing gym. I must also acknowledge my Beamline 11.3.1 family, Simon Teat, Laura McCormick, and Nico Girodano whom have all taught me more about single-crystal diffraction, and have had to listen to me talk about minerals at some point. All of you have been mentors and friends along the way and without your support this would have been a much longer journey. I must acknowledge the excellent UCSC technical staff, Dan Sampson and Rob Franks, for help with the analytical equipment that I used for some of my research.

I am grateful to have started graduate school with a cohort that was unusually close knit. We did everything together for the first several years and as the sole student in my lab for the first two years this was invaluable mental and emotional support for me. I must thank all of them for listening to me talk about trona and chromium for hours and hours. In 2014 Cara Vennari joined the mineral physics lab and provided much needed support during beamtime (she would run the night shift) as well as additional comic relief (which the lab already had in spades). Cara brought her chemistry background into the lab which meant I was now surrounded by two people with a chemistry background and Christine brought that number to three. Being this close to a large number of chemists forced me to learn more chemistry and has made me a better scientist.

To Camelia Stan, who has most likely had to listen to me talk about work more than anyone else. We met during a short course on X-ray diffraction, and I did not know at the time that she would become my closest friend and partner. Playing the role of colleague can be difficult, but you have made me a better scientist, you have supported me when I wavered, and you have shared my victories. More recently you have provided me with many dirty dishes to clean, however the quality of my dinners has vastly improved. Words cannot express my gratitude. Thank You.

I want to thank my parents Earl and Carol O'Bannon for always supporting me in all my endeavors from joining the military, to going to college, deploying to Iraq (they were not super enthusiastic about this one), and eventually going to graduate school. To my brother Andrew O'Bannon for supporting me along the way and going camping with me when he could since he enjoys the desert as much as I do. Without your support this would have been truly difficult and there are not enough words to express my gratitude. Thank you.

Published content and contributions

O'Bannon, E., & Williams, Q. (2017). Delocalization in Cr 3+ luminescence of clinochlore: A pressure-induced transition from single-ion emission to pair emission. *Journal of Physics and Chemistry of Solids*. (In Press).

O'Bannon, E.F. and Williams, Q. (2016) A Cr^{3+} luminescence study of spodumene at high pressure: Effects of site geometry, a phase transition, and a level crossing, *American Mineralogist*, 101, 1406-1413.

O'Bannon, E.F. and Williams, Q., (2016) Beryl-II, a high-pressure phase of beryl: Raman and luminescence spectroscopy to 16.4 GPa, *Physics and Chemistry of Minerals, 43,671-687.*

Chapter 1

Introduction

Cycling of elements between the crust and the mantle occurs at subduction zones (Figure 1.1). Subduction zones are areas where variably hydrated oceanic crust which can be capped with sediments descends into the mantle. At shallow depths, <10 to 40 km, subduction zone processes are relatively well constrained (Peacock 1990). At intermediate depths of 80 to 150 km most of what we know about the magma generation, back arc volcanism and mineral dehydration reactions is based on petrologic studies (Peacock 1990; Pawley 1994; Schmidt and Poli 1994, 1998; Poli and Schmidt 1995; Schmidt 1995; Holland et al. 1996; Ono 1998). Our understanding or processes at depths > 150 km is limited since geologic samples from this region are rare, and experiments in this pressure and temperature regime are difficult.

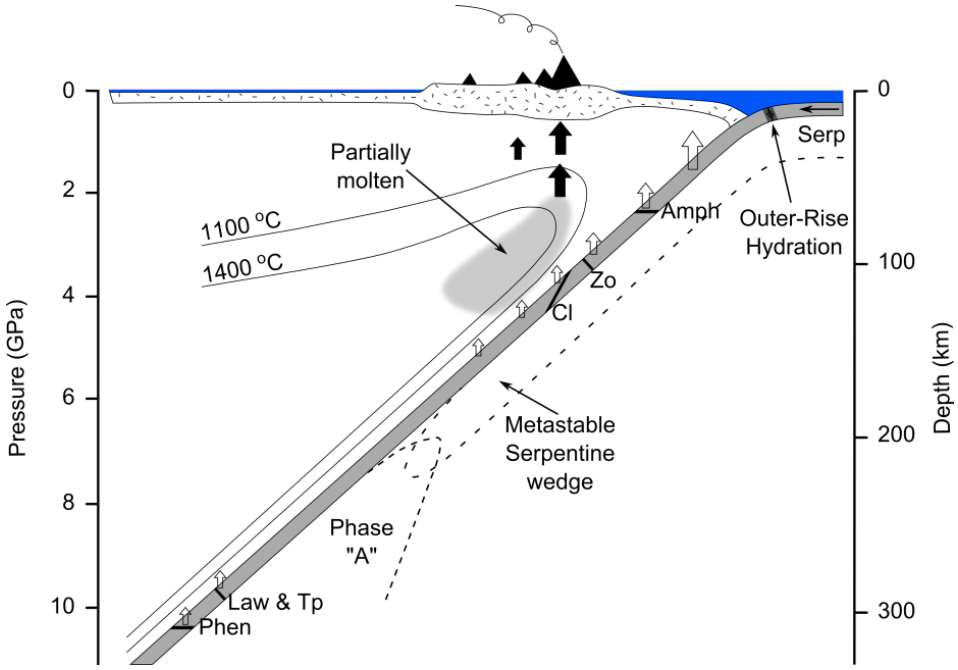

Figure 1.1 Simplified schematic diagram of a subduction zone showing the pressure and depth conditions of typical mineral dehydration reactions. Open arrows indicate the rise of fluid, and solid arrows indicate the rise of magma. Modified from (Schmidt and Poli 1998) with topaz data from (Wunder et al. 1993).

1.1 Deep Earth water cycle

For chapters 2 and 3, I studied two hydrated aluminosilicates lawsonite [$CaAl_2Si_2O_7(OH)_2 \cdot H_2O$] and clinochlore [$Mg_5Al(AlSi_3O_{10})(OH)_8$]. The deep Earth water cycle is complex, and amount of water contained within our planet, and how it is distributed remains uncertain (for more detailed information on the deep Earth water cycle see review papers by Williams and Hemley 2001; Hirschmann 2006). Significant amounts of water are transported into the mantle by subduction zones in minerals within oceanic crust and continentally derived meta-sediments (Ono 1998; Chinnery et al. 2000; Dobrzhinetskaya and Green 2007). Figure 1.1 shows a simplified diagram of a typical subduction zone. Water affects the chemical and physical properties of materials by lowering solidus temperatures, which allows for partial melting of mantle material under relatively low temperature, and by altering rheological properties. Thus, understanding the high-pressure polymorphism of water bearing subduction zone minerals is key in interpreting subduction zone processes like partial melting and magma generation. The transport of water in minerals to great depths in subduction zones is no longer in question (Pawley 1994; Poli and Schmidt 1995, 2002; Pawley et al. 1996). However other questions remain unanswered, and include: (1) how does hydrogen bonding change under high-pressure conditions, (2) what is the crystal structure of the high-pressure phase(s) and (3) are there high-pressure phases that have not yet been found?

Lawsonite is a unique mineral that has a high overall water content and a large pressure/temperature stability field. It is believed to be one of the few minerals that could transport water to depths of > 300km. Using synchrotron based single-crystal x-ray diffraction I was able to solve for the first time the high-pressure monoclinic structure of lawsonite. The structural transition is driven by the O1 atom and involves a slight distortion of the aluminosilicate framework and a re-orientation of both the H2O molecule and hydroxyls. The high-pressure structure confirms the earlier spectroscopic results and powder diffraction results of Scott and Williams (1999), Daniel et al. (2000), and Pawley and Allan (2001). Clinochlore is a TOT + O sheet silicate that has a high overall water content and is abundant in subduction zones. I used Cr^{3+} luminescence spectroscopy to investigate the known ~6.0 GPa polytypic phase transition reported by Kleppe et al. (2003) and Welch and Crichton (2005). This study quickly evolved into an interesting story of pressure induced electron delocalization which led to a transition from single-ion emission to paired-ion emission.

1.2 Deep Earth B and F cycling

For chapters 3 and 4, I studied topaz [$Al_2SiO_4(F,OH)_2$] an F bearing phase, and dravite variety tourmaline [$Na(Mg_3)Al_6(Si_6O_{18}(BO_3)_3(OH)_3(OH)$] a B bearing phase. B and F are useful tracers to investigate crustal cycling in subduction zones and are potentially useful in understating the transport and evolution of arc magmas (Bebout and Nakamura 2003; Ota et al. 2008; John et al. 2011; Kendrick et al. 2015; Van den Bleeken and Koga 2015; Pagé et al. 2016). Most of the reported studies are

focused on constraining isotope fractionation between fluids and minerals in order to understand cycling of B and F in the deep Earth. Experiments on mineral phases that contain several weight % B or F at pressures greater than 5 GPa are scarce. Hence our understating of structural response of mineral phases with high concentrations of B or F under high-pressures is limited.

Topaz is one of the few phases that could transport F to great depths in subduction zones. It has been previously studied with high-pressure single-crystal diffraction up to ~45 GPa and phase transitions and changes in deformation mechanisms were not reported (Gatta et al. 2006, 2014). This is in contrast to our high-pressure Cr^{3+} luminescence results which suggest that there is a change in compression mechanism above ~38 GPa. Tourmaline is a chemically complex mineral, which is present in subduction zones (Nakano and Nakamura 2001; Bebout and Nakamura 2003) and is one of the few minerals that transport B to depth. Only two previous powder diffraction studies have been reported and phase transitions were not observed up to ~26 GPa (Li et al. 2004; Xu et al. 2016). I studied dravite variety tourmaline under high-pressure with both Cr^{3+} luminescence spectroscopy and synchrotron based single-crystal x-ray diffraction. A subtle peak splitting of the Cr^{3+} ^2E emission band occurs near 15 GPa, and above that pressure the high-pressure structure appears to be stable up to at least ~65 GPa. Single-crystal data show that a rhombohedral R3m to R3 phase transition occurs near 15 GPa. High-pressure phase transitions have not been reported for tourmaline, and the onset pressure of this phase transition is expected to be compositionally dependent.

1.3 Analogue subduction zone minerals

Finally, for my last two chapters I studied beryl [$Be_3Al_2Si_6O_{18}$] and spodumene [$LiAlSi_2O_6$] which are structurally related to mineral phases that are found in abundance in subduction zones. Analog materials can be studied in order to understand material properties or access phase transitions which are experimentally difficult to access. The classic geosciences example is the substitution of Ge for Si in minerals to study phase transitions (Ringwood and Seabrook 1963; Navrotsky and Hughes 1976; Akaogi et al. 2005; Stan et al. 2017) and rheological properties (Burnley et al. 1991; Merkel et al. 2006). Difluorides and dichlorides have been found to be good analogs for the high-pressure behavior of oxides due to their lower transition pressures (Leger et al. 1996; Stan et al. 2016). SiO_2 has been theoretically predicted to adopt the cotunnite structure at pressures > 700 GPa (Oganov et al. 2005), a pressure not accessible with static compression techniques.

Beryl is structurally related to the high-temperature phase of cordierite [$(Mg,Fe)_2Al_3(AlSi_5O_{18})$]. Cordierite is found in subduction zones and exhibits extensive high-pressure polymorphism (Finkelstein et al. 2015). The main difference between beryl and cordierite is that cordierite typically has a larger amount of tetrahedrally coordinated aluminum. High-pressure Raman and luminescence spectra experimentally confirm the theoretically predicted soft-mode transition in beryl near 14 GPa. Spodumene [$LiAlSi_2O_6$] crystallizes in the same spacegroup as the mantle relevant pyroxenes hedenbergite [$CaFeSi_2O_6$] and diopside [$CaMgSi_2O_6$]. Using Cr^{3+} luminescence spectroscopy I found that under compression to ~15 GPa only one

phase transition occurs. This is in contrast to one previous study which reports two phase transitions under compression to ~15 GPa.

Chapter 2

The high-pressure phase of lawsonite: A single crystal study of a key mantle hydrous phase

2.1 Introduction

Significant amounts of water are transported into the mantle by subduction zones in the form of hydrated minerals in oceanic crust and continentally derived meta-sediments (Ono 1998; Chinnery et al. 2000; Dobrzhinetskaya and Green 2007). This water affects the chemical and physical properties of materials by lowering their solidus temperatures, which allows for partial melting of mantle material at relatively low temperatures, and by altering rheological properties. Water reservoirs in subducted oceanic crust and its overlying sediments include chloritoid, lawsonite, topaz, serpentines, chlorite (clinochlore), zoisite, amphiboles and micas. Lawsonite is particularly interesting because of its high overall water content, ~11.5 wt.% (Baur 1978), large stability field, and its prevalence in fully hydrated mid-ocean ridge basalt (MORB) at pressure, which contains 7-15 wt% lawsonite (Schmidt and Poli 1998). Lawsonite and phengitic mica are thought to be the dominant water carriers in subducted crust from ~200 to over 300 km depth, which corresponds to pressures of ~7-10 GPa (Pawley 1994; Schmidt and Poli 1994; Domanik and Holloway 1996). The way that H_2O molecules and OH groups are contained within the lawsonite structure is unusual (Figure 2.1). H_2O molecules reside in cavities that are formed by rings of two Si_2O_7 groups and two Al-octahedra. These cavities are not completely open channels, like the channels typically found in ring silicates (e.g. cordierite), but

the channels in lawsonite also contain the large Ca ion, bound to the ring framework, in addition to the water molecule. The OH groups are contained within a much smaller channel in the structure formed by two AlO_6 octahedra and two SiO_4 tetrahedra.

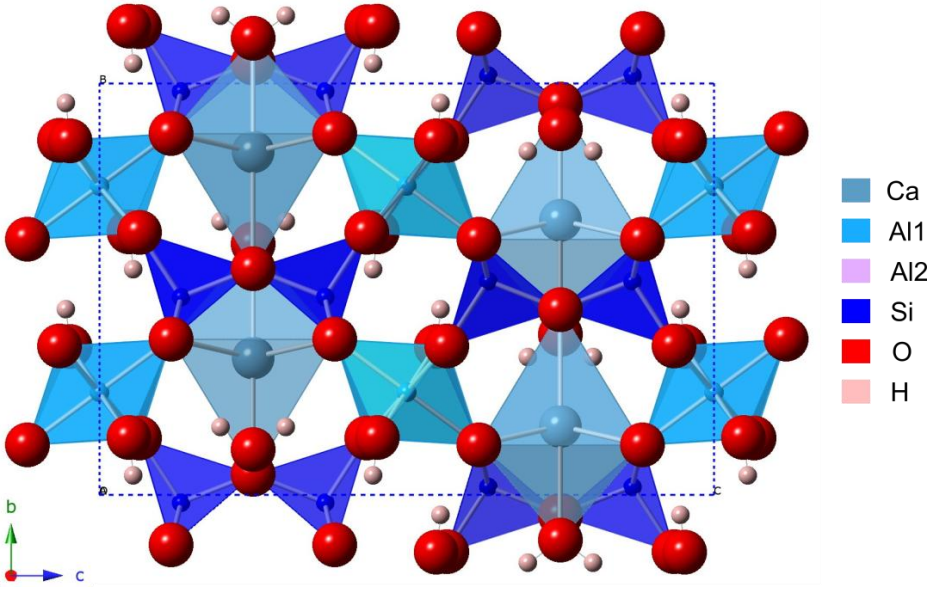

Figure 2.1. Room pressure and temperature structure of lawsonite looking along the *a*-axis. Atom colors are the same in all structural figures. All structural diagrams were generated using CrystalMaker ® v.8.7.6.

Lawsonite undergoes two low temperature phase transitions at -118 and 0 °C at ambient pressure that involve changes in the hydrogen bonding of the H_2O and OH groups (Libowitzky and Armbruster 1995), and to a lesser extent changes in the aluminosilicate framework. However, no phase transitions are observed upon heating to ~600 ^{o}C (Pawley et al. 1996). Notably, the H atoms of the H_2O and OHs in lawsonite are dynamically disordered and oscillate between two equivalent sites, and the low temperature phase transitions are interpreted to be generated by a freezing in

of the dynamic hopping motions of the H atoms (Libowitzky and Armbruster 1995; Libowitzky 2009). High pressure, room temperature single-crystal diffraction structures have been reported up to ~3.78 GPa (Comodi and Zanazzi 1996) and no phase transitions were reported in this pressure range. An additional phase transition at ~4 GPa from orthorhombic C to an orthorhombic P space group was reported by Ballaran and Angel (2003) using single-crystal diffraction, but they could not determine the structure and space group of this phase. If accurate, the presence of this unsolved transition in symmetry would imply that we do not know the structure of the major water carrier in basalt at depths greater than ~120 km.

At higher pressures, Scott and Williams (1999) reported a discontinuous shift in the O-H stretching vibrations at ~8-9 GPa in the high-pressure infrared spectra of lawsonite. Daniel et al. (2000) reported a phase transition at ~8.6 GPa using Raman spectroscopy and powder diffraction, and Pawley and Allan (2001) observed the same transition at ~10-11 GPa using powder diffraction. This transition, from orthorhombic to monoclinic symmetry, has now been known, for ~16 years, to occur between ~8.6 and ~11 GPa (Daniel et al. 2000; Pawley and Allan 2001; Ballaran and Angel 2003).

Structural determinations of the proposed orthorhombic P phase (> 4 GPa) and the monoclinic P phase have not been reported, and both of these transitions occur at pressures relevant to subduction zones. Pawley and Allan (2001) reported a Rietveld refinement of the $P2_1/m$ structure of monoclinic lawsonite using the orthorhombic *Cmcm* structure as their starting model. The P-T slope of this phase transition is poorly constrained, and Pawley and Allan (2001) hypothesize that this

transition has a shallow positive slope. If this were the case, the high-pressure phase of lawsonite would be unlikely to be stable under conditions found within subduction zones. However, Pawley and Allan (2001) also explicitly state that a negative slope cannot be ruled out, which would intersect the temperature field within colder subducted slabs. Moreover, the high-pressure phase of lawsonite almost certainly has higher entropy since the oxygen position, O2, splits into two separate sites in the monoclinic structure , O2A and O2B, and the cation site M1 splits into M1A and M1B (e.g. Liebscher et al., 2010; Pawley and Allan, 2001). Hence, $\Delta S_{\text{ortho-mono}}$ is anticipated to be positive, and $\Delta V_{\text{ortho-mono}}$ is small but negative (e.g. Ballaran and Angel, 2003; Daniel et al., 2000; Pawley and Allan, 2001), which indicates that the slope of the *Cmcm*-$P2_1/m$ transition must be negative. From this it follows that the high-pressure monoclinic phase of lawsonite could be the dominant water carrier in basalts carried by deep, rapidly subducted, older slabs, and thus may be of considerable importance for moving water to depths deeper than 300 km (~10 GPa), and approaching the top of the transition zone.

High quality single-crystal structural determinations of the high-pressure phase(s) of the dominant carrier of water to depths of ~300 km in subducted basalt (Schmidt and Poli 1998) and in hydrated metamorphic assemblages associated with subduction (Vitale Brovarone and Beyssac 2014) have thus not yet been reported, and the structure of this primary water carrier is uncertain. This study uses synchrotron based single-crystal x-ray diffraction at room temperature to examine the structural changes of lawsonite under compression up to ~10.0 GPa. The great benefit of single-

crystal structure determinations is the ability to *ab initio* determine, and subsequently refine the atomic positions. Moreover, atomic positions can be refined with anisotropic displacement parameters (ADPs), which is not considered a good practice if done with high-pressure powder diffraction data. Here, our goals are to probe and characterize the existence of the proposed ~4.0 GPa transition in lawsonite, and solve the structure of the higher-pressure monoclinic lawsonite. Both the proposed orthorhombic P phase and the monoclinic P phase occur within pressure ranges that are important for our understanding of subduction zones, and both are thus anticipated to be primary carriers of water to depth.

2.2 Methods

2.2.1 Sample characterization

The natural sample used in this study is from the type locality Reed Station, Tiburon Peninsula, Marin Co., California, USA (Ransome 1895). We characterized the sample with single-crystal diffraction and Raman spectroscopy, which both agree well with previous studies (Baur 1978; Daniel et al. 2000; Meyer et al. 2001; Pawley and Allan 2001). Ambient pressure measurements were conducted on Beamline 11.3.1 at the Advanced Light Source (ALS) at Lawrence Berkeley National Lab in Berkeley, CA.

2.2.2 High-pressure single crystal diffraction

High-pressure single-crystal measurements were carried out using either a Merrill-Bassett (HPDO) or BX90 (DESY) type diamond anvil cell (DAC) equipped with type Ia 500 μm culet Boehler-Almax (Boehler and De Hantsetters 2004)

geometry diamond anvils with 80^{o} or 85^{o} angular access. Rhenium gaskets with a 250 μm hole were used to contain the samples. Single crystals of lawsonite and ruby were loaded into the sample compartment with a mixture of 4:1 methanol ethanol as the pressure medium. Methanol:ethanol mixtures remain hydrostatic up to ~10.5 GPa (Klotz et al. 2009). The standard ruby fluorescence gauge was used to determine pressure (Mao et al. 1986).

High-pressure single-crystal X-ray diffraction measurements were conducted at Beamline 12.2.2 at the ALS. The DAC was mounted on a Huber sample stage, and shutterless single-crystal diffraction data were collected on a Perkin Elmer amorphous silicon detector using synchrotron radiation monochromated by silicon(111) to a wavelength of 0.49594 Å (25 keV). Distance and wavelength calibrations were done using a NIST single crystal ruby diffraction standard. Phi scans were employed to measure across both diamonds with 0.25° image width.

2.2.3 Data processing

Image masks, to avoid integrating signal from detector regions obscured by the DAC, were created using the program ECLIPSE (Parsons 2010). The data were integrated using the program SAINT v8.34A. A multi-scan correction for absorption was applied using the program SADABS-2014/11. Structures were solved by dual space methods (SHELXS-97/ SHELXT) and refined by full-matrix least-squares on F^2 (SHELXL-2014) (Sheldrick 2008) using the graphical user interface *ShelXle* (Hubschle et al. 2011). Crystallographic parameters for our structure refinements are shown in Table 2.1. All atoms in the room pressure structure were refined

anisotropically except for the hydrogen atoms, and in the high-pressure structures only the metals were refined anisotropically. For the high-pressure structures, we fixed the O-H bond lengths for the hydroxyls at 0.8(2) Å and for the H_2O molecule, we fixed the O-H bond length to 0.9(2) Å and the H-H distance to 1.5(4) Å. We also set the thermal parameters of the H atoms to ride on their respective oxygen atoms. Complete crystallographic information files (CIFs) for each structure can be found in supplementary material, as well as a discussion on the selection of our unit cells.

Pressure (GPa)	0.0001	5.3(1)	8.4(1)	9.3(1)	9.7(1)
Temperature (K)	298(2)	298(2)	298(2)	298(2)	298(2)
space group	*Cmcm*	*Cmcm*	*Cmcm*	*Cmcm*	$P2_1/m$
a (Å)	5.8569(3)	5.780(2)	5.7363(5)	5.7230(5)	5.2189(13)
b (Å)	8.8087(4)	8.688(3)	8.6155(9)	8.6004(8)	12.934(3)
c (Å)	13.1585(6)	13.038(6)	12.8935(11)	12.8853(11)	5.6856(19)
β (°)	90	90	90	90	124.466(16)
Volume (Å^3)	678.87(6)	654.7(4)	637.21(10)	634.22(10)	316.43(16)
Goodness-of-fit	1.056	1.095	1.055	1.029	1.145
R_1 (%)	1.96	5.00	4.95	4.65	4.69
wR_2 (%)	5.49	13.48	13.67	11.50	13.20

Table 2.1. Crystal structure refinement information for orthorhombic and monoclinic lawsonite on compression. Complete CIFs are found in supplementary material.

2.2.4 Unit cells for our high-pressure structures

By convention, the lattice parameters of an orthorhombic unit cell are reported with the shortest dimension as *a*, the intermediate dimension as *b*, and the longest dimension as *c*. The first reported lawsonite structure does not follow this convention,

and was reported with the *a*- and *b*-axes flipped (Baur 1978), which results in a different spacegroup (e.g. *Ccmm*). A survey of the literature reveals that the unit cell is most commonly reported using the conventional setting with a *Cmcm* spacegroup (Libowitzky and Armbruster 1995; Daniel et al. 2000; Meyer et al. 2001; Pawley and Allan 2001; Ballaran and Angel 2003; Kolesov et al. 2008; Liebscher et al. 2010). Thus, we choose to report our room pressure and 9.3 GPa structures following the conventional setting, with the spacegroup *Cmcm*. In particular, this setting allows us to directly compare our results with the previous Rietveld refinements of the high-pressure lawsonite structure of Pawley and Allan (2001). Moreover, by convention, a monoclinic unit cell is selected which reduces the monoclinic β angle. Thus, in order to directly compare our high-pressure structure with that of Pawley and Allan (2001) and the Pb-Ge high-pressure lawsonite (bartelkeite) structure of Origlieri et al. (2012), we transformed our standard monoclinic setting to a non-standard monoclinic setting using the transformation matrix (0 0 -1/0 1 0/1 0 1). The orthorhombic unit cell transforms into the monoclinic unit cell via the transformation matrix (020 / 001 / 110).

2.2.5 Atom naming convention for monoclinic lawsonite

The atom naming convention for monoclinic lawsonite was first proposed by Pawley and Allan (2001). The oxygen and aluminum atom naming convention that they chose is confusing, and makes it difficult to directly compare corresponding atoms between orthorhombic and monoclinic lawsonite. Pawley and Allan (2001) reported that $O2_{ortho}$ splits into $O2_{mono}$ and $O3_{mono}$, and that $Al1_{ortho}$ splits into $Al1_{mono}$

and $Al2_{mono}$. What is most confusing about this convention is that the oxygen atom numbers 3 thru 5 in orthorhombic lawsonite are numbers 4 thru 6 in monoclinic lawsonite. When discussing the O5 water atom in orthorhombic lawsonite one must state that it is the O6 water atom in monoclinic lawsonite. We chose to adopt a naming convention similar to the low temperature structures of lawsonite reported by Libowitzky and Armbruster (1995). In our structure $O2_{ortho}$ splits into $O2A_{mono}$ and $O2B_{mono}$, and $Al1_{ortho}$ splits into $Al1A_{mono}$ and $Al1B_{mono}$. This convention is less confusing, and importantly the oxygen atoms O3-O5 are the same atoms in orthorhombic and monoclinc lawsonite. This makes the discussion of the O5 water and O4 hydroxyl atoms in orhtorhonbic and monoclinic lawsonite less confusing.

2.3 Results

2.3.1 Unit cell under compression

We collected diffraction patterns at various pressures up to ~10 GPa. The reflections can be indexed to an orthorhombic C unit cell up to ~9.3 GPa. Starting at pressures of ~8.4 GPa, we did observe weak reflections that are systematically absent in a C-centered orthorhombic unit cell (e.g. (017)) this is notably in excess of the pressure of onset (4 GPa) of such forbidden reflections reported by Ballaran and Angel (2003). However, all other observed reflections could be indexed to an orthorhombic C unit cell. These weak reflections did not grow in intensity under compression from ~8.4 to 9.3 GPa. All attempts to index the reflections collected between ~8.4 GPa and ~9.3 GPa to an orthorhombic P-centered unit cell failed. The structure of lawsonite was solved at 5.3, 8.4, 9.3, and 9.7 GPa. We index the

reflections collected at 5.3, 8.4, and 9.3 GPa to an orthorhombic C unit cell, and we determined the spacegroup to be *Cmcm*. We index the reflections collected at 9.7 GPa to a monoclinic P unit cell, and determined the spacegroup to be $P2_1/m$ (Table 2.1). The symmetry we determined for the high-pressure phase is in accord with that inferred from analysis of high-pressure polycrystalline data by Pawley and Allan (2001).

2.3.2 Structural changes in monoclinic lawsonite

The quadratic elongation (QE) and angle variance (AV) is a measure of the distortion of a tetrahedron or octahedron from an ideal polyhedron (Robinson et al. 1971). The site volumes, QE, and AV of the Si, Al, and Ca sites are shown in Table 2.2. Very small changes in the QE and AV of the Al and Si sites occur under compression to 9.7 GPa. The Al site splits into two crystallographically unique sites in monoclinic lawsonite. These two Al-sites have slightly different volumes (Al1A is ~0.04 $Å^3$ smaller than Al1B), and their QEs are identical while the AV of Al1A is slightly larger than Al1B (Table 2.2). This is in contrast to the QE and AV of the Ca site which both *increase* dramatically across the orthorhombic to monoclinic transition. This indicates that this site becomes markedly distorted across the transition.

Site		Ambient	5.3(1) GPa	8.4(1) GPa	9.3(1) GPa	9.7(1) GPa
Si	Vol	2.227(3)	2.196(4)	2.132(5)	2.151(4)	2.171(4)
	QE	1.005	1.005	1.005	1.006	1.005
	AV	19	20	21	20	22
Al1	Vol	9.245(4)	9.031(6)	8.834(6)	8.795(7)	8.671(8)
	QE	1.011	1.009	1.009	1.009	1.009
	AV	36	31	31	30	30
Al2*	Vol	-	-	-	-	8.871(5)

	QE	-	-	-	-	1.009
	AV	-	-	-	-	28
Ca	Vol	18.391(6)	17.396(10)	16.803(10)	16.703(12)	16.639(13)
	QE	1.023	1.023	1.021	1.022	1.032
	AV	78	79	76	75	109

Table 2.2. Polyhedral volumes, quadratic elongation (QE), and angle variance (AV) of the Si, Al, and Ca sites in lawsonite structures at various pressures. *Orthorhombic lawsonite only has one Al site.

$$QE = Quadratic\ Elongation = \sum_{i=1}^{n} (l_i/l_o)^2 /n$$

$$AV = Angle\ Variance = \sum_{i=1}^{n} (\Theta_i/\Theta_o)^2 (n-1)$$

As noted above, the H_2O molecule and hydroxyls in room pressure and temperature lawsonite are dynamically disordered (Libowitzky and Armbruster 1995; Libowitzky 2009), and their reported positions from single crystal diffraction measurements are averaged in time and space. In orthorhombic *Cmcm* lawsonite, the hydroxyl is located on the hydroxylated O4 oxygen, and it is H-bonded to two symmetrically equivalent O2 oxygen atoms. The H_2O molecule is designated as being the O5-water molecule oxygen and is H-bonded to two hydroxylated O4 atoms. This basic configuration is preserved under compression to 9.3 GPa. In monoclinic $P2_1/m$ lawsonite, the O2 atom splits into O2A and O2B atoms in the new structure, and Al1 splits into Al1A and Al1B. In monoclinic lawsonite the hydroxyls reorient towards the closest acceptor, which is O2B. Interestingly, the geometry of the large channel that contains the Ca atoms (as well as the water molecules) remains almost undisturbed across this transition, and the cross section of the channel does not become more circular. In the high-pressure phase, the hydrogen-bonding environment

of the H_20 molecule changes, which results in a slight reorientation of the H_2O molecule parallel to the ±*c* direction.

The main features of the monoclinic high-pressure phase of lawsonite that differ from the low pressure phase (Fig. 2.2) are: (1) the Ca site becomes markedly more distorted in monoclinic lawsonite; (2) the single Al-site splits into two Al-sites with distinct volumes and distortions; (3) the Si-O-Si angle, previously linear and parallel to the *bc* plane, deviates from the symmetry required 180^o; and (4) the hydroxyls become more disordered due to changes in the H-bonding environment. These structural observations are consistent with the Rietveld refined structure reported by Pawley and Allan (2001). The major improvement of our study compared to that of Pawley and Allan (2001) is that our high-pressure single-crystal data allow us to unambiguously resolve the atomic mechanism of the orthorhombic to monoclinic phase transition and to resolve the changes in the orientation of the H-atoms of the H_2O and hydroxyls on the transition.

2.4 Discussion

2.4.1 Aluminosilicate framework and Ca atom: Bond valence analysis

AlO_6 octahedra and SiO_4 tetrahedra are the most fundamental building blocks of the lawsonite aluminosilicate framework. AlO_6 octahedra form linear edge-linked chains that run parallel to the *a*-axis (in the *Cmcm* setting). O3 and O4 constitute the linking octahedral edge. The corner linked Si_2O_7 groups connect these chains to a 3-dimensional framework. O1 is the bridging oxygen connecting the two SiO_4 tetrahedra, O2 atoms form a tetrahedral edge linking two octahedral apices within a

chain, while O3 is the 4th tetrahedral corner that connects to the neighboring octahedral chain roughly parallel to the *b*-axis (*Cmcm* setting). This three dimensional framework has its most flexible pivot point at the rather unconstrained O1 tetrahedral linkage. Large channels contain both the Ca cation as well as the H_2O molecule. The Ca site in orthorhombic lawsonite is a distorted octahedron. It has been proposed by Pawley and Allan (2001) that the Ca site is actually an 8-fold site based on a somewhat arbitrary coordination sphere argument, which assumes that any atom that lies within the defined coordination sphere (3 Å) is considered to be bonded. Moreover, Pawley and Allan (2001) argue that the average bond length of the Ca site increases across the transition which has been interpreted to indicate a change in coordination (Hazen and Finger 1983). Based on relative differences between the Ca-O bonds and their evolution with pressure (Figure 2.2), we regard the Ca coordination to be 6-fold throughout the pressure range investigated, including through the orthorhombic to monoclinic phase transition.

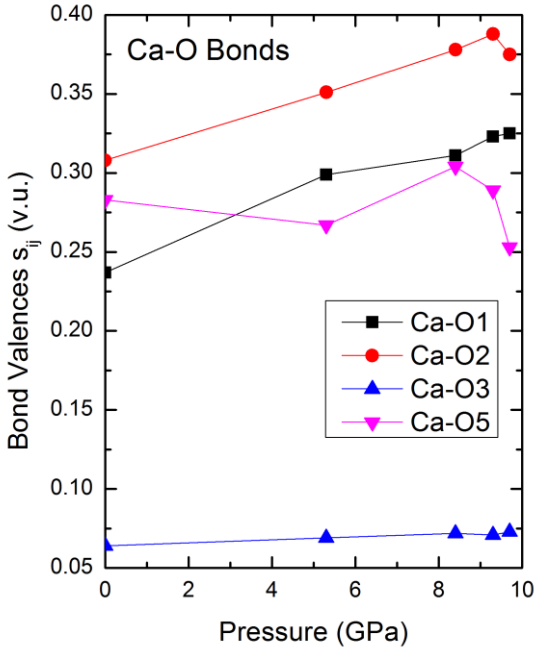

Figure 2.2. Bond valences and their evolution with pressure for the Ca-O bonds. Note the clustering of the O1, O2 and O5 bonds around 0.25 v.u. while O3 is separated from this group with values below 0.08 v.u. There is also a lack of any significant change of the Ca-O3 bond with increasing pressure. This strongly suggests that the Ca in lawsonite remains 6 coordinated up and across its phase transition between 9.3 and 9.7 GPa.

In the following we seek to further understand and quantitatively analyze the lawsonite structure on the basis of the bond valence model (Brown 2002). In this model, bond valences describe the strength of a bond and are uniquely related to bond lengths through the relationship

$$S_{ij} = \exp(R_0 - R_{ij}/b) \qquad (1)$$

with S_{ij} representing the bond valence between atoms i and j, R_{ij} the respective bond length and R_0 and b empirically determined atom-pair specific constants. For a given bond topology (i.e. the connectivity of the cations and anions in the compound), each bond has a unique bond valence (and thus bond length) defined by the two network

equations:

$V_i = \sum_j S_{ij}$ (2) Valence sum rule

$0 = \sum_{loop} S_{ij}$ (3) Equal valence rule

Equation 2 states that the sum of all bond valences converging on any cation or anion is equal to the absolute value of the atom's valence. Equation 3 requires the sum of all bond valences along any given topologic loop in the structure to be zero, assuming bond valences to be positive when looping from cation to anion, and negative when moving within the loop from anion to cation. This equation formalizes the requirement that bond valences should be distributed with the highest possible symmetry around any atom (Pauling's principle of parsimony Pauling, 1929). The network equations predict bond valences and thus bond lengths based on the bond topology. Mapping a given bond topology into 3-dimensional space leads in a general case to conflicting requirements due to mismatched dimensions of unstrained structural units. Therefore, comparing the bond valences predicted by the network equations with actually observed bond valences helps to understand where a given structure is strained due to steric mismatches and what limits its stability and thus drives observed phase transitions.

More details on solving the network equations in lawsonite are given in supplementary information. We compare predicted bond valences with values observed at ambient conditions for all framework cations (Table 2.3). We do not include hydrogen atoms in this comparison because on the one hand their intrinsic asymmetry is not reproduced in the model and on the other hand, observed O-H···O

geometries determined with X-rays are not particularly accurate. However, they can be accounted for by introducing weights into the network equations (Kunz and Brown 1995).

		Network	**0 GPa**	**5.3 GPa**	**8.4 GPa**	**9.3 GPa**	**9.7 GPa***
Ca	O1	0.226	0.237	0.299	0.311	0.323	0.325
	O2	0.394	0.308	0.351	0.378	0.388	0.363
	O2	0.394	0.308	0.351	0.378	0.388	0.363
	O2	0.394	0.308	0.351	0.378	0.388	0.387
	O2	0.394	0.308	0.351	0.378	0.388	0.387
	O5	0.200	0.283	0.267	0.304	0.289	0.253
Sum		**2.00**	**1.88**	**2.108**	**2.271**	**2.306**	**2.221**
Al	O2	0.551	0.488	0.504	0.528	0.537	0.521
	O2	0.551	0.488	0.504	0.528	0.537	0.521
	O3	0.499	0.429	0.46	0.481	0.493	0.507
	O3	0.499	0.429	0.46	0.481	0.493	0.507
	O4	0.450	0.553	0.564	0.583	0.575	0.589
	O4	0.450	0.553	0.564	0.583	0.575	0.589
Sum		**3.00**	**2.94**	**3.056**	**3.184**	**3.21**	**3.232**
Si	O1	0.887	0.96	0.981	1.009	1.02	1.017
	O2	1.056	1.06	1.079	1.125	1.104	1.137
	O2	1.056	1.06	1.079	1.125	1.104	1.124
	O3	1.003	0.981	1.021	1.062	1.036	1.021
Sum		**4.00**	**4.061**	**4.16**	**4.321**	**4.264**	**4.299**
O1	Ca	0.226	0.237	0.299	0.311	0.323	0.325
	Si	0.887	0.96	0.981	1.009	1.036	1.017
	Si	0.887	0.96	0.981	1.009	1.036	1.017
Sum		**2.00**	**2.157**	**2.261**	**2.329**	**2.395**	**2.359**
O2	Ca	0.394	0.308	0.351	0.378	0.323	0.375
	Al	0.551	0.488	0.504	0.528	0.493	0.521
	Si	1.056	1.06	1.079	1.125	1.036	1.131
Sum		**2.00**	**1.856**	**1.934**	**2.329**	**1.961**	**2.027**
O3	Al	0.499	0.429	0.46	0.481	0.493	0.491
	Al	0.499	0.429	0.46	0.481	0.493	0.522
	Si	1.003	0.981	1.021	1.062	1.036	1.021
Sum		**2.00**	**1.839**	**1.941**	**2.024**	**2.022**	**2.034**
O4	Al	0.450	0.553	0.564	0.583	0.575	0.587

	Al	0.450	0.553	0.564	0.583	0.575	0.591
	H2	0.10	0.041	0.05	0.051	0.053	0.057
	H1	0.92	1.024	0.979	0.051	0.968	0.934
	H1	0.08	0.025	0.049	0.953	0.058	0.026
Sum		**2.00**	**2.196**	**2.206**	**2.221**	**2.229**	**2.195**
O5	Ca	0.20	0.283	0.267	0.304	0.388	0.253
	H2	0.90	0.834	0.762	0.721	0.746	0.729
	H2	0.90	0.834	0.762	0.721	0.746	0.729
Sum		**2.00**	**1.951**	**1.791**	**1.746**	**1.782**	**1.711**

Table 2.3. Predicted (network) and observed bond valences for Lawsonite framework (cations and oxygens, excluding hydrogens). *For the monoclinic 9.7 GPa structure, the symmetry split Al and O2 values are averaged to facilitate comparison with the orthorhombic structures.

The relative strengths of the individual Ca-O bonds are more or less identical in the observed and predicted CaO_6 environment, with the Ca-O2 bonds being observed and predicted to be the strongest bond. However, the observed Ca-O2 bonds are still clearly weaker than the predicted (0.308 versus. 0.394 v.u.) values (Table 2.3). This indicates that the large channel where Ca is situated is too large for the size of Ca. For Ca to be sufficiently coordinated in the lawsonite structure it needs an additional Ca-O bond, which is provided by the H_2O molecule that is also packed into the channel, but otherwise does not participate in the framework. The equilibrium position for Ca seems to be slightly above the center of a rectangle formed by four O2 atoms belonging to two adjacent Si_2O_7 groups. In this position, it can form additional bonds to O1 and the O5 of the water molecule. This position in turn influences the geometry of the tetrahedral-octahedral aluminosilicate framework: here, we first observe a fairly good match between predicted and observed SiO_4 bond strengths.

However, we also notice a significant discrepancy between observed and predicted geometries of the AlO_6 octahedron. The network equations predict the O3 and O4 axes (which link the octahedra into an edge-shared chain) to be of similar medium length (Al-O3/O4 1.90 and 1.94 Å, respectively) with a short (Al-O2 ~1.87 Å) O2-O2 axis perpendicular to it. We observe however a medium long (Al-O2 ~ 1.92 Å) O2-O2 axis perpendicular to a distorted O3-O4-O3-O4 plane with a long (Al-O3 ~ 1.96 Å) O3-O3 axis and a short (Al-O4 ~ 1.87 Å) O4-O4 axis. This can be rationalized by the fact that the underbonded Ca needs to draw 2/3 of its valence requirements from the four O2 atoms to which it is bonded. Ca-O2 is therefore also predicted to be the strongest bond in the Ca environment. The realization of the network predicted Ca-O2 bond within the limits of the lawsonite structure is, however, in conflict with the size of the O2-O2-O2-O2 rectangle defined by the aluminosilicate framework. The three dimensional geometry and symmetry cause conflicting constraints on the Ca-O2 and Al-O2 bonds: For Ca-O2 to become as short as predicted by the network, the O2-Al-O2 axis would need to be stretched beyond the network predicted Al-O2 length. This leads to an elongation of the O2-Al-O2 axis, relative to the network prediction. The Al cation compensates some of the associated loss of bond valence by shortening the Al-O3 and Al-O4 bonds. It does this in an asymmetric way since O3 is also coordinated to Si, whereas O4 is only bonded to its neighbor Al and the hydroxyl hydrogen. This strained nature of the lawsonite structure at ambient conditions is also reflected in the observed bond valence sums (Figure 2.3, and Table 2.3). While Al and Si show bond valence sums that match closely the expected values (3 and 4,

respectively), we find Ca, O2 and O3 to be underbonded (differences ~ -12%, -7%, -8%, respectively), while O1 is strongly overbonded (~ +8%). O4 and O5 are also over and underbonded, but we do not weigh those values strongly in our interpretation due to the limited accuracy of the position of the H atom determined with X-rays. It is known that the insufficiently accounted-for libration of the hydrogen around the associated O atom can lead to an apparent shortening of the O-H bond (e.g. Kunz et al., 2006).

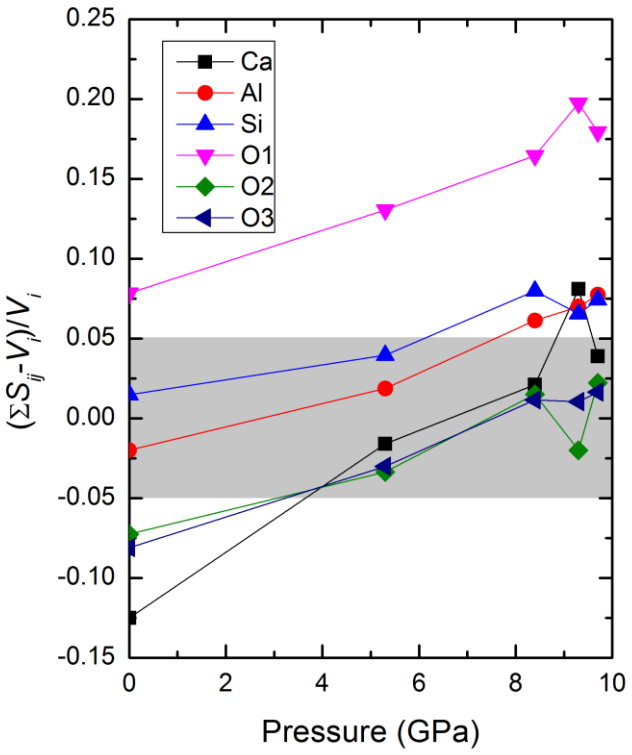

Figure 2.3. Relative deviation of observed bond valence sums (S_{ij}) from their ideal values (i.e. absolute values of atomic valence (V_i)). The grey shaded area is regarded as a "comfort zone" for the internal strain in an extended crystal structure.

2.4.2 Details of bond valence calculations and solution of network equations

Observed bond valence sums were calculated using the observed bond lengths

and the following atom pair specific parameters (Table 2.4) for equation (1) in main text.

Atom pair	R_o	b
Ca-O	1.967	0.37
Al-O	1.651	0.37
Si-O	1.640	0.37
H-O	0.79	0.37

Table 2.4. Atom specific pair parameters used for the bond valence calculations.

The solution of the network equations (eqs (2) and (3) in main text) is based on a given topology (i.e. atomic connectivity table). We established a bond graph based on a 6-fold coordinated Ca. The calculations were performed with an in-house written code written in Matlab. It follows the robust iterative approach originally described in Brown (1977). This method initially assigns to each bond starting bond valences which correspond to the average V_i/N for the two atoms terminating each bond, where V_i is the atomic valence and N is the coordination number. Since these initial average values do not obey equation (2) (valence sum rule) they are iteratively adjusted for all cations and anions until the valence sum rule is fulfilled at all atoms. The iterative adjustments ensure that equation (3) stays fulfilled. The number of iterative cycles corresponds roughly to the number of bond valences to be determined.

Network equations intrinsically fail to predict the known asymmetry of the O-H…O configuration. Although we do not attempt to compare network predicted O-H…O configurations with our experimental ones, we still need to reproduce this asymmetry since mostly the strong O-H bonds have a ripple effect on the rest of the

structure. As discussed by Kunz and Brown (1992), this can be accounted for by introducing weights into the network equations. We found that weights of 2.0 and 0.2 for O-H and O…H respectively, reproduce the observed configuration in a satisfactory way.

2.4.3 H_2O molecule

In orthorhombic *Cmcm* lawsonite, the H_2O molecule is H-bonded to the O4 oxygens (Figure 2.4a) and the H atoms are dynamically disordered between two equivalent sites (Libowitzky and Armbruster 1995; Libowitzky 2009). Our single-crystal data show that the donor-acceptor distances in orthorhombic lawsonite between O5 and O4 decrease symmetrically by ~0.7 Å by 9.3 GPa, and that these oxygens lie in the same plane with the two H atoms associated with the water. This is in contrast to the changes observed at low temperature, where the distance between O5 and the two O4 atoms decrease by different amounts and the position of the H_2O molecule is refined as being oriented towards the closest acceptor: O4 (Libowitzky and Armbruster 1995). The decrease in distance of this hydrogen-bonded unit associated with the water molecule that is observed under compression is significant, and the H-bonds of the H_2O molecule are strengthened, which stabilizes its configuration. Since the two H-bond distances decrease by the same amount, the H_2O molecule is not expected to rotate or "freeze" into an ordered position. The cross channel distances between O4-O4 and O2-O2 change by essentially the same amount (~0.13 Å) from ambient to 9.3 GPa, whereas the O3-O3 distance only changes by ~0.03 Å. As the channel dimensions relative to the O5 water atom change

symmetrically, there is no evidence that suggests that the H_2O molecule orders under compression. Moreover, it likely remains dynamically disordered under compression to at least 9.3 GPa, and our refined position at 9.3 GPa is the average position of the H_2O molecule.

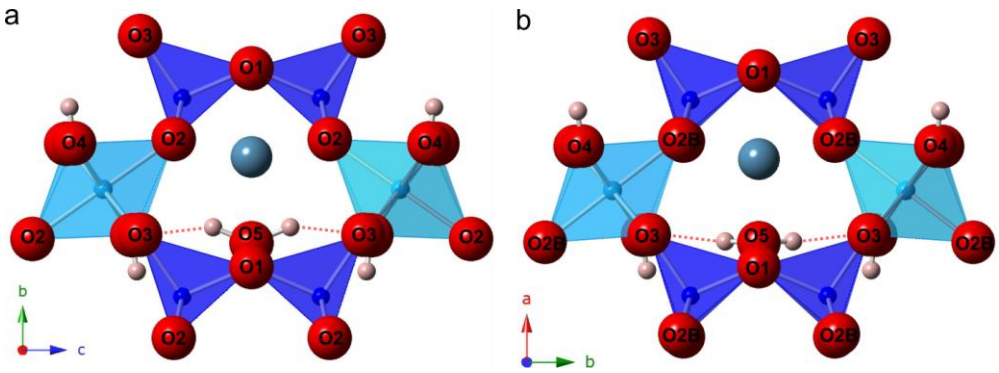

Figure 2.4. H_2O H-bonding environment of (a) orthorhombic lawsonite at 9.3 GPa, and (b) monoclinic lawsonite at 9.7 GPa. The H_2O molecule in monoclinic lawsonite rotates into the page, and rotation in the *ab* plane is not observed. Dotted lines represent H-bonds of the H_2O molecule. Atom colors are the same as Figure 2.1.

Across the orthorhombic to monoclinic phase transition, the two oxygen atoms to which the H_2O molecule is H-bonded move out of the plane. This motion causes the H_2O molecule to rotate slightly in order to remain H-bonded to these closest acceptors (Figure 2.4b). For reference, the H_2O molecule in the isostructural mineral bartelkeite ($PbFeGe^{VI}(Ge_2{}^{IV}O_7)(OH)_2 \cdot H_2O$) shows the same change in orientation (Origlieri et al., 2012). Importantly, the distances between O5 and the two O4 atoms change by the same amount, demonstrating that neither acceptor becomes closer across the transition, and hence the H_2O molecule remains symmetrically oriented, and disordered. The H-bonding environment of the H_2O molecule does become more complex in monoclinic lawsonite (Figure 2.4a). This is due to O2

splitting into the separate sites O2A and O2B, which creates two different, longer donor-acceptor lengths from the O5 water atom to O2A and O2B in monoclinic lawsonite. At 9.7 GPa, these two oxygen atoms are still far enough away (>3.0 Å), that they are expected to only form weak (if any) hydrogen bonds.

Thus, our single-crystal data do not provide any evidence that the H_2O molecule becomes ordered in monoclinic lawsonite. Our refined H_2O position in monoclinic lawsonite is therefore likely an average position of the H_2O molecule. This modest shift in orientation, but not ordering, is consistent with previous Raman and infrared spectroscopic investigations which indicate that the H-bonding environment of the H_2O molecule does not change significantly under compression or across the orthorhombic to monoclinic phase transition (Scott and Williams 1999; Daniel et al. 2000). Moreover, ordering of the H_2O molecule in lawsonite across its low-temperature phase transitions produces a discrete H-bonding environment for the H_2O molecule, which is spectroscopically manifested by a decrease in the full width at half max (FWHM) of the O-H vibrational modes (Kolesov et al. 2008; Libowitzky 2009). Decreases in the FWHM of the O-H vibrational modes under compression is not observed, suggesting that the H_2O molecule does not order under compression to at least 20 GPa (Scott and Williams 1999; Daniel et al. 2000; Scott et al. 2007).

2.4.4 Hydroxyls

The hydroxyls in room temperature orthorhombic *Cmcm* lawsonite are also disordered (Libowitzky and Armbruster 1995; Libowitzky 2009). In orthorhombic *Cmcm* lawsonite, the hydroxyls are located on the O4 oxygen and the hydroxyl is H-

bonded to two symmetrically equivalent O2 atoms (Figure 2.5a). At 9.3 GPa, the O4 to O2 distance is 2.853(3) Å, and the hydrogen-bond angle between O4-H···O2 is ~132^{o}. Interestingly, the cross channel distance (O4 to O4) and the O4 to O5 distances are both shorter (2.575 and 2.671 Å, respectively) than the O4 to O2 distance. The hydrogen bond might be expected to be oriented towards the closest acceptor, which in lawsonite at room pressure and temperature is the O5 atom. However, H-H repulsion between the hydroxyls likely prevents them from being oriented/hydrogen-bound out into the channel at the same time, or flipping towards the O5 oxygen (assuming that the orientation of the H_2O molecule does not change). At 9.3 GPa, the configuration of the hydroxyls changes slightly from ambient pressures, and our refined positions place the hydroxyl H-atoms out into the channel. Since this is an average position for the hydroxyl H-atoms, this shift indicates that the H-bonding across the channel has increased under compression to 9.3 GPa. This change is consistent with the hydroxyls becoming more delocalized, and hence more disordered: the shift of hydroxyls into the channel is not surprising since the cross-channel distance decreases by ~0.13 Å to 9.3 GPa, and this behavior may be precursory to the high-pressure phase transition. The refined H-H distance at 9.3 GPa is too close (at ~1.09 Å), and there may be cooperative motion between the hydroxyl units, with both being unlikely to be H-bonded out in the channel simultaneously due to H-H repulsion.

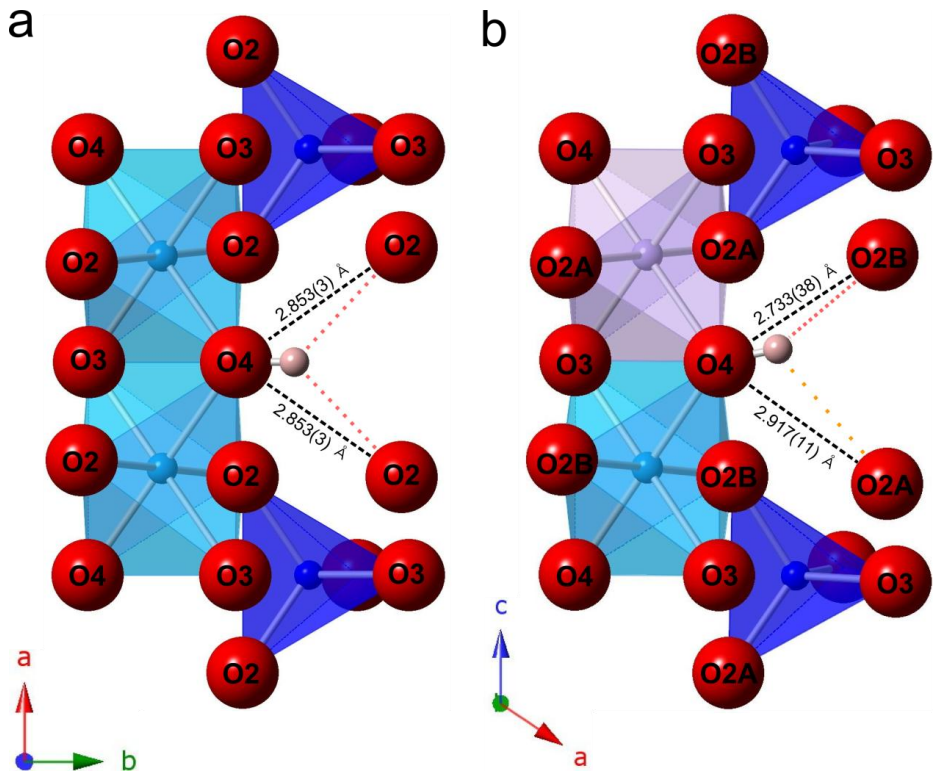

Figure 2.5. Hydroxyl H-bonding environment of (a) orthorhombic lawsonite at 9.3 GPa, and (b) monoclinic lawsonite at 9.7 GPa. Note that the hydroxyls in monoclinic lawsonite re-orient towards the closest acceptor (O2B). Dotted lines indicate H-Bonds and dashed lines are distance between hydroxyl oxygen and O2 or O2A or B. Atom colors are the same as Figure 2.1.

In the high-pressure monoclinic phase, $O2_{orth}$ splits into $O2A_{mono}$ and $O2B_{mono}$ (Pawley and Allan 2001; Liebscher et al. 2010) which gives rise to two different donor-acceptor distances from O4 to O2A and O2B (Figure 4b). At 9.7 GPa, the donor-acceptor distance from O4 to O2A and O2B is 2.917(11) Å and 2.733(38) Å respectively. The hydroxyl is observed to reorient towards the O2B atom (Figure 2.5b), and the angle between O5-H···O2B is ~148^{o}, while between O5-H···O2A, it is ~118^{o}. It should be noted that these non-traditional/abnormal hydrogen bond angles are strongly indicative of dynamic disorder (Brown 1976). This re-orientation

minimizes the H-H repulsion between the two H-atoms of the hydroxyls that reside in the same channel. The observed orientation of the hydroxyls in monoclinic lawsonite is similar to that observed in the Pb-Ge lawsonite-like monoclinic phase bartelkeite. In bartelkeite, the hydroxyls are oriented towards the closer acceptor O2B and engaged in one strong H-bond and one weak H-Bond (Origlieri et al. 2012). As in orthorhombic lawsonite, H-H repulsion in monoclinic lawsonite likely prevents the re-orientation of both hydroxyls out into the channel, and H-H repulsion likely increases under compression to ~9.3 GPa.

As with the H_2O molecule, our single-crystal data provide no evidence that hydroxyls become ordered in monoclinic lawsonite. From a vibrational spectroscopic perspective, changes in the H-bonding environment of the hydroxyls are the primary manifestation of the orthorhombic to monoclinic phase transition (e.g. Scott and Williams, 1999; Daniel et al., 2000; Scott et al., 2007). Scott and Williams (1999) report that the pressure shifts of both of the infrared hydroxyl stretching vibrations change near 9.0 GPa, with one of them beginning to shift negatively above ~9.0 GPa. Their interpretation was that changes in O-O distances primarily control the behavior of the hydroxyls in orthorhombic lawsonite, whereas changes in O-H···O angles primarily control the behavior of the hydroxyls in monoclinic lawsonite. For comparison, the Raman active OH stretching modes initially shift positively, but also shift negatively on the transition to the high-pressure phase of lawsonite (Daniel et al. 2000). High-pressure far infrared spectra show that a new band near 368 cm^{-1} appears in the monoclinic phase of lawsonite, which is likely produced by librational motion

of the OH groups and indicates that the OH environment changes in monoclinic lawsonite (Scott et al. 2007). Thus, previous spectroscopic investigations are in full accord with our single-crystal refinement in showing that the H-bonding environment of the hydroxyls becomes more complex in monoclinic lawsonite. Indeed, our single crystal structural refinement of monoclinic lawsonite show that the hydroxyls re-orient in monoclinic lawsonite, and that the disordered hydroxyl positions in monoclinic lawsonite include displacements along the *c*-axis of the crystal structure.

2.4.5 Mechanism of high-pressure phase transition

Previously the phase transition mechanism was described as a shearing of the structure that opens up the monoclinic β angle (Daniel et al. 2000, Pawley and Allan 2001). Daniel et al. (2000) propose that the phase transition is ferroelastic in nature, and that it is driven by shear. Pawley and Allan (2001) state that shearing parallel to the AlO_6 octahedral chains breaks the symmetry of the Al-O2-Si angles, doubles their numbers, and opens up the monoclinic β angle. Our data indicate that the orthorhombic to monoclinic phase transition between 9.3 and 9.7 GPa is neither driven by a change in coordination number of the Ca cation nor by a noticeable shearing of the structural framework.

The pressure evolution of the Ca-O bonds is observed within a group of fairly strong (s_{ij} > 0.2 v.u.) bonds (Ca-O1, Ca-O2, Ca-O5). In this group, the Ca-O bonds linked to the aluminosilicate framework show a general strengthening trend while O5, linked only to Ca and the H_2O molecule stays more or less constant in strength. Across the phase transition, the Ca-O1 bonds strengthen only slightly, while the 4 Ca-

O2 bonds weaken. These 6 Ca-O bonds are clearly differ in strength from the Ca-O3 bond which is not only much weaker (s_{ij} < 0.1) than Ca-O1, Ca-O2 and Ca-O5 but also does not change significantly with increasing pressure up to and across the phase transition. Therefore, there is no physical rationale to propose anything other than 6-fold coordination for Ca at all pressures probed, and across the phase transition. The general topology of the lawsonite structure remains unchanged across the phase transition. Indeed, when comparing the orthorhombic and monoclinic structures, it is visually difficult to discern any difference (Figure 2.6). At 9.3 GPa, the angle of what will become the monoclinic β-angle in the orthorhombic structure is 123.66°: this changes to only 124.47° across the phase transition. The largest atomic shifts from 9.3 to 9.7 GPa are observed for O1 and O5 (Table 2.5). Their shift vectors are almost parallel (angle ~ 1.6°) and lie in the monoclinic *a*-*c* plane.

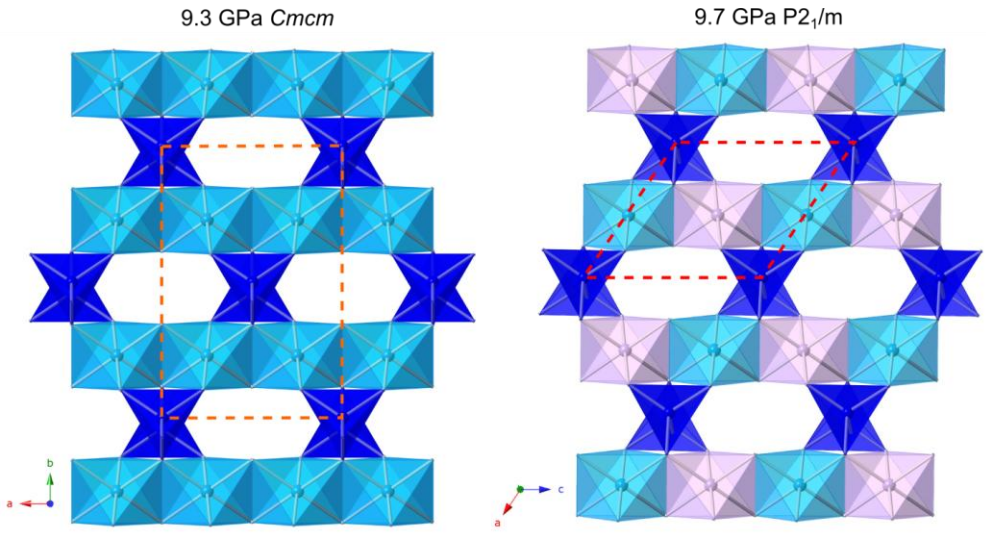

Figure 2.6. Structural diagrams of the aluminosilicate framework of orthorhombic and monoclinc lawsonite. Unit cells are shown as dotted lines. These structures are almost indistinguishable from one another.

	9.3 GPa Ortho_MonoSetting			9.7 GPa Mono			Shift (Å)
Ca	0.3374	0.75	0.6687	0.3386	0.75	0.6795	0.058
Al1A	0.5	0	0.5	0.5	0	0.5	0
Al1B	0.5	0	0	0.5	0	0	0
Si	-0.0410	0.1335	0.9795	-0.0377	0.1342	0.9866	0.035
O1	0.8920	0.75	0.946	0.8885	0.75	0.9150	0.167
O2A	0.7514	0.1191	0.6452	0.7525	0.1211	0.6488	0.031
O2B	0.7514	0.3808	0.1062	0.7653	0.3851	0.1182	0.080
O3	0.2716	0.0624	0.1358	0.2750	0.0630	0.1358	0.019
O4	0.2674	0.0488	0.6337	0.2733	0.0512	0.6319	0.048
O5	0.7732	0.75	0.3866	0.7661	0.75	0.338	0.25

Table 2.5. Comparison of atomic shifts across the phase transition between 9.3 and 9.7 GPa. The orthorhombic coordinates at 9.3 GPa were transformed into the monoclinic reference system using the transformation matrix $\begin{bmatrix} 0 & 2 & 0 \\ 0 & 0 & 1 \\ 1 & 1 & 0 \end{bmatrix}$. The shift was calculated using the monoclinic 9.7 GPa cell parameters.

We use again bond valences to shed light on the mechanism of the orthorhombic to monoclinic phase transition. As described above the lawsonite structure exhibits a peculiar pattern of internal strains at ambient conditions. This is plotted – together with its pressure evolution - in Figure 2.3 as a relative deviation of the bond valence sum from the ideal value. Disregarding the less-well-determined O-H bonds linked to O4 and O5, we find a tensional strain (underbonding) for Ca, O2 and O3 and high compressional strain (overbonding) for O1. Si and Al are well within the 'comfort zone' of ± 5 % deviation from ideal bonding. The overall tensile strain in the lawsonite structure at ambient pressure is not surprising given that it is a mineral stabilized at high pressure. The peculiar situation of O1 can be understood in terms of its role as the bridging oxygen in the Si_2O_7 group. Being coordinated to two

Si atoms with ideal bond valences of 1.0 v.u. for each bond, saturates the bond valence requirements of O1 (i.e. 2.0). Its additional somewhat forced coordination to Ca leads to the observed overbonding. The application of pressure moves the underbonded atoms into the ideal bonding comfort zone while the overbonding of O1 becomes more pronounced. Finally at 9.3 GPa, O1 is overbonded by 20%, which is often viewed as the limit for structural stability (Brown 2002). At this pressure all cations are slightly overbonded as well. We regard the massive overbonding of O1 as the driving force of the ensuing phase transition between 9.3 and 9.7 GPa, particularly as the phase transition leads to a substantial decrease in the overbonding of O1. Hence, the O1 atom plays the villain in the high-pressure orthorhombic to monoclinic phase transition. This is mainly achieved by a slight lengthening (i.e. weakening) of the two O1-Si bonds at the O1 atom. In order to achieve this, O1 moves off the mirror/glide planes perpendicular to the *a*- and *b*-axes, respectively, which reduces the point group symmetry from 2/m 2/m 2/m to . 2/m ., and hence the orthorhombic to monoclinic phase transition occurs. The shift of O1 away from the orthorhombic c-glide plane is by approximately 0.24 Å roughly parallel to the *b-axis*. This shift of the Si_2O_7 bridging oxygen leads to a slight rotation of the rigid SiO_4 tetrahedra, which in turn leads to a twisting of the octahedral chain, to which they are attached, away from a straight edge-connected chain (Figure 2.7). This twisting leads to a splitting of both, the Al cation and O2 anion through the loss of C centering. Nevertheless, the individual atomic shifts are quite small (Table 2.5). Thus, the net effect of the phase transition is to remove a topologically-induced overbonding via a relatively modest

deformation, and it is this deformation that likely allows the monoclinic lawsonite phase to be stable at pressures above ~9.5 GPa.

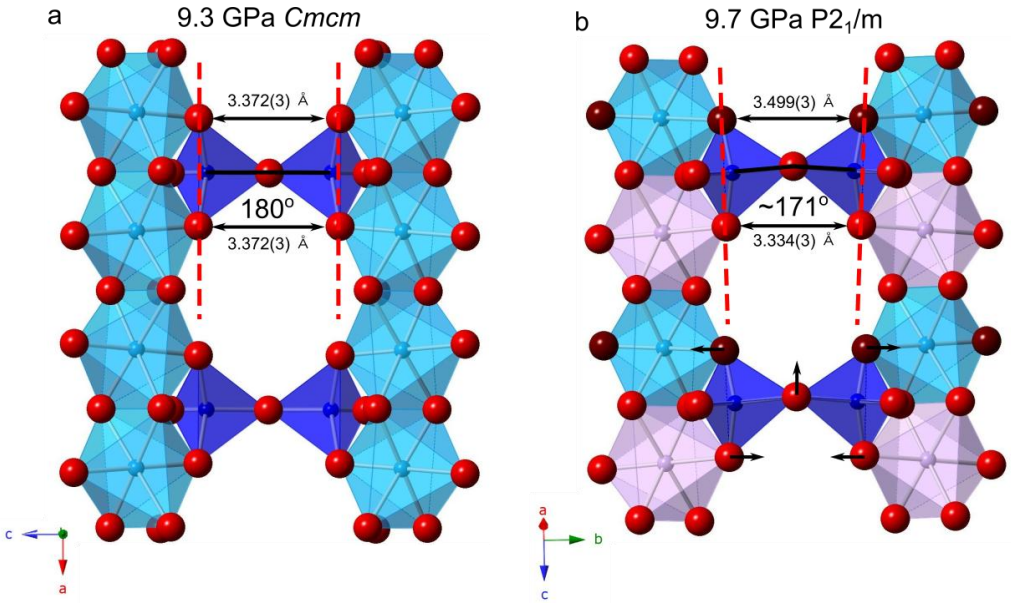

Figure 2.7. Illustration of the O1 shift off the mirror plane perpendicular to the orthorhombic *c*-axis. The plane defined by Si-O1 and O3 at the two SiO_4 tetrahedra tilts at O1 by an angle of ~ 9°. The shift in distances of the individual atoms are given in Table 2.5.

2.5 Geophysical Implications

Notably, lawsonite has been observed to be stable to pressures as high as 14 GPa at temperatures of ~600°C, which represent conditions encountered in cold subduction environments (Pawley 1994). Our results have implications for the anisotropy, crystal structure, and phase transitions of lawsonite as it is subducted to depth within meta-basalts in Earth's mantle. In particular, lawsonite compresses nearly isotropically up to the ~9.3 GPa phase transition, confirming previous inferences from polycrystalline diffraction (Im and Lee, 2016): thus, the level of

compressional wave anisotropy in lawsonite is likely to remain relatively constant under compression (Ballaran and Angel 2003; Fujimoto et al. 2010; Chantel et al. 2012). We do not observe a previously reported transition from orthorhombic C to orthorhombic P symmetry near 4.0 GPa, nor at pressures higher than 4.0 GPa, and lawsonite undergoes only one phase transition, from orthorhombic to monoclinic symmetry near 9.5 GPa, under compression to ~10.0 GPa.

Across the transition, the Ca site becomes markedly distorted, O2 splits into two separate oxygen sites, O2A and O2B, and Al1 splits into two octahedral sites, Al1A and Al1B, and the disordered hydroxyls become more delocalized, and their distribution shifts along the *c*-axis. The shifts in distortion, numbers of sites, and increased delocalization documented here each imply that monoclinic lawsonite is a higher entropy phase than orthorhombic lawsonite (e.g. $\Delta S_{\text{ortho-mono}}$ is positive), which is consistent with a previous inference of Liebscher et al. (2010) based on the Sr-analogue of lawsonite. Pawley and Allan (2001) proposed a positive Clapeyron slope for this transition (and hence lower entropy for the high pressure phase), but ultimately concluded that "a negative slope cannot be ruled out." Our structural solutions of the high-pressure phase show that the volume change $\Delta V_{\text{ortho-mono}}$ is small and negative, consistent with previous studies of Daniel et al. (2000), Pawley and Allan (2001), and Ballaran and Angel (2003).

Hence, monoclinic lawsonite is expected to occur at lower pressures than its ~9.5 GPa pressure of occurrence at 300 K, within warmer subduction zone environments. Given the expectation that the *Cmcm*-$P2_1/m$ transition has a negative

slope, the high-pressure monoclinic phase of lawsonite is expected to exist in meta-basalt assemblages in cold subduction environments approaching and exceeding 300 km in depth, barring any undocumented high-temperature polymorphism. Notably, the stability field of lawsonite in the CASH system was determined from the analysis of high-pressure run products (e.g., Schmidt and Poli, 1994), and the phase of lawsonite *in situ* in these experiments is not known. Even if the Clapeyron slope of the transition is close to flat, there is still a large pressure and temperature range where monoclinic lawsonite would be stable within cold subduction environments (Figure 2.8). Hence, we expect that this modestly distorted form of lawsonite is a major carrier of water to depths approaching the transition zone, and is of key importance in transporting water into the deep upper mantle.

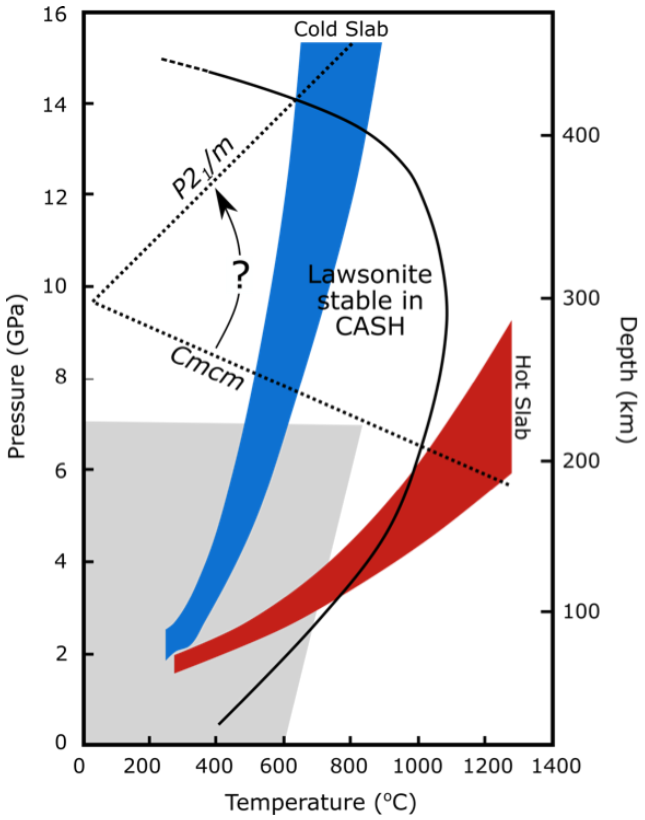

Figure 2.8. Possible slopes for the *Cmcm* to $P2_1/m$ phase transition. Grey region represents the stability field of Cmcm lawsonite determined in situ (Comodi and Zanazzi 1996; Pawley et al. 1996; Chinnery et al. 2000; Grevel and Nowlan 2000; Pawley and Allan 2001). Hypothetical slab pressure-temperature paths from (Ono 1998). Lawsonite stability in CASH system, solid black line (Newton and Kennedy 1963; Pawley 1994; Schmidt and Poli 1994).

The distorted Ca site and multiple Al-sites of monoclinic laswonite also have implications for the geochemical partitioning behavior of elements at depth and during dehydration. Halogen partitioning in subducting slabs is complex, and lawsonite does incorporate trace amounts of F, Cl, Br, and I (Pagé et al. 2016). Indeed, upon apatite decomposition at ~200 km, F has been proposed to be sequestered in lawsonite and phengite (Pagé et al. 2016). Thus, lawsonite and phengite represent two of the few minerals that may transport F to depths greater than 200 km and the increased H-H repulsion in the monoclinic phase of lawsonite may enhance the solubility of F in lawsonite. Speculatively, monoclinic lawsonite may, within cold subduction zones, be a significant means of transport of F to depth, which could contribute to the high F content observed in deep mantle, subduction-associated magmas (Paul et al. 1976; Kendrick et al. 2015). Ultimately, if the transition zone functions as an F repository (e.g., Roberge et al., 2015), monoclinic lawsonite could be a primary mechanism through which F is transported to depths close to this region of the planet.

The monoclinic phase is anticipated to impact lawsonite stability and the manner in which lawsonite dehydrates in subduction zones. Our single crystal structure shows that the H-bonding environment of the H_2O molecule changes across

the transition in a manner that stabilizes the average position of the molecule across the transition. With respect to the hydroxyls, they re-orient slightly towards the closer acceptor (O2B), which changes their average position along the *c*-axis. This, combined with the rotation of the H_2O molecule in the ± *c*-direction, suggests that the electrical conductivity via proton mobility of the monoclinic phase may be enhanced along the *c*-direction. Our single crystal data provides the first evidence of reorientations of the H_2O molecules and hydroxyls across the orthorhombic to monoclinic lawsonite phase transition. These re-orientations could also be relevant to the detailed dehydration mechanism of lawsonite, which is currently poorly understood. The actual mechanism of lawsonite dehydration is important, since it has been suggested that lawsonite dehydration could directly trigger earthquakes in subducting oceanic crust (Okazaki and Hirth 2016; Incel et al. 2017). The relative bonding environments of the water molecules and hydroxyl units indicate that the dehydration of monoclinic lawsonite could be a multi-stage process that commences with the hydroxyls, as they are both significantly more disordered in monoclinic lawsonite, and in relatively close proximity to one another. Hence, relative to the stabilized position of the water molecule in the monoclinic phase, the hydroxyl units may be more prone to being destabilized within monoclinic lawsonite.

Chapter 3

Delocalization in Cr^{3+} luminescence of clinochlore: A pressure-induced transition from single-ion emission to pair emission

3.1 Introduction

The luminescence spectra of layered quasi-two-dimensional compounds have attracted considerable attention (Patterson et al. 1984; Nagasundaram et al. 1986; Lacasce et al. 1987; Assefa et al. 1991, 1994; Yersin and Riedl 1995; Tanner et al. 2005; Czaja et al. 2014). Here, we focus on transition metal chromophores (and particularly Cr^{3+}) in a layered silicate structure under compression, and at low temperatures. Previously, a number of luminescence studies of quasi-two-dimensional compounds have focused on layered gold cyanide salts such as $M[Au(CN)_2]$ (where M = K, Cs, Ti, Eu, or Tb), in which excitation of $[Au(CN)_2]_n^{n-1}$ clusters produces a temperature-dependent emission (Hettiarachchi et al. 2002). Moreover, excitation into the absorption band of $[Au(CN)_2]_n^{n-1}$ clusters can lead to energy transfer and emission of Eu^{3+} and Tb^{3+} (Assefa et al. 1994; Rawashdeh-Omary et al. 2000). In contrast, the properties of Cr^{3+} and Mn^{2+} luminescence in layered structures are limited to only a few studies (Czaja 2002; Czaja et al. 2014) under ambient pressure conditions, and at low temperatures. Luminescence at high-pressure in layered structures has been examined in gold cyanide compounds (Yersin and Riedl 1995; Strasser et al. 1998). The pressure-induced energy shifts of the emission in these compounds are some of the largest known for solid compounds (up to -1600 cm^{-1}/GPa). Moreover, the in-plane magnetic coupling between ions has been probed under pressure in layered copper-organic hybrid compounds (Drillon et al. 2002). Here, we examine the

pressure- and temperature dependence of the luminescence spectrum of Cr^{3+} within the layered silicate $(Mg,Fe^{2+})_5Al(Si_3Al)O_{10}(OH)_8$-clinochlore to probe the magnitude of pressure shifts of emission in this compound, and to characterize whether significant shifts in magnetic exchange coupling between ions occurs on compression.

The high-pressure behavior of Cr^{3+} luminescence is well characterized for ruby, which is widely used as a pressure calibrant (Mao et al. 1986). However, only a subset of oxides have had the luminescence of Cr^{3+} dopants examined under pressure: these include alexandrite, emerald, MgO, $MgAl_2O_4$, $LiAlSi_2O_6$, and a range of garnets (Chopelas and Nicol 1982; Kottke and Williams 1983; Jahren et al. 1992; Wamsley and Bray 1994; Jovanić 2000; O'Bannon and Williams 2016a, 2016b). To our knowledge, the high-pressure behavior of Cr^{3+} luminescence in a layered silicate structure has not previously been explored. $(Mg,Fe^{2+})_5Al(Si_3Al)O_{10}(OH)_8$-clinochlore is a well-characterized layer silicate (Figure 3.1) that has a relatively simple in-layer geometry of octahedral sites, and is known to have sharp-line fluorescence of Cr^{3+} associated with its strong crystal-field environment (Czaja et al. 2014). Previously, the high-pressure structural response of a Cr-bearing clinochlore has been studied using powder diffraction, and a polytypic transformation was reported at ~6.0 GPa (Welch and Crichton 2005). Thus, clinochlore allows us to probe the luminescent response of Cr^{3+} (both as Cr-Cr pairs and single Cr atoms) under pressure within a quasi-two-dimensional structure for which the low-pressure structural response has

been characterized, as well as through a polytypic transition (a rearrangement of the layers relative to one another) at moderate pressures.

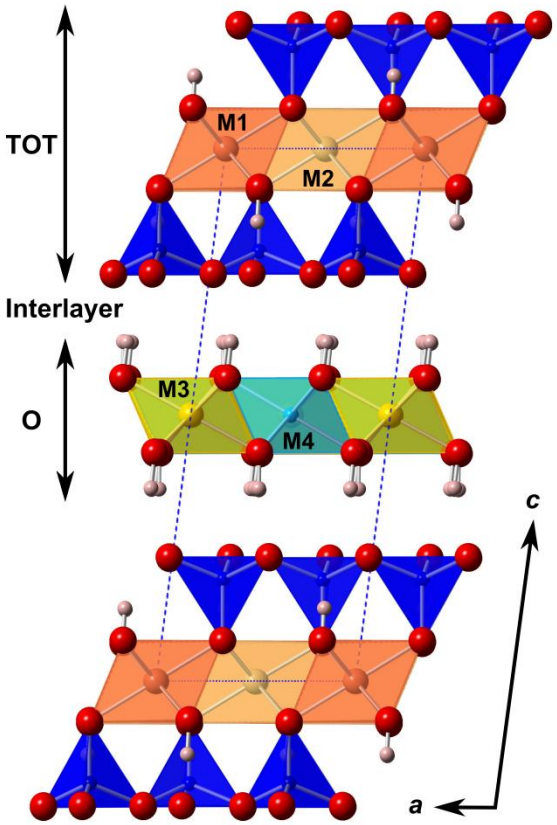

Figure 3.1. Crystal structure of clinochlore at ambient conditions looking down the *b*-axis. M1, M2, M3 = Mg M4 = Al, tetrahedral sites (blue) are Si. Cr^{3+} is most likely to substitute into the M1 and M2 sites. Dashed line indicates unit cell, crystal structure after (Zanazzi et al. 2007). Diagram made in CrystalMaker® v8.7.6.

In strong crystal field environments, Cr^{3+} luminescence spectra are characterized by relatively sharp R-lines associated with the spin-forbidden ^2E-$^4A_2$ transition, with the $^4A_2$ state being the ground state and the ^2E state being split in non-cubic environments (Syassen 2008). At lower field strengths, the broader $^4T_2$-$^4A_2$ emission dominates. Relatively sharp neighbor lines (N-lines), generated by shared

excitations between neighboring Cr^{3+} centers, are also observed in many Cr^{3+} bearing compounds (e.g. Vink et al. 2000). These bands tend to be complex, since a wide variety of potential neighbor interactions exist in most 3-dimensional structures, and different pairs generate suites of lines for which the pattern depends on exchange parameters and whether ferromagnetic or antiferromagnetic pair interactions are present (e.g. Powell and DiBartolo 1972). If the pair-line assignments are known, their pressure-dependence can be used to estimate compaction-induced changes in magnetic exchange interactions between chromium centers (Williams and Jeanloz 1985). Lastly, vibronic emission bands are observed: these phonon-associated sidebands are offset from the R-lines by the frequency of a coupled vibrational mode, and the pressure dependence of these bands reflects the conflation of the shift of the primary electronic transition and the shift of the phonon mode, from which a mode Grüneisen parameter may be extracted.

Here, we use Cr^{3+} luminescence as both a probe of the Al and/or Mg sites in clinochlore under pressure, and as a tool to examine shifts in magnetic interactions between Cr^{3+} ions under compression. High-pressure luminescence spectra of clinochlore have not previously been reported. Thus, our experiments are oriented towards: (1) investigating the pressure dependence of the intensity and position of R-Line, N-Line and vibronic modes in a quasi-two-dimensional structure, and (2) characterizing the luminescence spectra across a known high-pressure polytypic transition in a layered structure (the response of Cr emission to a high-pressure rearrangement of the TOT and O layers in layered ceramics is unknown). Our net

goals are thus to constrain pressure-induced shifts in magnetic interactions between Cr^{3+} centers and determine the effects of compaction and structural rearrangements on the luminescence spectra of Cr^{3+} ions within the layers.

3.2 Experimental Methods

Our sample was a natural gem quality green clinochlore, with an ideal formula of $((Mg,Fe^{2+})_5Al(Si_3Al)O_{10}(OH)_8)$, from Murphys, Mariposa County, California (UCSC# 6278). Sample purity was confirmed by Raman spectroscopy and luminescence spectroscopy, which were in excellent agreement with previous studies (Prieto et al. 1991, 2003; Kleppe et al. 2003; Czaja et al. 2014). Trace element concentrations in the sample were measured with a PhotonMachines Analyte 193H, which is a 193 nm ArF excimer laser system coupled with a ThermoScientific ElementXR single-collector magnetic sector ICP-MS. The instrument was calibrated with a SRM 610 trace element glass from NIST. Mg, Fe, Al, Si, Ca, Ti, V, Cr, and Mn were measured and Al was used as an internal standard, and the results are presented in Table 3.1.

Element	Concentration (ppm)	Standard error
Fe	7402	2913
Ca	348	202
Ti	70	32
V	133	7
Cr	2963	74
Mn	58	31

Table 3.1. Trace element concentration of the clinochlore crystal utilized: some elemental zoning was likely present, but the zoning had little effect on the Cr abundances, implying that Cr is, within the size of the compositional probe, homogeneously distributed.

High static pressures were generated using a Merrill-Bassett type diamond anvil cell (DAC) equipped with 16-sided type Ia 500 μm culet diamond anvils. A spring steel gasket with a 200 μm hole was used as the sample compartment. Experiments were carried out with methanol:ethanol:water 16:3:1 and methanol:ethanol 4:1 mixtures as the pressure media, which yield hydrostatic conditions that range from ~9.2-15 GPa (Piermarini et al. 1973; Fujishiro et al. 1982; Angel et al. 2007; Klotz et al. 2009). A single crystal of clinochlore with dimensions of ~20x30x10 μm and a single crystal of ruby were loaded into the sample compartment. The *a*-*b* plane of clinochlore was perpendicular to the axis of compression for each experiment. The standard ruby luminescence method (Mao et al. 1986) was used to determine the pressure.

Luminescence spectra were collected from 650-800 nm (15380-12500 cm^{-1}) with a Horiba LabRAM HR Evolution Raman spectrometer with a spectrometer focal length of 800 mm. An 1800 lines/mm grating with a corresponding spectral resolution of ~1 cm^{-1} was utilized. Excitation at both 532 and 633 nm was used to collect room pressure spectra at 77 K and room temperature. Room pressure and temperature measurements down each crystallographic axis did not produce significantly different spectra. All high-pressure spectra were collected using an excitation wavelength of 532 nm. The excitation laser was oriented perpendicular to the *c*-axis during all high-

pressure measurements, and the sample remained a single crystal on compression to ~25 GPa and on decompression. An Olympus BXFM-ILHS microscope with a 50x long working distance objective was used to focus the laser beam onto the sample. Luminescence spectra were fit using a combination of Gaussian and Lorentzian functions with Horiba Labspec6 software.

3.3 Crystal structure and Cr distribution in clinochlore

The layered structure of clinochlore consists of two alternating layers, a tetrahedral-octahedral-tetrahedral (TOT) layer, often described as a talc-like layer, and an octahedral (O) layer, which has features in common with the brucite structure (Pauling 1930; Zanazzi et al. 2007) (Figure 3.1). It has been proposed, based on site characteristics coupled with crystal field splitting parameters derived from absorption spectra, that Cr atoms substitute primarily into the M1 or M2 sites within the TOT-layer (Zheng and Bailey 1989; Czaja et al. 2014) in green chlorites of the type we examine here. The likely confinement of Cr ions within a discrete quasi-2-dimensional layer dramatically limits the numbers and types of pair interactions between Cr ions that might produce luminescent neighbor lines. Indeed, even if Cr ions were present in both the TOT- and O-layers, pairing of chromium atoms between the layers is not likely, due to the distance between the atoms being > 7.0 Å, and the corresponding coupling across the layers likely being small relative to in-layer interactions. Moreover, since interactions between Cr ions are produced either through a direct interaction, via overlap of neighboring d-orbitals, or superexchange via pairing through an oxygen, it is not likely that significant pairing would occur

across the extended gap between layers. Unlike the gold cyanide compounds (Assefa et al. 1994), clinochlore is truly a layered structure with hydrogen bonding between layers (Figure 3.1).

The 2-dimensional layering of clinochlore generates three nearest neighbor pairs associated with octahedral sites in both the T-O-T layer and the O layer, each of which have two equivalent sites (Figure 3.2). The distances between the nearest neighbor pairs for each M-site are listed in Table 3.2. The number of nearest neighbors varies from two to as many as five depending on which site is being considered. However, some of the distances between adjacent sites vary from one another by as little as 0.001 Å, and emission from these pairs would thus probably be indistinguishable. We have used the M1 site to illustrate the configuration of nearest neighbors in Figure 3.2, but this configuration is the same for all the M sites within the clinochlore structure. If chromium substitutes into M1 or M4, then any Cr-pair emission must occur across multiple oxygen atoms (the distance between these sites is ~5.0 Å). If chromium substitutes only into M2 and M3, then these sites have slightly different configurations that generate three nearest neighbors, and pairing can occur across a single oxygen (the distance between these sites is ~3.0 Å). As shown by Czaja et al. (2014) and Zheng and Bailey (1989), the dominant substitution of Cr in the sample we probe is into the M1 and M2 sites. Importantly, the absolute chromium concentration will control the abundance of pairs: however, clustering of chromium ions could occur, which would enhance the abundance of pairs and neighbor line intensities. Whether such clustering is present is unclear from current

optical and x-ray diffraction measurements (Zheng and Bailey 1989; Czaja et al. 2014). High-pressure single-crystal X-ray diffraction data definitively show that cation configurations of the type shown in Fig. 3.2 continue to be stable up to at least ~4.9 GPa (Welch and Marshall 2001; Zanazzi et al. 2007) and Raman spectroscopic data suggests that no major bonding changes occur, and hence that the general layered configuration is stable, up to ~27 GPa (Kleppe et al. 2003).

Type of neighbor	Pair separation * (Å)	Number of equivalent sites	Pair separation* (Å)	Number of equivalent sites
TOT-layer	M1 site		M2 site	
first	3.071	2	3.070	2
second	3.078	2	3.078	1
third	3.080	2	3.080	2
fourth	-	-	3.088	1
O-layer	M3 site		M4 site	
first	3.073	1	3.076	2
second	3.076	1	3.077	4
third	3.077	2	-	-
fourth	3.078	1	-	-
fifth	3.080	1	-	-

Table 3.2. Nearest neighbor pair distances for the four octahedral sites. *Data from [(Zanazzi et al. 2007)].

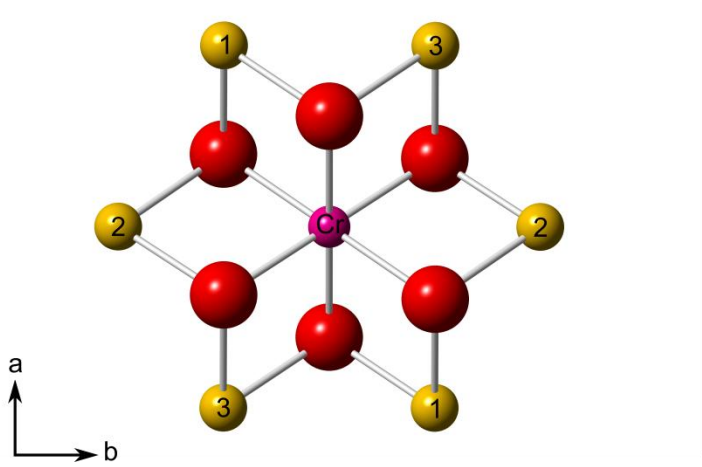

Figure 3.2. Nearest neighbor pair sites for chromium ion in the M1 site of clinochlore. This configuration is the same for M2, M3, and M4, however the distances between the nearest neighbors differ slightly between the different sites. Crystal structure after (Zanazzi et al. 2007). Diagram made in CrystalMaker®.

3.4 Fe content and Cr^{3+} emission

The Fe content of ~7400 ppm, in tandem with our luminescence observations, is novel (Table 3.1), since Fe is typically the strongest quencher of visible luminescence in minerals (Gaft et al. 2005). For example, in the case of ruby containing 0.05 wt% Cr, R-line emission is entirely quenched when it is co-doped with ~2.0 wt% Fe (Yu and Clarke 2002). Yet, in clinochlore, the high-concentration of Fe does not quench the R-line emission: although Czaja et al. (Czaja et al. 2014) attributed the relatively short Cr^{3+} luminescent lifetimes in clinochlore to energy transfer to iron ions. The quenching of R-line emission in ruby is related to the $^4T_2(^4G)$ transition of octahedrally coordinated Fe^{3+} at ~14350 cm^{-1} (Lehmann and Harder 1970). Hence, the typical R-line emission (~14404 cm^{-1}) is absorbed by this transition and re-emitted as a broad feature in the near infrared. Fe does not always totally quench R-line emission in ruby: a broad luminescence band at ~770 nm occurs

with the R-line emission in Al_2O_3 and has been assigned to a Cr-Fe interaction (Snytnikov et al. 2008). The lack of quenching of R-line emission in iron-bearing clinochlore, despite its high Fe content, may stem from one of two effects: (1) Fe atoms are spatially separated from the chromium centers within the structure, or (2) the absorption bands (or oxidation state) of Fe in layered silicates may differ from those in 3-dimensional oxide structures such as ruby. Neither the spatial distribution of Fe nor of Cr in clinochlore are well understood, but since Fe is thought to substitute into both the TOT- and O-layers (Zheng and Bailey 1989), it is unlikely that Fe and Cr sites would be markedly spatially separated. Thus, the absorption bands of Fe in layered structures probably do not lie close to the Cr R-line emissions (R_2 at ~14755 cm^{-1} and R_1 at ~14649 cm^{-1}). Optical absorption spectra of a wide variety of layered silicate structures (e.g., nontronite, biotite, muscovite, phlogopite, and chlorite) indicate that the absorption bands of octahedrally coordinated Fe^{2+} and Fe^{3+} and tetrahedrally coordinated Fe^{3+} are shifted shorter wavelengths from where they lie in non-layered oxide minerals (Faye 1968; Karickhoff and Bailey 1973; Bonnin et al. 1985). Hence, this offset plausibly shifts the major Fe absorption bands away from the Cr^{3+} emission, and the sharp R-line emission is thus not quenched by Fe absorption; this is in accord with previous lifetime measurements (Czaja et al. 2014). Fe may, however, operate as an inefficient non-radiative trap.

3.5 Results and Discussion

3.5.1 Ambient Pressure Spectra

Characteristic luminescence spectra of clinochlore at room pressure and temperatures of 298 and 77 K for two excitation wavelengths are shown in Figure 3.3. At room temperature and pressure, split sharp R-line emissions with an R_2 line at 677.7 nm and R_1 at 682.6 nm, a broad $^4T_2$-$^4A_2$ transition at ~720 nm, N-lines (emission from Cr-Cr pairs), and phonon sidebands are observed in the spectra excited with 532 nm excitation. These spectra are in good accord with those of Czaja et al. (Czaja et al. 2014), although their sideband amplitudes are somewhat lower; our assignments also agree with those of Czaja et al. (Czaja et al. 2014), although we resolve more N-lines and vibronic peaks.

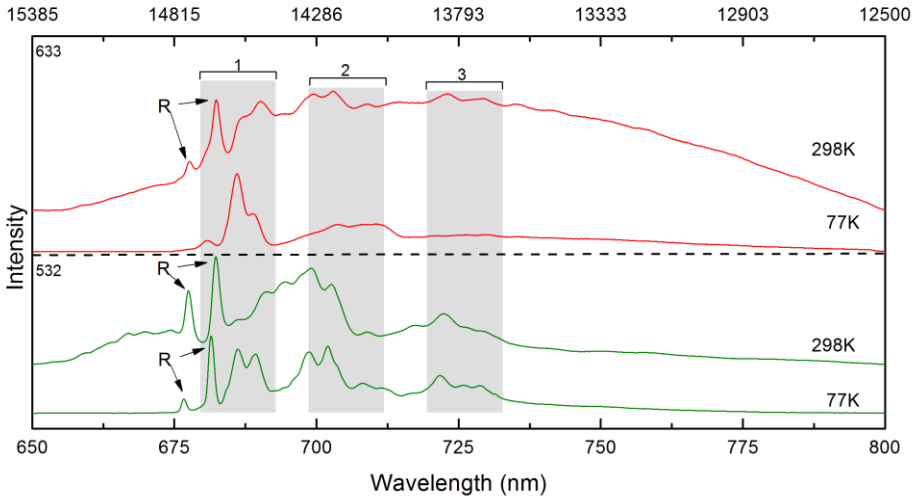

Figure 3.3. Room pressure 298K and 77K luminescence spectra of clinochlore under 532 (bottom) and 633 nm (top) excitation. The brackets with numbers indicate the regions in the spectra where the exchanged coupled pairs of Cr^{3+} ions emit. Energy levels and assignment of these N-lines are discussed in the text. Notably, the intensities of the N-line and the $^4T_2$-$^4A_2$ transition each strongly depend on excitation wavelength.

The observation of a broad $^4T_2$-$^4A_2$ transition coexisting with the R-line emission and its location within ~1000 cm^{-1} of the ^2E-$^4A_2$ associated R-lines suggests

that the Cr in clinochlore is in an intermediate strength crystal field environment, in accord with the Tanabe-Sugano diagram for a d^3 system (Tanabe and Sugano 1954). The presence of the broad $^4T_2$-$^4A_2$ emission (which represents a superposition of this transition and the vibronic sidebands of the R-lines) becomes particularly apparent under 633 nm excitation at 298 K (Figure 3.3), likely because the absorption associated with this transition lies near 600 nm (Czaja et al. 2014). Hence, 633 nm excitation pumps this transition more effectively than 532 nm excitation; the strong temperature dependence of its amplitude under 633 nm excitation indicates that the $^4T_2$ band's occupation is thermally induced. It is possible that the energy of the $^4T_2$ to $^4A_2$ transition may also be temperature dependent, but our data do not constrain this possibility (e.g., Fonger and Struck 1975). The location of the broad $^4T_2$ emission band at ~720 nm at room pressure and temperature under 633 nm excitation (Figure 3.3) is at substantially longer wavelength than the corresponding absorption of this transition at ~600 nm (Czaja et al. 2014), demonstrating that the excited state of this transition is Stokes shifted to the long wavelength side of the R-lines, a phenomenon that is well-documented in, for example, emerald and ruby (Kisliuk and Moore 1967). Notably, the variable excitation results show a dramatic intensity enhancement of a neighbor line near 686 nm under 633 nm excitation at 77 K (Figure 3.3): the R-line becomes a small fraction of its relative intensity, and this neighbor line, along with a lower energy shoulder at ~691 nm, become the dominant features of the emission spectrum. Such an intensity enhancement at low temperatures was observed under broad-band excitation by Czaja et al. (Czaja et al. 2014), but our results show that 532

nm excitation continues to excite the R-lines at low temperatures. Such neighbor-line enhancement as a function of excitation wavelength is well-documented in Cr-bearing spinels (Mikenda and Preisinger 1981), and is observed particularly as the wavelength of excitation closely approaches the R-lines. As a result, we utilize 532 nm excitation in our high-pressure studies because of both its distance from the R-lines and its location on the broad single-ion $^4A_{2g}$ -> $^4T_{2g}$ absorption peak (Czaja et al. 2014).

The appearance of the R-lines at 298 K with 633 nm excitation reflects that the ^2E states (and the $^4T_2$ state) become thermally populated at this temperature, while the N-lines whose intensities are augmented at 77 K remain higher amplitude than with 532 excitation, but they no longer dominate the spectrum. The N-lines of clinochlore were identified based on the dependence of their intensity on excitation wavelength (Mikenda and Preisinger 1981), and our assignments of them to different pair manifolds are discussed in detail below.

3.5.2 Luminescence Spectra under Pressure

Luminescence spectra of clinochlore have been collected on compression up to ~25 GPa and on decompression to room pressure (Figure 3.4). The pressure shifts of the R-lines, N-lines and phonon sidebands are plotted in Fig. 3.5. The pressure shift up to the ~6.0 GPa polytypic transition, and the offsets of the different sidebands from R_1 are listed in Table 3.3. The R-lines can be fit well by single peaks, which suggests that, if Cr^{3+} enters into multiple sites, the lattice distortion associated with Cr^{3+} substitution in these sites is essentially identical: that is, multiple R-lines are not required to fit the spectrum. However, the M-site volumes in clinochlore (M1 is 11.80

$Å^3$, M2 11.79 $Å^3$, M3 10.93 $Å^3$ and M4 10.65 $Å^3$: (Zanazzi et al. 2007)) markedly vary. Hence, the appearance of sharp, single component R-lines is consistent with Cr^{3+} substitution dominantly into one subset of similar sites, which is almost certainly the M1 and M2 sites. That two to four sets of R-lines are not observed is consistent with the Cr^{3+}-bearing M1 and M2 sites having essentially indistinguishable R-line locations, and their Cr^{3+} internal site geometry and electron densities being essentially the same.

Assignment	λ (nm)	ν (cm^{-1})	Δν (cm^{-1})	*dv*/*dP* (cm^{-1}/GPa)
^{2}T?	667.0	14993.6		-22.5 (±1.3)
^{2}T?	670.6	14911.8		-19.0 (±1.2)
^{2}T?	674.4	14828.7		-18.7 (±0.6)
R_2	677.7	14755.4		-18.4 (±0.3)
N-line	679.9*	14693.1		-17.4 (±0.6)
R_1	682.6	14650.5		-18.0 (±0.2)
N-line	686.2	14572.3	78.2	-11.0 (±0.7)
N-line	691.2	14468.4	182.1	-8.8 (±0.5)
N-line	694.5	14399.5	251.0	-21.1 (±0.8)
Vibronic?	698.3	14321.7	328.8	-25.7 (±0.7)
N-line	699.27	14300.6	349.9	-20.0 (±0.8)
Vibronic?	702.8	14228.6	421.9	-23.2 (±0.4)
N-line	709.0	14103.8	546.7	-21.4 (±0.7)
N-line	713.2*	14018.2	632.3	-18.2 (±1.1)
N-line	717.9	13928.7	721.8	-15.2 (±0.8)
$^4T_2$?	720.5*	13875.8	774.7	-17.3 (±1.0)
N-line	723.0	13830.9	819.6	-16.9 (±1.0)
N-line	726.7	13760.1	890.4	-17.6 (±0.8)
N-line	729.3	13712.7	937.8	-17.2 (±0.8)
N-line	732.4	13653.6	996.9	-15.6 (±0.4)

Table 3.3. Pressure shifts of R-lines, N-lines, and sidebands up to the ~6.0 GPa polytypic transition. Assignment of vibronic modes based on pressure shifts and bands in the Raman spectra of (Prieto et al. 1991; Kleppe et al. 2003). *Lines observed at high pressures have been extrapolated back to room pressure.

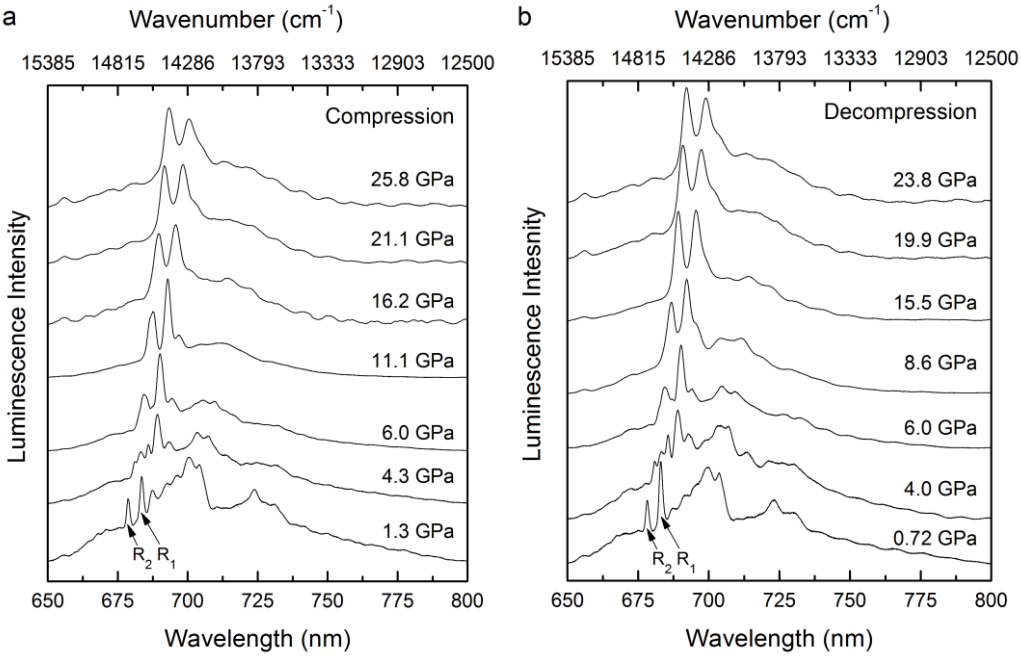

Figure 3.4. High-pressure luminescence spectra of clinochlore (a) compression and (b) decompression, collected using 532 nm excitation. Spectra on decompression are selected to emphasize the reversibility on decompression.

Both R-lines shift linearly and positively (to longer wavelength) up to ~6.0 GPa (Figure 3.5b). Above ~6.0 GPa, the initially intense R-lines become difficult to fit due to a progressive increase in intensity of N-line associated bands, and ultimately they become too weak to resolve above ~12.0 GPa. Above ~12.0 GPa, the N-line emission dominates the luminescence spectra up to the maximum pressure of this study (~25 GPa). Notably, the shifts in relative intensities of the R- and N-lines are fully reversible on decompression.

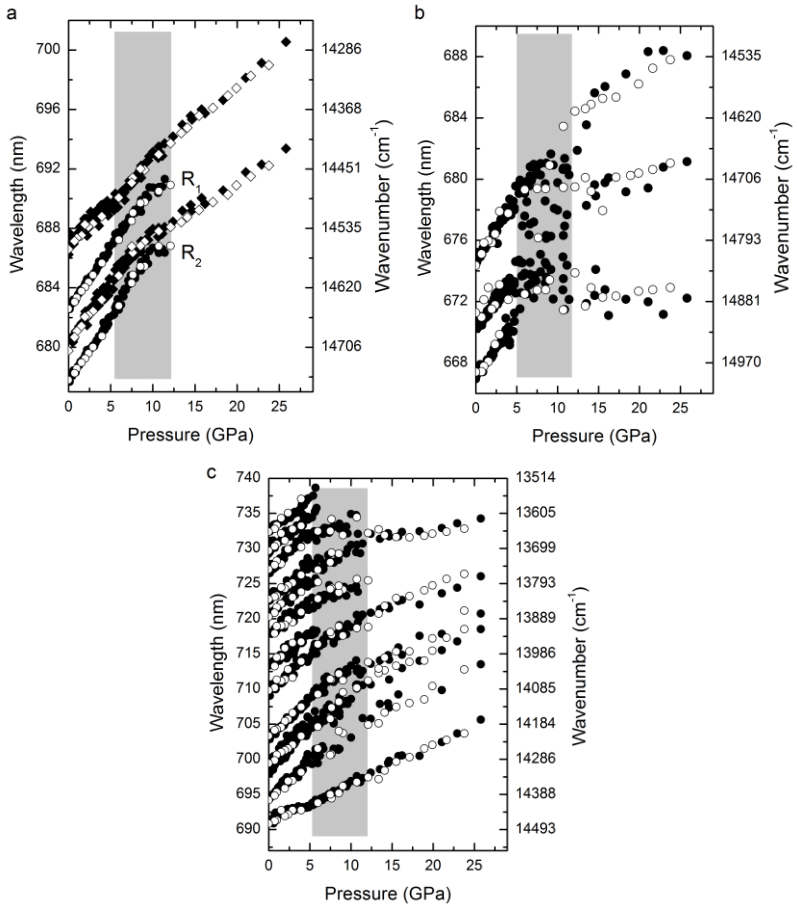

Figure 3.5. Pressure shift of luminescence bands on the (a) the R-line region; (b) high energy side of the R-lines; and (c) low energy side of the R-lines. Grey box represents the region where R-line and N-line intensities approach one another: in this region, vibronically coupled bands become notably difficult to track. Closed symbols are data on compression, open symbols on decompression, and error bars are smaller than the symbols.

In terms of the weaker sidebands, three bands are resolvable on the high-energy side of the R-lines and each shift to longer wavelength with pressure at rates that modestly narrow their separation from the R-lines (Figure 3.5a, Table 3.3). These bands become difficult to track between ~5.0 and 12 GPa, and thus become notably scattered. However, they do appear to have markedly decreased pressure shifts above

the ~6.0 GPa polytypic transition (Figure 3.5b). The assignment of these bands is unclear: their pressure shifts are not in accord with hard-mode vibronic peaks. It is possible that, as within the emission spectrum of alexandrite (Walling et al. 1980), they represent the three components of the $^2T_1$ to $^4A_2$ transition.

In the sideband region to the lower energy side of the R-lines (Figure 3.5c), the N-lines, the $^4T_2$-$^4A_2$ band, and likely vibronic modes also shift to longer wavelength. The pressure shift of the N-lines varies between nearest neighbor pairs which is consistent with previous studies on ruby (Merklei et al. 1981; Williams and Jeanloz 1985). The vibronically coupled modes become difficult to track between 6 and 11 GPa: this is certainly due to the amplitude shift from the R- to N-line emissions. Above 12 GPa, the vibronic peaks are anticipated to be frequency-offset from the dominant N-line(s), rather than the R-line(s): this inference is based on the much stronger intensity of the N-line(s), but also depends on the unknown coupling between vibrational modes and the N-line(s). Interestingly, no discontinuous shifts in R- or N-line emission energies, or in the vibronically coupled modes are observed across the ~6.0 GPa polytypic transition documented in clinochlore using x-ray diffraction (Welch and Crichton 2005). Neither are significant changes in R- or N-line emission intensity observed across the ~6.0 GPa polytypic transition. The only spectroscopic manifestations of this transition are (1) a discontinuous shift in R-line separation (ΔE_d) at ~6.0 GPa (Figure 3.6), which is driven largely by a shift in the position of the R_2 band (Figure 3.5b); and (2) a decrease in the rate at which the separation between the R_1 band and the highest amplitude N-line decrease (Figure

3.7). Thus, a modest decrease in distance and lateral shift of the TOT- and O-layers relative to one another have only a small effect on the local bonding or electron density of the Cr-sites. This suggests that the luminescence of Cr^{3+} ions that are isolated within a single layer is a rather insensitive probe of transitions involving changes in the orientation/lateral offset of layers relative to one another. Since the polytypic transition primarily involves changes in bonding 5-7 Å away from the layer containing the Cr ions, this lack of sensitivity is not surprising.

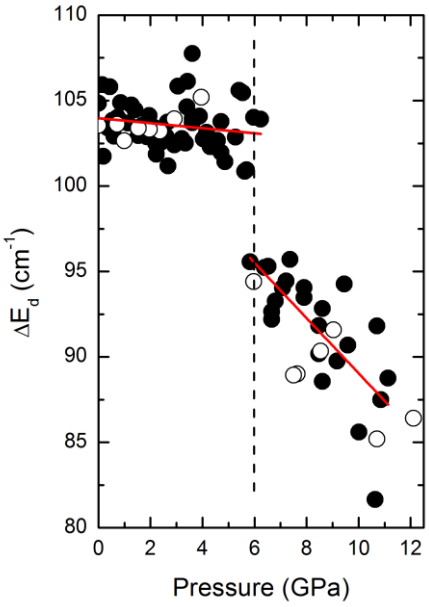

Figure 3.6. ΔE_d of clinochlore under compression up to ~12 GPa. Vertical dashed line indicates the pressure of the polytypic transition. Linear fits are guides to the eye. Solid symbols are on compression, and open symbols are on decompression. Error bars are smaller than the size of the symbols.

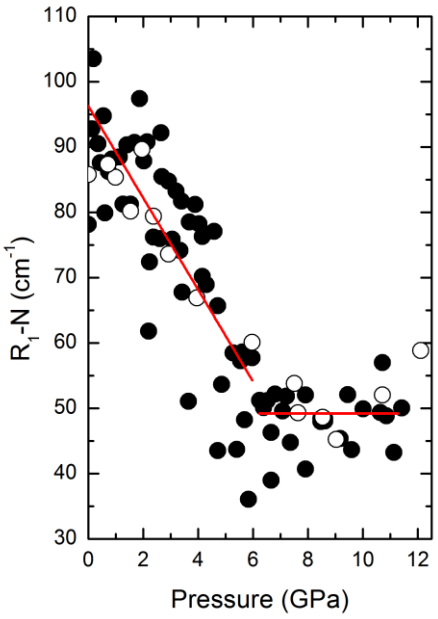

Figure 3.7. R_1 and primary N-line separation from one another. Closed symbols are compression, open symbols are decompression, solid lines are to guide the eye.

The discontinuous decrease in the splitting between the two components of the R-line (Figure 3.6) is largely generated by a non-linear shift in the R_2 line near the transition (Figure 3.5b). This splitting of the ^2E state is interpreted as an indicator of site distortion, with larger values of splitting suggesting a more highly distorted site. For example, ruby has a Cr site which has a slight trigonal distortion and an R-line splitting of ~29 cm^{-1} (Maiman 1960), while zoisite ($Ca_2Al_3Si_3O_{12}(OH)$) has a highly distorted Cr site with an R-line splitting of ~350 cm^{-1} (Koziarska et al. 1994): one of the largest such splittings known. Clinochlore at ambient conditions has an R-line splitting of ~105 cm^{-1}, and single crystal diffraction data show that the Cr sites in clinochlore (Figure 3.1) have an intermediate distortion between those of ruby and zoisite (Zanazzi et al. 2007). Under compression up to ~6 GPa, the observed R-line

splitting decreases at a rate of -0.19 ± 0.13 cm^{-1}/GPa (Figure 3.6), suggesting that the Cr site becomes slightly less distorted up to ~6.0 GPa. Above 6 GPa, the R-line splitting decreases more rapidly (at -2.15 ± 0.40 cm^{-1}/GPa), suggesting that the site becomes less distorted at a more rapid rate within the higher pressure polytype.

The full width at half maximum (FWHM) of the R-lines decreases slightly up to the ~6.0 GPa polytypic transition (Figure 3.8). Above ~6.0 GPa, accurate fitting of the R-lines becomes difficult due to both the decreases in intensity and the increased intensities of both the N-line and $^4T_2$ emissions. Thus, while peak positions of the R-lines can be determined above ~6.0 GPa, the FWHM of the R-lines can no longer be resolved reliably. The decrease in FWHM to 6 GPa is most likely due to the larger pressure shift of the vibronic modes relative to the R-lines, as the pressure-dependence of R-line peak width follows a Debye relation (Kottke and Williams 1983). The increased separation between the R-lines and vibronically coupled modes with pressure implies that the coupling of phonons with the R-lines decreases over the pressure range of these measurements, and hence the peak width of the R-lines is expected to decrease.

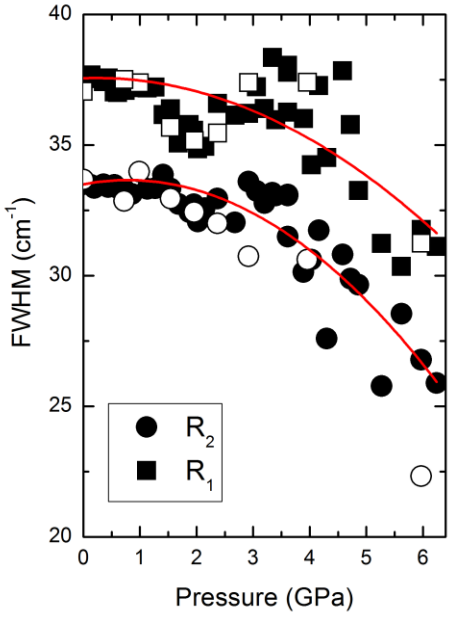

Figure 3.8. Full width at half maximum (FWHM) vs pressure of the R-lines in clinochlore; square symbols are R_1 and circles are R_2. There is an overall slight decrease in the width of the R-line emission under compression, and this decrease may be non-linear with pressure. Closed symbols are on compression and open symbols are on decompression, and lines are to guide the eye.

The high-pressure diffraction data on clinochlore are inconsistent with one another on the response of the octahedral sites to compression, and hence the structural changes that generate both the R-line shifts and their shift in splitting are difficult to assess from these data. High-pressure single crystal data up to 4.85 GPa indicate that under compression the M-sites in both the TOT- and O-layers both tilt and become more regular (less distorted), which results in a net *increase* in their volume under compression (Zanazzi et al. 2007). In contrast, Rietveld refinements of a deuterated clinochlore sample under compression result in a *decrease* in volume of the M-sites at least up to 4.65 GPa (Welch and Marshall 2001). We have no simple explanation for this first-order discrepancy in the high-pressure structural data, but

note that this difference is very unlikely to be associated with deuteration: for example, the high-pressure behavior of δ-AlOOH and δ-AlOOD are nearly identical (Sano-Furukawa et al. 2009). Notably, high-pressure structural determinations of layered silicate structures are notoriously difficult, due to the typical orientation of these samples in the pressure apparatus with their *c*-axis parallel to the axis of compression. Hence, changes in atomic positions in the *c*-direction can be difficult to constrain. Notably, the high-pressure unit cell parameters and volumes reported by Zanazzi et al. (Zanazzi et al. 2007) and Welch and Marshall (Welch and Marshall 2001) are very similar: yet they differ markedly in the internal coordinates associated with the structure. Importantly, Kleppe et al. (Kleppe et al. 2003), in their Raman study of clinochlore under compression, report an anomalously small pressure shift of the Raman active $v_5(F_{2g})$ MO_6–stretching mode (0.119 cm^{-1}/GPa), which is consistent with the octahedral sites minimally decreasing in volume under compression up to 5.26 GPa. Within oxides, the general trend is that R-lines shift to longer wavelength as site volume decreases (Mao et al. 1986; Wamsley and Bray 1994; Hua et al. 1996). Our luminescence data thus are consistent with the volume of the chromium sites decreasing under compression. Yet, site compressibility and geometry are not the sole factors that contribute to the pressure shift of the R-lines: the electron density around the Cr^{3+} atom plays a primary role in the behavior of R-line luminescence under pressure. Since hydrogen bonding in clinochlore appears to weaken under compression (Kleppe et al. 2003), a net increase in electron density around the Al-site (into which the Cr substitutes) is expected as pressure is increased (as H atoms move

closer to the O-layer: Figure 3.1). Thus, shifts in electron density could be manifested as a positive shift of the R-lines, in a manner that is complementary to the shift generated by a decrease in the volume of the Al-site under increased pressure.

3.5.3 Cr-Pair Coupling and N-line Assignments

Czaja et al. (Czaja et al. 2014) have noted that significant pair-line emissions are present in the emission spectrum of clinochlore, and our luminescence results (Figure 3.3), under different excitations, confirm their presence. Indeed, Cr-Cr pair emission in the vicinity of the R-lines has been observed in oxides such as ruby Al_2O_3 (Kisliuk et al. 1969; Powell and DiBartolo 1972), $LiNbO_3$ (Kamińska et al. 2007), $LiGa_5O_8$ (MacCraith et al. 1982), $BeAl_2O_4$ (Powell et al. 1985), a suite of oxide spinels and perovskites (McCarthy and Gudel 1988), and in silicates such as zoisite $Ca_2Al_3Si_3O_{12}(OH)$ (Koziarska et al. 1994). As originally shown in ruby, a simplified theory of isotropic exchange can accurately describe the ground state splittings of Cr-Cr pair systems (Powell and DiBartolo 1972). The neighbor line interactions can be described using an exchange type interaction Hamiltonian,

$$H=Js_1 \cdot s_2 \qquad (1)$$

where s_1 and s_2 are the total spins of ion 1 and ion 2 respectively, and J is a coupling constant. However, simple isotropic exchange theory fails if an electron on one of the ions of the pair is in the excited ^2E state, and the Hamiltonian given in equation (1) is not valid (Kisliuk et al. 1969; Powell and DiBartolo 1972). In order to account for the different states of the two coupled ions, a more general interaction Hamiltonian is used:

$$H=\Sigma J_{ij}\, s_{1i}\cdot s_{2j} + j\,(s_1.s_2)^2 \qquad (2)$$

Here, J, s_1 and s_2 are the same as in (1), and i and j run over the three one-electron t_{2g} orbitals on each ion, and the second term involves a biquadratic correction to account for polarization effects on a nonmagnetic ion (oxygen) located between the pair. Powell and DiBartolo (Powell and DiBartolo 1972) note that J and j (the biquadratic exchange interaction term) are treated as adjustable parameters for which the meaning of their magnitude is unclear (beyond reflecting spin coupling mechanisms), and they note that typical experimental values of J and j are substantially greater than predicted by theory. For ruby, superexchange is the accepted coupling mechanism of Cr-Cr pairs (Anderson 1959; Goodenough 1960; Laurance et al. 1962; Osmond 1962; Kisliuk et al. 1969; Lyo 1971; Powell and DiBartolo 1972).

Resolving a relatively large number of N-lines allows us to assign them to different pair manifolds in accord with Eqn. 2. The assignment of the N-lines was based on low temperature measurements as well as the measurements using 633 nm excitation (Figure 3.3). Under 633 nm excitation and low temperatures, some of the N-line intensities increase dramatically relative to the R-lines: this is most obvious in the 77 K spectrum where the R-line emission is almost entirely absent and N-line emission predominates (Figure 3.3). High amplitude N-Lines are observed at 680.6, 686.2, and 691.2 nm: this assignment and observation agrees well with the ambient pressure spectra and interpretations of Czaja et al. (Czaja et al. 2014). These lines can be fit, along with an additional line at 694.5 nm, to transitions within a single pair manifold using Eqn. 2. For ferromagnetically coupled Cr^{3+} ions, the energies of lines

arising from a single pair fall in a sequence of 0, 3*J*, 5*J*, and 6*J*, where the coupling constant *J* is negative for ferromagnetic coupling (Kisliuk et al. 1969; Powell and DiBartolo 1972). At least eight other weaker pair lines are observed (Table 3.3): these additional eight lines can be similarly fit to two additional pair manifolds (Figure 3.9). Thus, in accord with the existence of the three possible pair interactions that are shown in Figure 3.2, the N-lines observed can be modeled in terms of three ferromagnetically coupled distinct pairs of Cr^{3+} ions. Nevertheless, the strongest neighbor lines are clearly associated with the first ferromagnetically coupled pair in Figure 3.9, with weaker lines being associated with the other two. We have no simple explanation for the large relative intensities of the neighbor lines associated with this first pair, beyond noting that it may be associated with the abundance of these pairs. Although the absolute values of the excited state energies differ (Figure 3.9), the values of the exchange interaction constants, and hence the inter-Cr ferromagnetic coupling, are similar in two of the three pair manifolds that we identify in clinochlore (Table 3.4). The estimated values of the exchange parameters, as derived from the shifts in Figure 3.5 and the energy-level assignments of Figure 3.9, are also shown in Table 3.4 at ambient pressure and 4.9 GPa. Not all neighbor lines observed below 5 GPa can be resolved at higher pressures, so distinguishing the pressure dependence of the exchange parameters is difficult, beyond noting that they all decrease in value up to 5 GPa (Table 3.4).

Pressure (GPa)	Exchange parameters for pairs 1-3		
0.0001	J_1= -50.8 cm^{-1}	J_2= -59.6 cm^{-1}	J_3= -29.2 cm^{-1}

4.9	J_1= -35.2 cm^{-1}	J_2= -48.8 cm^{-1}	J_3= -26.0 cm^{-1}

Table 3.4. Exchange parameters at various pressures and room temperature used to determine the energy levels in Figure 3.9 of the three ferromagnetically coupled pairs of Cr^{3+} ions.

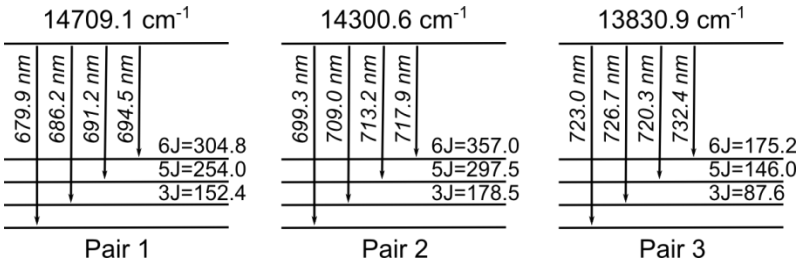

Figure 3.9. Energy level diagrams for three ferromagnetically exchange-coupled pairs of Cr^{3+} ions in clinochlore that fit the observed neighbor lines at ambient pressure. The multiples of the exchange parameter are given in units of cm^{-1}.

3.5.4 Transition from R- to N-line dominated emission

Under compression, the R-line emission decreases in intensity while the N-line emission increases in intensity (Figure 3.4); an expanded view of this transition is shown in Figure 3.10. This apparent transfer of relative intensity between the R- and N-lines is exponential up to ~6.0 GPa (Figure 3.11). The reversibility of the transition and general lack of hysteresis indicate that this transition is purely electronic in character (e.g. produced by changes in orbital overlap due to fully reversible changes in the geometry of the Cr sites). The transition is unusual: to our knowledge, a transition from R-line to N-line dominated emission under pressure has not previously been reported. Yet, energy transfer from R-lines to N-lines via rapid, non-radiative transfer processes has long been recognized in ruby (e.g., Imbusch 1967),

with the likely mechanism for this transfer being orbitally-dependent exchange (Birgeneau 1969).

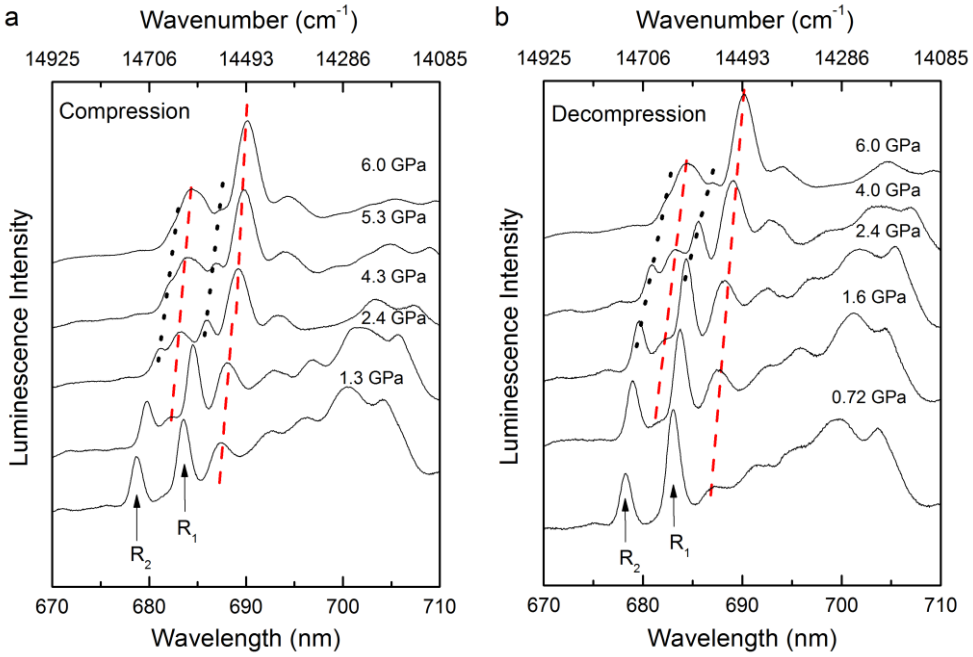

Figure 3.10. Detail of the R-line region showing the transition from R-line dominated to N-line dominated emission on (a) compression and (b) decompression. By ~6 GPa the transition to N-line dominated emission is nearly complete, but R-lines can be fit within the spectra up to ~12 GPa. Dotted Lines (black) indicate R-lines, and dashed lines (red) indicate N-lines.

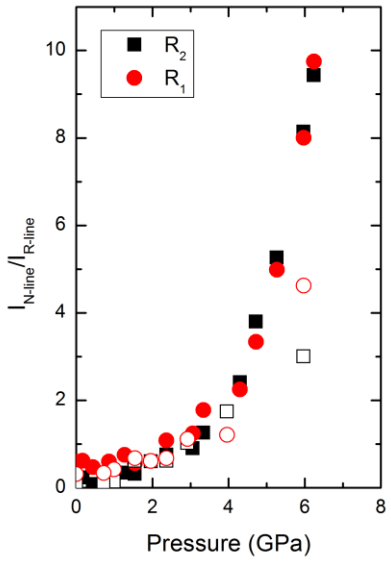

Figure 3.11. N-line intensities divided by the intensity of the R-lines that they replace at high pressure. Closed symbols are on compression, open symbols on decompression.

Cr-Cr exchange can occur by direct cation-cation transfer, or indirect cation-anion-cation transfer (van Gorkom et al. 1973). In ruby, the first four types of Cr-Cr pairs occur across a single oxygen ion; pairing across two oxygens begins with the fifth-neighbor pairs. The exchange interactions associated with multiple anions are small, and give rise to a high density of low-amplitude transitions near the R-lines (Kisliuk et al. 1969). Thus, the pairing that is resolved in the luminescence spectrum of clinochlore is very unlikely to occur across layers, both due to the distance and the multiple oxygen ions through which the interaction would occur. The Cr pairing we observe must occur entirely within the TOT and/or O layers, and Figure 3.2 describes the nearest interactions spanning a single oxygen ion that can occur between octahedral sites in these layers. As an important ancillary note, the concentrations of other transition metal elements, such as V, Mn, and Ti, are low enough (Table 3.1)

that any possible pairing and energy transfer between Cr^{3+} and these elements would likely result in weak (if any) emission lines. The octahedral sites in clinochlore are edge sharing, and compounds with ferromagnetic interactions between edge sharing Cr sites typically have nearest-neighbor exchange interactions that are produced by close-to-90^{o} super-exchange between Cr ions. The strength of the exchange is not only determined by the Cr-Cr distance, but also the Cr-O-Cr bond angle (Motida and Miyahara 1970; Shapira and Bindilatti 2002). Hence, the neighbor lines that grow into, and eventually dominate, the high-pressure spectra likely have their intensity modulated by the precise geometric interactions associated with adjoining octahedral sites in clinochlore. Fig. 3.12 shows the detailed deformation of the octahedral sites under compression to ~6.0 GPa, as derived from the single crystal data of Zanazzi et al. (Zanazzi et al. 2007). Notably, these deformations are those undergone by octahedral sites containing Al; the degree of local structural relaxation accompanying substitution of the larger Cr-ion into these sites is not well-constrained (Ardit et al. 2014).

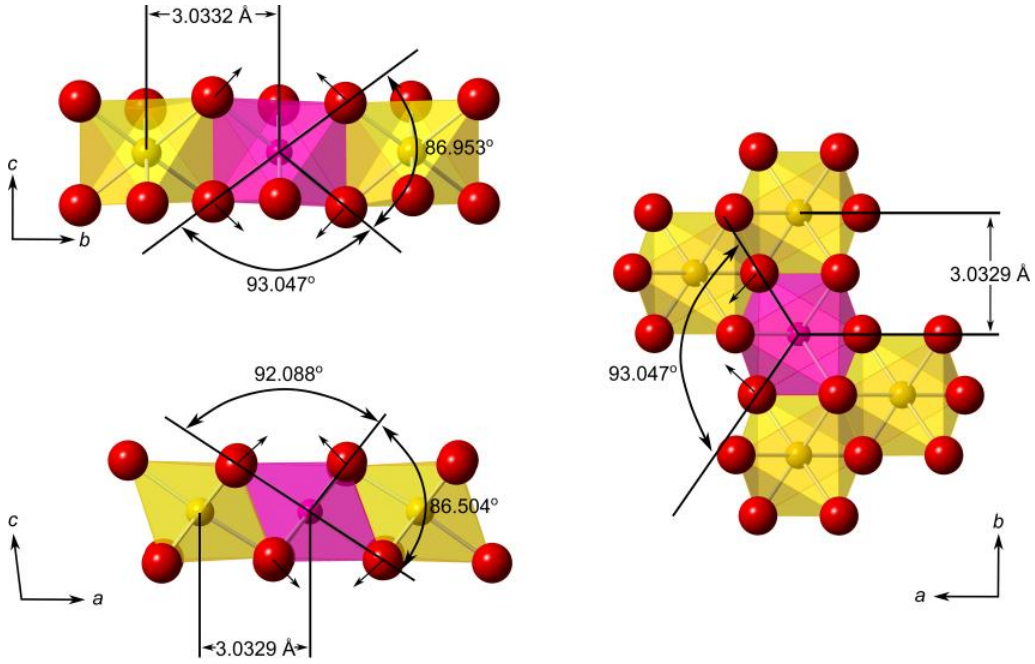

Figure 3.12. Bond angles and distance between M1 and M2 sites at 4.9 GPa looking down each crystallographic axis. While this figure is centered on the M1 site, in the TOT-layer the same changes occur in the M3 and M4 sites in the O layer. Crystal structure diagrams made in CrystalMaker® using structural data from (Zanazzi et al. 2007).

Our observation of decreased splitting between the R-line components indicates that over the pressure range of these measurements site distortion is *decreasing* (Figure 3.6), and it is notably more rapid above the ~6.0 GPa polytypic transition. High-pressure single-crystal data have not been reported for clinochlore above ~6 GPa, so the exact changes that occur in the Cr sites (or, indeed, within the layers) are unknown above this transition. However, our high-pressure luminescence data show that a transition to N-line dominated emission initiates below 2 GPa (Figure 3.10), and is essentially complete as pressure is raised above ~6.0 GPa. Given the subtle structural differences between the low- and high-pressure polytypes (Welch

and Crichton 2005), the approach of the octahedral sites towards a more ideal geometry above ~6.0 GPa probably, to first order, continues the approach towards ideal octahedra that occurs from room pressure to ~6.0 GPa (Figures 3.6 and 3.12), albeit at a more rapid rate. Thus, a rapid increase in the e_g orbital overlap likely proceeds progressively with pressure, and is enhanced above ~6.0 GPa. Hence, the combination of Cr atoms moving closer together, Cr-sites becoming closer to ideal octahedral geometry (with Cr-O-Cr bond angles becoming closer to 90^o), and an increase in overlap of the excited e_g state lead to an enhancement in intensity of the Cr pair emission. Moreover, the separation between the single-ion R-lines and the N-line pair emissions that eventually dominate the emission spectra *decreases* under compression (Figure 13). This decreased energy separation may enhance the ability of excitation to be non-radiatively transferred from single-ion to pair traps (Imbusch 1967; Birgeneau 1969; Chu et al. 1981). Although the N-line intensities increase exponentially in the low-pressure phase of clinochlore (Room P to ~6.0 GPa: Figure 3.11), the N-line intensities continue to increase above ~6.0 GPa, with the R-lines ultimately becoming unresolvable above ~12 GPa.

The two-dimensional configuration of the layer in which the chromium atoms are present, and the way the sites deform under compression, appear to play key roles in the transition from single-ion to pair-line dominated emission (Figure 3.12). Notably, the Cr-Cr pair interactions occur entirely in the *a-b* plane due to the layered nature of the structure (Figure 3.2). Under compression to ~4.9 GPa, the slight rotation of the M-sites and an associated systematic change in bond angles (Zanazzi

et al. 2007) result in a decrease in overall site distortion, with Cr-O-Cr bond angles approaching 90^o; the distance between adjacent sites also decreases. Thus, the detailed geometric changes that occur under pressure may lead to an enhancement of the 90^o super-exchange interaction between adjacent Cr-sites.

Other structural changes under compression may also play roles in enhancing single ion to pair energy transfer. Transfer from single ion to pairs occurs nonradiatively, and the efficiency of the transfer mechanism is generated by the transfer of excitation between single ions, or from a single ion to a pair trap (Imbusch 1967; Birgeneau 1969; Jessop and Szabo 1980; Chu et al. 1981). The decreases in distance between octahedral sites within the TOT- and O-layers induced by pressure (Welch and Marshall 2001; Zanazzi et al. 2007) may enhance this transfer. Since similar transfers in intensity have not observed under compression in other Cr^{3+}-bearing luminescent phases, a combination of the geometry and the two-dimensionality of the clinochlore system likely plays a primary role in enhancing Cr-Cr superexchange interactions.

The relative intensity of the N-line emission relative to the R-line emission can be described by the proportionality

$$I_N/(I_N+I_R) \alpha (N_p/N_s)P_T \qquad (3)$$

(e.g., Imbusch 1967). Here, N_p and N_s are the number of pairs and single ions, respectively, P the transfer rate of excitation between single ions and pairs, and □ is the lifetime of the single ion emission. The numbers of pairs and single ions should not be changed by pressure, and hence is constant. Single-ion emission lifetimes of

Cr^{3+} ions in oxides typically increase by a factor of several over a pressure range of tens of GPa (e.g., Sato-Sorenson 1986; Eggert et al. 1989; Jovanic 2000). The factor of 30-50 increase in relative neighbor line intensity over a pressure range of 6 GPa (Figure 3.13) hence can be attributed to pressure-induced shifts in the energy transfer rate between single-ions and pairs under compression. The characteristic distance dependence of P in Eqn. 3 is expected to vary as r^{-n}, with r being the distance of transfer, where n is 6 for electrostatic dipole-dipole interactions, 8 for dipole-quadrupole interactions, and 10 for quadrupole-quadrupole interactions (e.g., Dexter 1953; van Uitert 1967). Alternatively, exchange phenomena may cause P to scale with distance as exp(-2r/L), where L is an average effective Bohr radius for the excited and unexcited states. Figure 3.13 shows a log-log fit to our intensity data as a function of the pressure-induced variation in Cr-Cr separation within the crystal, with distances derived from the high-pressure single crystal measurements of (Zanazzi et al. 2007). We utilize the scaled Cr-Cr separations both because these can be viewed as reflecting the compaction that occurs within the octahedral layers of clinochlore (within the *a-b* planes: Figure 3.1), and because they provide a measure of the distance contraction that occurs between single-ions and nearby pairs that is induced by compression. The fit yields a value for $d\ln(I_N/(I_N+I_R))/d\ln((R_o-R_P)/R_o)$, where R_o and R_P are the zero-pressure and high-pressure Cr-Cr distances, respectively, of 0.26 ± 0.03, which is a more delocalized dependence on distance than those that result from simple electrostatic coupling interactions (Figure 3.13).

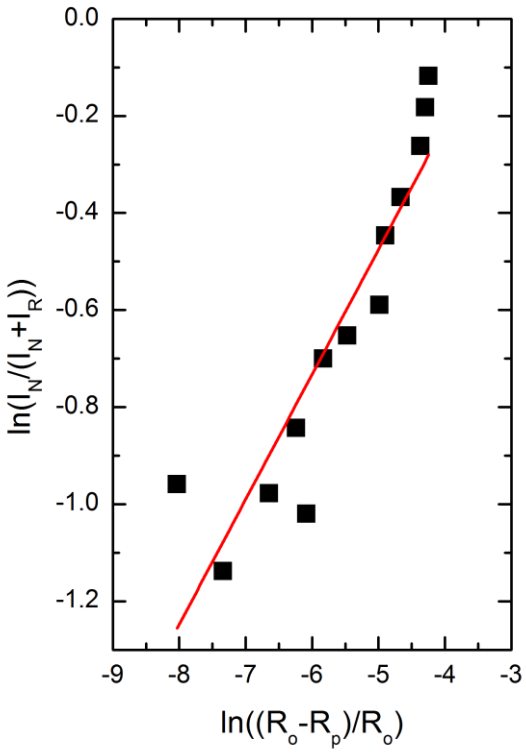

Figure 3.13. Intensity as a function of Cr-Cr distance; R_o is the zero-pressure separation and R_p is the separation at pressure. The slope of the log-log fit is 0.26 ± 0.03. Cr-Cr distances from and interpolated from (Zanazzi et al. 2007), intensity data from this study.

This empirical result indicates that the effect of compaction on excitation transfer between single ions and pair traps in this quasi-2D material is extreme. It is possible that resonant energy transfer, and associated spectral overlap between single-ion emission and pair absorption, may be important in the pressure-dependence of energy transfer in this material, particularly given the progressive decrease in separation between the R_1 line and the primary N-line shown in Figure 3.7. It is also possible that geometrical effects produced by compaction, and in particular the decreased distortion of Cr-bearing octahedra under compression, could also play an

important role in shifting the efficiency of energy transport. Regardless of which effects dominate, the energy transfer between single ions and pairs in this material is dramatically sensitive to small changes in Cr-Cr separations.

3.6 Conclusions

The luminescence spectra of Cr^{3+} in the layered silicate clinochlore have been characterized at high pressure. Three manifolds of neighbor lines produced by ferromagnetically coupled Cr-Cr pairs are observed and assigned: the number of pairs is in accord with that expected for this quasi-2-dimensional system. A transition from R-line (single ion) to N-line (pair) dominated emission is observed under compression. The shift in intensity is progressively enhanced by pressure, and N-line emission totally obscures R-line emission by ~12 GPa. This transition is due to markedly more efficient energy transport from single-ions to pairs, and this increase in efficiency varies as roughly the 4^{th} power of the change in inter-cation distances within the quasi-2-D layer within which the Cr ions reside.

In particular, Cr-pair emission may be enhanced under compression due to cation sites becoming closer to ideal octahedral geometry under compression, with bond angles between neighboring octahedra approaching 90 degrees. Other effects may include energy transfer between single ions and pairs under compression due to resonant transfer between the single ion donors and paired acceptors. The observation of a transition from R-line to N-line emission under pressure further implies that a chromium concentration of ~3000 ppm in clinochlore is close to the critical concentration where single-ion to single-ion non-radiative transfer processes become

efficient (with excitations ultimately encountering the ‘trap’ of pair centers). This concentration is in general accord with the critical concentration for delocalization of single-ion excitation in ruby (e.g., Lyo, 1971). The role of pressure is thus to produce an enhancement of orbital interactions that moves the clinochlore Cr^{3+}-luminescent system from a localized single-ion system to a system dominated by pair-line emissions.

Chapter 4

High-pressure compressional mechanisms of natural topaz [$Al_2SiO_4(F,OH)_2$] up to 60 GPa 4.1 Introduction

Metamorphic minerals transport water and volatiles to depth during subduction. The dehydration of minerals in subduction zones is well-known to cause partial melting and back arc volcanism. The water budget of a subducting slab is complex, but it is generally agreed that the amount of water subducted is substantially greater than the amount of water released above the back arc (Peacock 1990; Poli and Schmidt 1995; Schmidt and Poli 1998; Williams and Hemley 2001). Minerals such as lawsonite [$CaAl_2Si_2O_7(OH)_2 \cdot H_2O$], phengite [$K(AlMg)_2(OH)_2(SiAl)_4O_{10}$], topaz [$Al_2SiO_4(F,OH)_2$], and other dense hydrous phases are thought to be able to transport water and volatiles to depths greater than ~150 km (Wunder et al. 1993; Pawley 1994; Schmidt and Poli 1994; Domanik and Holloway 1996; Ono 1998).

Topaz is a subduction-related mineral that is found in metasediments and has a large pressure and temperature stability field. Topaz can form in pelitic sediments in subduction zones at conditions starting near 5.0 GPa and ~600 °C. Topaz has been shown to be stable to at least 12 GPa and ~1100 °C (Holland et al. 1996). Hydroxyl rich topaz has been found in high-pressure and ultra-high-pressure belts of the Sulu terrane, China (Zhang et al. 2002). In order to fully understand H_2O and fluorine (F) cycling in subduction zones, detailed studies of the minerals that are likely to carry H_2O and F to depth are required. Previous high-pressure, room temperature spectroscopic investigations focused on looking at the pressure dependence of the OH

stretches and silicate vibrations (Bradbury and Williams 2003; Komatsu 2005). Spectra were collected up to ~24 and ~30 GPa, respectively, and no phase transitions were observed. High-pressure room temperature single-crystal X-ray diffraction studies have also been reported up to ~45 GPa and, again, no phase transitions were observed (Komatsu et al. 2003; Gatta et al. 2006, 2014). Moreover, Gatta et al. (2014) report that H-bonding in natural F-rich topaz likely strengthens in response to external pressure, which is in contrast to the high-pressure spectroscopic results reported by Bradbury and Williams (2003) and Komatsu et al. (2005). Hence, there are ambiguities associated with the high-pressure response of natural F-rich topaz to pressure. More recently, using first principles techniques topaz-OH was investigated at high-pressure and two distinct spacegroups were found, orthorhombic *Pbnm* and monoclinic $P2_1/c$ (Mookherjee et al. 2016). Moreover, another first principles study investigated the effect of fluorine content on the elastic behavior of topaz (Ulian and Valdre 2017).

The luminescence spectrum of topaz has primarily been studied at ambient pressure and various temperatures (Gaft et al. 2003; Tarashchan et al. 2006). In topaz, there is one unique Al site (Figure 4.1); however, there are three unique Al environments whose abundances depend on the relative concentration of OH and F (e.g. $[AlO_4(OH)_2]^{7-}$, $[AlO_4(F)_2]^{7-}$, and $[AlO_4OH,F]^{7-}$). When trace amounts of Cr^{3+} are substituted into the lattice, these different environments give rise to three sets of overlapping transitions for each of the R_1 and R_2 peaks. The two split components are produced by the transition from the doubly-split ^2E level to the $^4A_2$ ground state, and

the three components of each of these peaks can be easily deconvolved. Here, we use luminescence spectroscopy of Cr^{3+} to probe the Al site in topaz under high-pressure. Our experiments are oriented towards (1) determining if any phase transitions occur in topaz under compression, (2) measuring the pressure shift of the R-lines, and (3) determining if any changes in the compression mechanism of topaz occurs at high pressures.

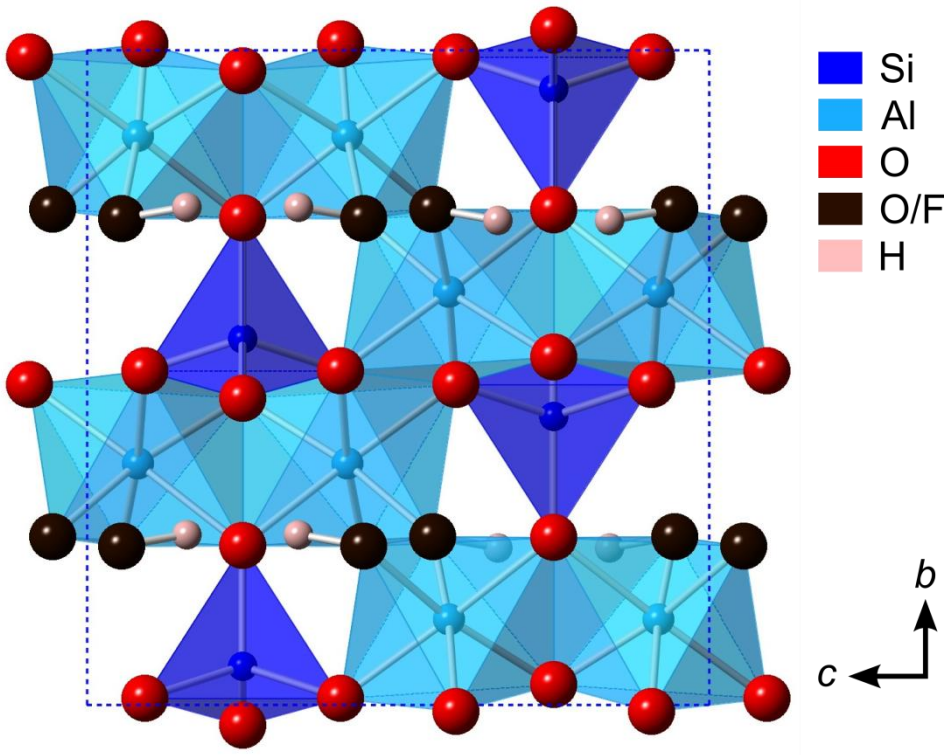

Figure 4.1. Crystal structure of topaz looking along the *a*-axis. Crystal structure based on our own synchrotron X-ray structure refinement. Diagram generated in CrystalMaker ® v 8.7.6.

4.2 Experimental Methods

Our sample was a natural gem quality imperial topaz sample from Capao Topaz mine, Minas Gerais, Brazil. The sample identity was confirmed with Raman

spectroscopy, luminescence spectroscopy, and single-crystal X-ray diffraction, all of which agree well with previous studies (Alston and West 1928; Beny and Piriou 1987; Gaft et al. 2003; Tarashchan et al. 2006). Trace element concentrations of topaz were measured with a PhotonMachines Analyte 193H, which is a 193-nm ArF excimer laser system coupled with a ThermoScientific ElementXR single-collect or magnetic sector ICP-MS. The instrument was calibrated with a SRM 610 trace element glass from NIST, and Al was used as the internal standard. The following trace elements were measured, Cr 145 ±68, V 35 ±14, Fe 68 ±43, Mn 2.0 ±0.4, and Ti is below detection limits (all numbers in ppm). From single-crystal diffraction experiments, we calculate a site occupancy for F of 0.743 (±0.026), with the balance being hydroxyl ions.

High static pressures were generated using a symmetric type diamond anvil cell (DAC). Anvils were 16 sided type Ia diamonds with culet sizes that ranged from 500 to 200 μm depending on target pressure, and gaskets were made from rhenium. The pressure medium was either 16:3:1, Ne, or He depending on target pressures. Ne and He gasses were loaded with a high pressure gas loading apparatus at the Advanced Light Source, Berkeley, CA. A single crystal of the sample along with at least two ruby spheres (Chervin et al. 2001) were loaded into the sample compartment. Pressures were determined using the standard ruby fluorescence pressure gauge (Mao et al., 1986), and data were collected on both compression and decompression.

Luminescence spectra were collected from 650-800 nm (15380-12500 cm^{-1}) with a Horiba LabRAM HR Evolution Raman spectrometer with a spectrometer focal length of 800 mm. Spectra were collected to a pressure of ~60 GPa and on decompression at 300 K using an excitation wavelength of 532 nm. An Olympus BXFM-ILHS microscope with a 50x long working distance objective was used to focus the laser beam onto the sample. An 1800 lines/mm grating with a corresponding spectral resolution of ~1 cm^{-1} (or, equivalently, ~0.05 nm) was utilized. Combinations of Gaussian and Lorentzian functions were fit to the luminescence spectra with Horiba Labspec6 software.

4.3 Results and discussion

4.3.1 Emission band assignments

The luminescence spectra of topaz at various temperatures are shown in Figure 4.2. These spectra agree well with the previous studies of Gaft et al. (2003) and Tarashchan et al. (2006). At room temperature and pressure, the sharp R-line emissions, a broad $^4T_2$-$^4A_2$ transition, and vibrational sidebands are observed. At 77 K, the sharp R-lines shft to slightly shorter wavelength, and the $^4T_2$-$^4A_2$ transition become unresolvable. This assignment and observation agree well with the ambient pressure spectra and the interpretation of Tarashchan et al. (2006). The three components of each R-line are easily observed at 77K, as well as a more complex set of lines associated with emission from neighboring Cr^{3+}-ions (N-lines).

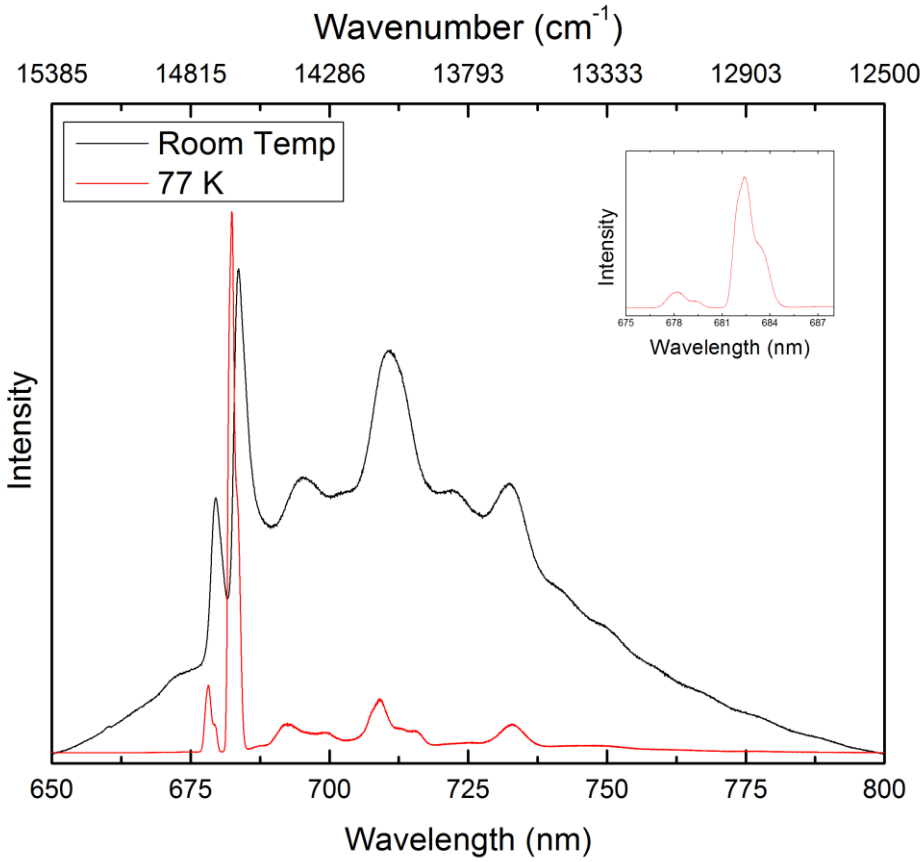

Figure 4.2. Cr^{3+} luminescence emission spectra of topaz at various temperatures. Inset shows a detailed view of the R-lines at 77 K showing the multi-component character of each R-line.

Figure 4.3 shows a representative deconvolution of the R-lines at room pressure and temperature. Three emission bands can be fit under each R-line. Given that the OH/F ratio in this topaz is ~0.35, the majority of the Al sites in this topaz have the $[AlO_4(F)_2]^{7-}$ environment, with the mixed site ($[AlO_4OH,F]^{7-}$) being the next most abundant, and the $[AlO_4(OH)_2]^{7-}$ environment being the least abundant. Hence, we assign the intense 683.5 nm R_1 band to the $[AlO_4(F)_2]^{7-}$ site, the 684.7 nm R_1 band to the $[AlO_4OH,F]^{7-}$ site, and the 683.1 nm R1 band to the $[AlO_4(OH)_2]^{7-}$ site.

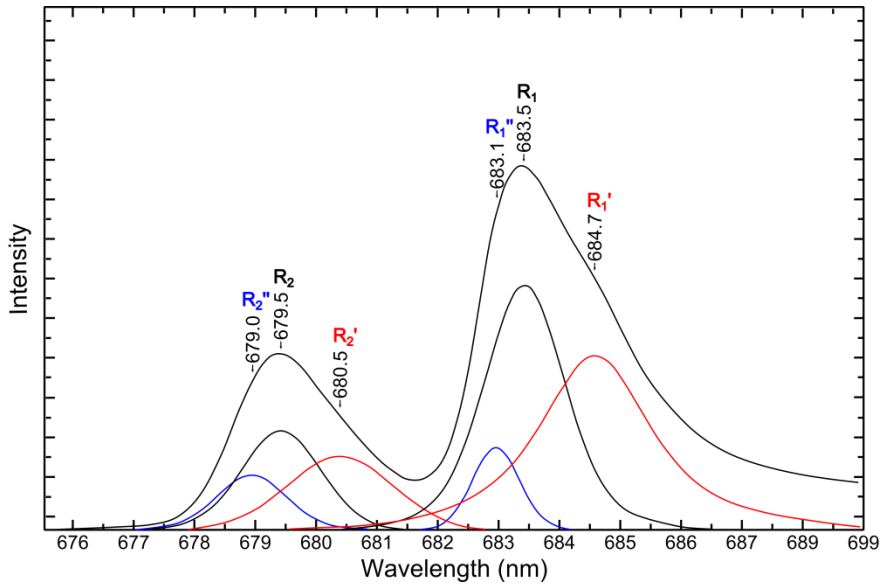

Figure 4.3. Deconvolution of the R-lines in topaz showing the three components of each R-line, at room pressure and temperature.

4.3.2 High-pressure spectra

Representative high-pressure luminescence spectra of the topaz R-lines up to ~55.0 GPa are shown in Figure 4.4. As with all Cr^{3+} R-line emissions observed to date (Dolan et al. 1986; Mao et al. 1986; Wamsley and Bray 1994; O'Bannon and Williams 2016a, 2016b, 2017), the R-lines shift to longer wavelength under compression to ~55.0 GPa. The intensity of the R-lines decreases as a function of pressure, and they become unresolvable above ~55 GPa (they continued to be unresolvable to at least 60 GPa). On decompression from 60 GPa the R-lines again became resolvable near 55 GPa, and no hysteresis of the luminescence peaks was observed. The loss of intensity above 55 GPa is probably due to pressure-induced migration of the absorption bands in topaz to wavelengths such that pumping these transitions with 532 nm excitation becomes inefficient. The observed broadening of

the topaz R-lines is due to non-hydrostatic conditions, and is observed in both experiments with Ne and He as pressure media.

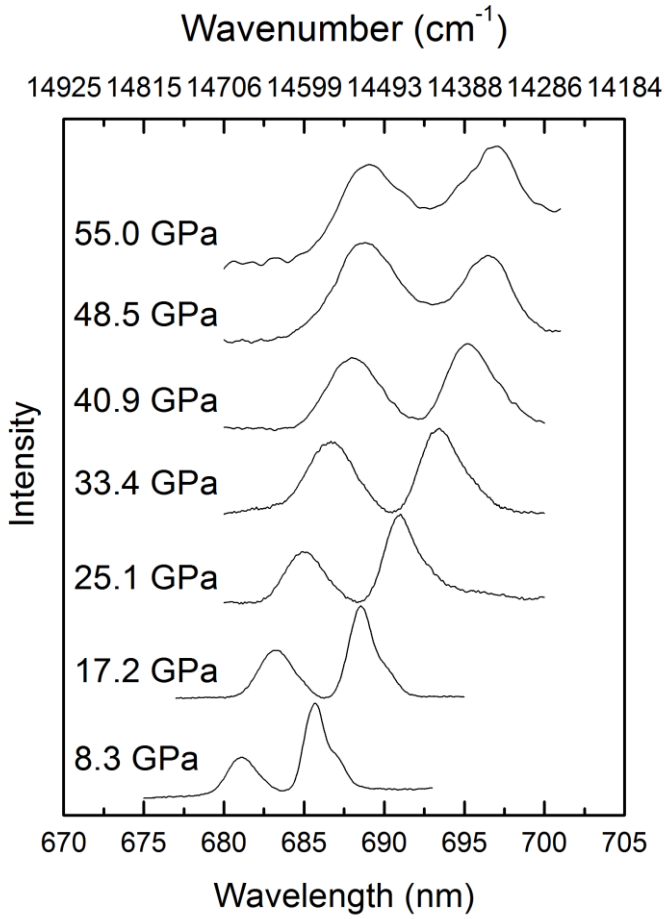

Figure 4.4. Representative high-pressure luminescence spectra of topaz up to ~55.0 GPa. Spectra were collected in a Ne pressure medium.

The pressure shifts of the R-lines of topaz are plotted in Figure 4.5, and they are tabulated in Table 4.1. The R-lines are labeled in accord with their intensity. The most intense components (associated with a fully fluorinated environment) are R_1 and R_2, the intermediate intensity components are R_1' and R_2' (the mixed F/OH environment), and the least intense components are labeled R_1" and R_2" (the solely

OH-bearing octahedra). The pressure shift of the R-lines is remarkably linear below ~40 GPa suggesting that the compaction mechanism of topaz, as manifested at the Al site, remains constant up to ~40 GPa. Above 40 GPa the pressure shift becomes non-linear suggesting that the compressional mechanism changes above this pressure. This shift in compressional mechanism is not in accord with the constant compressional mechanism reported based on single crystal results by Gatta et al. (2014). They report that neither phase transitions, changes in compressional mechanism, nor changes in Al-site distortion are observed under compression to ~45 GPa. However, a plot of the pressure dependence of the Al-site volume from their study shows that the site volume remains essentially constant above ~40 GPa (Figure 4.6a). The Si site volumes and bond lengths reported by Gatta et al. (2014) do not show any trends and are a bit more scattered than the Al site (Figure 4.7). The Al-O/F bond lengths as a function of pressure show similar behavior, with the Al-O bond lengths becoming nearly constant at about ~40 GPa; the Al-F bond lengths may show similar behavior, but they are sufficiently scattered that it is difficult to conclusively resolve a trend. These previous single-crystal data, combined with our luminescence results, strongly indicate that a change in the compressional mechanism of topaz occurs above ~40 GPa. Notably, the experiment was conducted using both He and Ne pressure media (Figure 4.5) in order to rule out the possibility that non-hydrostaticity in Ne at pressures above 40 GPa might be the cause of the non-linear pressure shift. The non-linear behavior is identical in both He and Ne pressure media, and on decompression the band positions are completely reversible.

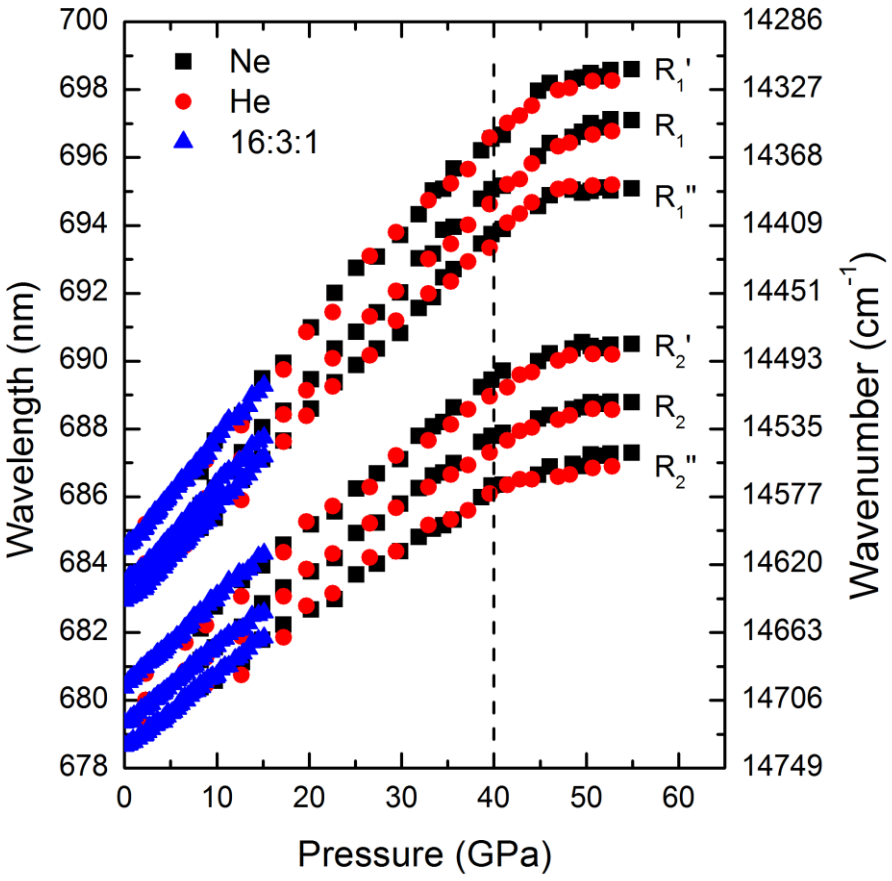

Figure 4.5. Pressure shift of the R-lines in topaz, triangles are in a 16:3:1 alcohol mix, circles are in He, and squares are in Ne. Error bars are smaller than the symbols.

Assignment	Pressure shift (nm/GPa)	R^2 value
Ne experiment (up to 40 GPa)		
R_1"	0.27 ±0.10	0.997
R_1	0.29 ±0.10	0.997
R_1'	0.30 ±0.16	0.993
R_2"	0.18 ±0.08	0.998
R_2	0.20 ±0.06	0.999
R_2'	0.22 ±0.08	0.998
He experiment (up to 40 GPa)		
R_1"	0.27 ±0.11	0.998
R_1	0.28 ±0.07	0.999
R_1'	0.31 ±0.14	0.998
R_2"	0.19 ±0.14	0.994

R_2	0.20 ±0.10	0.997
R_2'	0.22 ±0.13	0.996
16:3:1 experiment (up to 15 GPa)		
R_1"	0.29 ±0.01	0.998
R_1	0.29 ±0.01	0.998
R_1'	0.32 ±0.01	0.998
R_2"	0.22 ±0.01	0.998
R_2	0.22 ±0.01	0.998
R_2'	0.26 ±0.01	0.998

Table 4.1. Pressure shift of each component of the R-lines for all three experiments. Notably, the pressure shifts between the Ne and He experiments are essentially identical. The larger errors from the He and Ne experiments are produced by the uncertainty in deconvolving all three components of the peaks in weaker, broader bands at higher pressures.

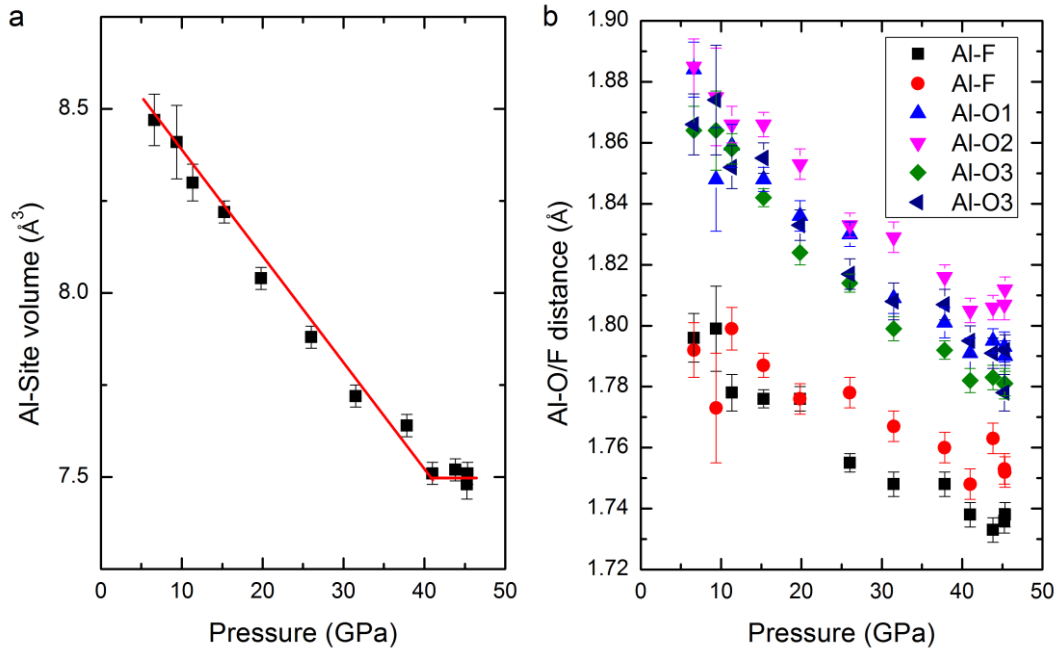

Figure 4.6. Single crystal data on topaz from Gatta et al. (2014). Note both the (a) Al-site volume behavior above ~40 GPa and the (b) Al-O bond length behavior above ~40 GPa.

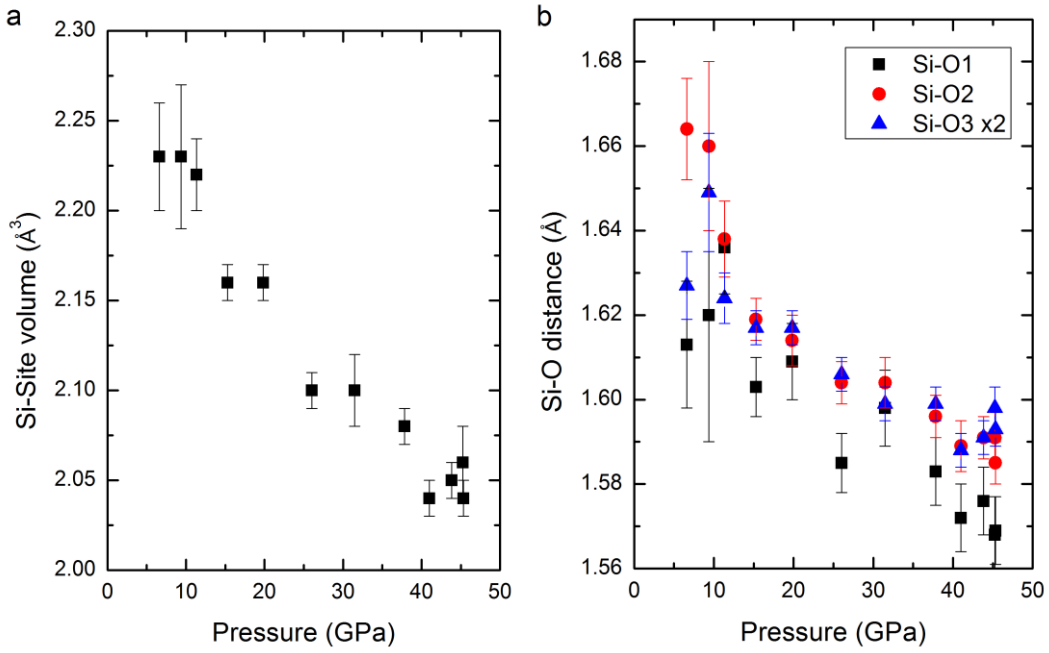

Figure 4.7. Single crystal data on topaz from Gatta et al. (2014). (a) Si-site volume and the (b) Si-O bond length.

4.3.3 R-line separation and FWHM

The separation between the R_1 and R_2 bands of all three components of the R-lines increases as a function of pressure. Figure 4.8 shows the separation of the three components of the R-lines. All three components behave in a similar way and their separation increases as pressure increases; again, this behavior is fully reversible on decompression. As this separation arises from the distortion of the Al/Cr-octahedron from an ideal geometry (e.g., Syassen, 2008), this increase in separation implies that the Al-sites become more distorted under compression. The observed decrease in the R-line separation of the R_1" and R_2" components above 40 GPa may be due to the difficulties in fitting the weak R_1" component because of peak broadening and low intensity of the emission bands at the highest pressure of these experiments. There is

also a change in slope above ~40 GPa in R_1-R_2 and R_1'-R_2' (Figure 4.6b and 4.6c) which is consistent with a change in deformation mechanism, as indicated by both the R-line pressure dependences and single crystal diffraction data (Figures 4.5 and 4.6). It is possible that the deviation from the lower pressure trend of the R-line separation above 40 GPa is largest for the doubly hydroxylated site, intermediate in magnitude for the singly hydroxylated site, and smallest for the fully fluorinated site (Figure 4.8).

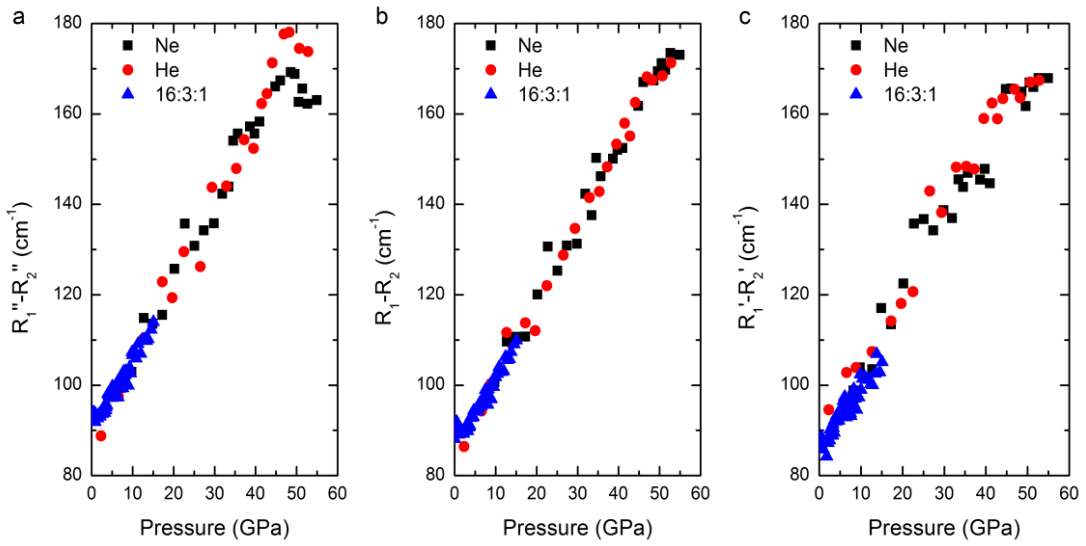

Figure 4.8. R-line separation as a function of pressure (a) R_1"-R_2" hydroxylated site (b) R_1-R_2 fluorinated site and (c) R_1'-R_2' F,OH site. Error bars are smaller than the symbols, and different pressure media are shown with the same symbols and colors as Figure 4.5.

Full width at half maximum (FWHM) of the topaz R-lines as a function of pressure are shown in Figure 4.9. The peak width of the R-lines increases as pressure increases. Notably, at the highest pressures, the peakwidth with a He medium is narrower than the peakwidth in Ne, which shows that, unsurprisingly, the He

experiment is more hydrostatic than the Ne experiment. This agrees well with previously reported results on differential stress in different pressure media (Klotz et al. 2009). As with the shift in R_1-R_2 separation, the uniform increase in peakwidth as a function of pressure suggests that the Al-sites become more distorted as a function of pressure.

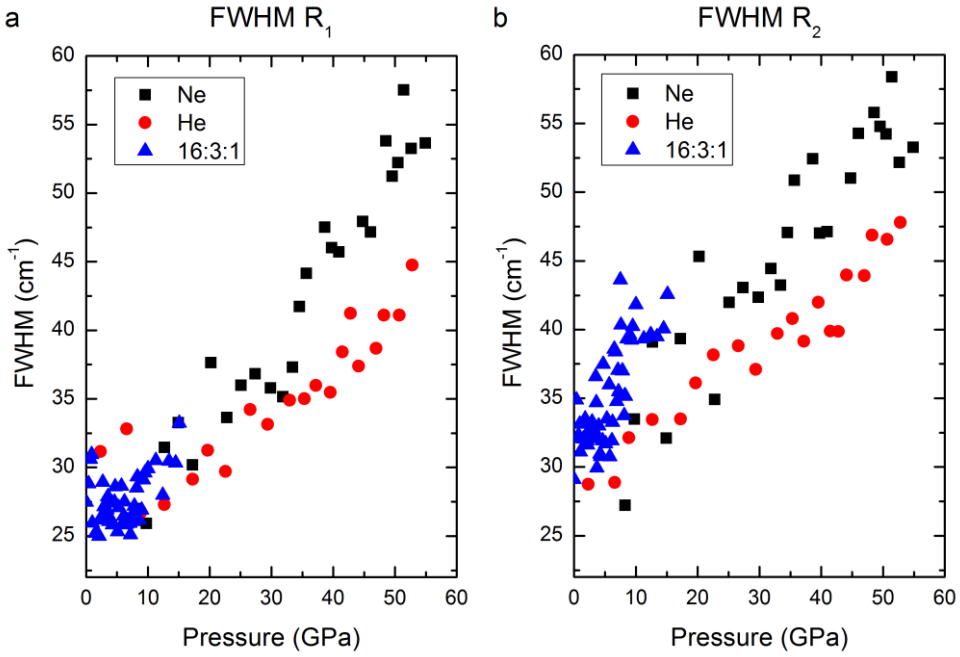

Figure 4.9. Full width at half maximum of (a) R_1 and (b) R_2. The other components of the R-lines show similar trends but are not plotted for clarity.

It should be noted that Gatta et al. (2014) modeled the Al sites as fully fluorinated. This is not totally accurate considering the reported composition of their sample [$Al_{2.00}Si_{1.05}O_{4.00}(OH_{0.26}F_{1.75})$]. It is not surprising that their structural model would not fully of capture subtle differences in the compression behavior of the three unique Al environments since their structures represent an average change of the Al-

F/OH bond length. Cr^{3+} luminescence allows us to probe all three Al environments under compression and it demonstrates the sensitivity of this technique. The pressure shift, R-line separation, and FWHM of the Cr^{3+} luminescence bands all behave slightly differently from one another indicating that each Al environment responds differently to compression. Gatta et al. (2014) report that compression is mainly accommodated by contraction of the polyhedral bond distance, along with polyhedral tilting. If we recall Figure 4.6b, Gatta et al. (2014) report two populations of bonds in the Al-site, with the Al-O bonds being more compressible than the Al-F bonds. Moreover, the pressure dependence of the Al-O and Al-F bond lengths reported by Gatta et al. (2014) changes above ~40 GPa. Interestingly, this change in bond length behavior as a function of pressure was not discussed by these authors. This change in behavior may be explained by H···H repulsion and/or changes in the H-bonding environment of the hydroxyls. Ulian and Valdre (2017) report that using density functional theory that each topaz model that contains an OH group changes in H-bonding are established under compression. Moreover, our luminescence data suggest that the hydroxylated and the mixed F/OH sites show the largest changes above ~40 GPa (Figure 4.8a and 4.8c). Hence, a transition to a compression mechanism where polyhedral tilting becomes the dominate mechanism with polyhedral bond contraction playing a more minor role likely occurs above ~40 GPa, and is likely driven by changes in H-bonding.

4.4 Implications

Our results indicate that the compression mechanism in topaz changes above ~40 GPa; this shift is supported by the single crystal data of Gatta et al. (2014), although the change was not recognized in their study. The R-line splittings and FWHM of the luminescence bands both are consistent with the Al-sites in topaz becoming more distorted under compression up to 40 GPa. Our results also show that the high-pressure behavior of the different Al environments (e.g. $[AlO_4(OH)_2]^{7-}$, $[AlO_4(F)_2]^{7-}$, and $[AlO_4OH,F]^{7-}$) are similar to one another up to 40 GPa. This suggests that no single Al environment is notably less stable than the others. The behavior of the luminescent bands above 40 GPa indicate that the Al-polyhedra become less compressible above this pressure, and that polyhedral tilting and/or tetrahedral distortion may play more major roles in the compaction of topaz above this pressure than polyhedral bond contraction does. This is likely driven by changes in the H-bonding environment of the Al-sites that are fully hydroxylated and the mixed OH/F Al sites.

Thus, this change in slope of the R-lines above ~40 GPa, and associated shift in compressional mechanism, could be precursory behavior to a phase transition. The observation that the luminescence spectra are fully reversible following compression to 60 GPa implies that any transition is either fully reversible, or occurs above 60 GPa at 300 K. A notable aspect is that topaz is, at 300 K, it is one of the most metastable tetrahedrally-coordinated silicates under compression known: for comparison magnesian olivine persists to 54 GPa prior to amorphizing (Santamaria-Perez et al. 2016). This stability is plausibly a consequence of (as with olivine) its tetrahedra

being surrounded by stable, highly coordinated cations in a relatively simple arrangement (Fig. 4.1) in which compression is dominantly achieved (initially) by simple polyhedral compaction. Diopside [$CaMgSi_2O_6$] is another example of a mineral that persists metastably at 300 K to very high pressures (Chopelas and Serghiou 2002; Plonka et al. 2012). Diopside undergoes a phase transition near 55 GPa where half of the Si-sites change coordination from SiO_4 to SiO_6 (Chopelas and Serghiou 2002; Plonka et al. 2012). Unlike topaz and olivine, diopside is a chain silicate and the topology of the structure allows for coordination changes to occur in the Si sites at high-pressure.

If topaz does undergo a phase transition at a pressure above ~60 GPa, this pressure corresponds to a depth of >1400 km in the Earth. Even in cold subduction zones, topaz would probably be close to being in thermal equilibrium with the surrounding mantle at these depths (as it should predominantly form near the top of the slab, in pelitic sediments). Thus, no low temperature transition in topaz is likely to occur within Earth's interior, and the major transformations undergone by topaz are likely to be either dehydration or conversion to high pressure hydrous aluminous phases (Ono, 1999; Sano et al., 2008). Nevertheless, the high degree of metastability exhibited by topaz at 300 K indicates that it could be a strong candidate to kinetically persist substantially beyond its stability field if present in lower temperature subduction zone environments.

Chapter 5

High-pressure phase transitions in tourmaline a single-crystal and luminescence study

5.1 Introduction

Tourmaline is a supergroup of minerals that are chemically complex and are divided into different varieties based on chemical composition (Hawthorne and Henry 1999; Henry et al. 2011). This group of minerals is so complex that an entire subcommittee on tourmaline nomenclature exists. These minerals are categorized using the generalized tourmaline structural formula $XY_3Z_6(T_6O_{18})(BO_3)_3V_3W$ where X = Na, Ca, K; Y = Fe, Mg, Mn, Al, Li; Z = Al, Fe, Mg, Cr; T = Si, Al; B= B; V = (OH), O; and W = (OH), O, F (Hawthorne and Henry 1999; Henry et al. 2011). From a compositional perspective, most of the variability occurs in the X, Y, and Z sites, and we refer readers to Hawthorne and Henry (1999) and Henry et al. (2011) for more information on the classification of tourmaline supergroup minerals. Tourmaline is also highly sought after as a gemstone due to its high hardness and wide range of colors.

Tourmaline typically crystallizes in the rhombohedral crystal system with *R3m* symmetry (Hawthorne and Henry 1999; Henry et al. 2011), although other crystal systems have been reported (Akizuri et al. 2001; Shtukenberg et al. 2007). It is typically considered a ring-silicate with six corner shared TO_4 tetrahedral sites that form a hexagonal ring, a nine-fold X-site, two six-fold octahedral Y- and Z-sites, and a

trigonal planar B-site (Figure 5.1), although B and Li substitution into the tetrahedral sites has been reported (Rosenberg and Foit 1979; Hughes et al. 2000). Interestingly, the first reported structure of tourmaline presented the Si_6O_{18} ring as ditrigonal in symmetry (Hamburger and Buerger 1948). However, it was later shown to be hexagonal in symmetry (Ito and Sadanaga 1951), and all subsequent studies agree that the Si_6O_{18} ring is hexagonal.

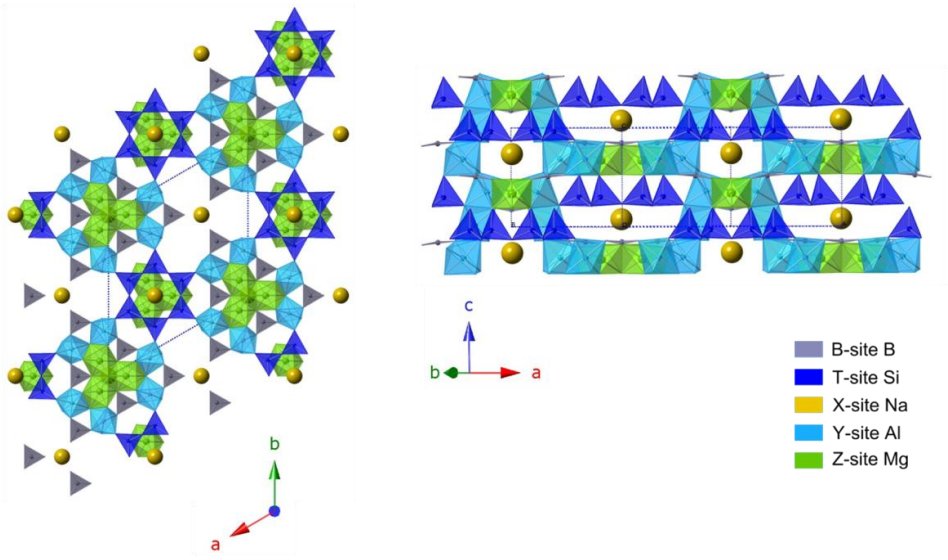

Figure 5.1. Crystal structure diagram of dravite tourmaline. Unit cell shown as dashed line, and diagrams were generated in CrystalMaker ® v8.7.6.

Tourmaline is the most widespread borosilicate mineral in natural rocks and can be found in subduction zone environments (Nakano and Nakamura 2001; Bebout and Nakamura 2003; Ota et al. 2008). Petrologic studies have shown that dravite tourmaline breaks down at ~7.0 GPa and ~900 °C (Werding and Schreyer 1996) and ~3-5 GPa and ~1000 °C (Krosse 1995) and that breakdown pressures and temperatures are dependent on its precise composition (Ota et al. 2008). The

decomposition products associated with tourmaline breakdown are complex, but one decomposition product, phengite, is important from a deep Earth boron and water cycling perspective; phengite could transport B to depths >300 km (Domanik and Holloway 1996; Marschall et al. 2007). Higher pressure studies (e.g. > 7.0 GPa) on tourmaline are scarce, and to the best of our knowledge only two studies have been reported (Li et al. 2004; Xu et al. 2016). Li et al. (2004) conducted high-pressure powder diffraction experiments on schorl variety tourmaline which has an ideal formula of $[Na(Fe_3)Al_6(Si_6O_{18})(BO_3)_3(OH)_3(OH)]$ up to 27.8 GPa, and phase transitions were not reported. Xu et al. (2016) reported high-pressure and temperature powder diffraction experiments on uvite variety tourmaline which has an ideal formula of $[Ca(Mg_3)MgAl_5(Si_6O_{18})(BO_3)_3(OH)_3(OH)]$ up to ~18.4 GPa and 723 K and again, no phase transitions were observed.

This is in contrast to other ring-silicates such as cordierite $[(Mg, Fe)_2Al_3(AlSi_5O_{18})]$ and beryl $[Be_3Al_2(Si_6O_{18})]$ which each show extensive high-pressure polymorphism (Prencipe et al. 2011; Miletich et al. 2014; Scheidl et al. 2014; Finkelstein et al. 2015; O'Bannon and Williams 2016b). Both cordierite and beryl undergo high-pressure phase transitions that involve distortion of the Si_6O_{18} ring. The main structural difference between tourmaline and these other ring silicates is that tourmaline does not have open channels in its structure like cordierite and beryl. It is possible that the configuration of the Si_6O_{18} rings in tourmaline creates a

structure that is more stable under compression than open channel ring silicates like cordierite or beryl.

Tourmaline is also both pyroelectric and piezoelectric, and has been used in industrial applications such as pressure gauges (Frondel 1948). Growing synthetic tourmaline >1mm in diameter has not yet been achieved, and any industrial applications require natural tourmalines (Shekhar Pandey and Schreuer 2012). The two previous studies of Li et al. (2004) and Xu et al. (2016) provide insights into how the unit cell responds to compression. However, they do not elucidate the positional changes of the individual atoms in the unit cell. Hence, our experiments are oriented towards (1) understanding the trace element response of dravite tourmaline to compression using high-pressure luminescence spectroscopy which is a sensitive site-specific probe of bonding environments, (2) understanding the bulk crystallographic response of dravite tourmaline to compression using synchrotron based high-pressure single-crystal diffraction, and (3) integrating the responses of these two types of studies to provide an integrated picture of structural changes in this material under compression.

5.2 Methods

5.2.1 Sample characterization

The natural sample used in this study is from the Lengenbach Quarry, Switzerland. The sample is a light green dravite variety tourmaline [$Na(Mg_3)Al_6(Si_6O_{18})(BO_3)_3(OH)_3(OH)$]. We characterized the sample with single-

crystal X-ray diffraction, Raman, and luminescence spectroscopy, which all agree well with previous studies (Hawthorne et al. 1993; Gasharova et al. 1997; Gaft et al. 2005). Ambient pressure single-crystal X-ray measurements were conducted on Beamline 11.3.1 at the Advanced Light Source (ALS) at Lawrence Berkeley National Lab in Berkeley, CA. We modeled our tourmaline as an endmember dravite and our ambient structure refines with an R_1 of 1.9%. Its crystal system, spacegroup and unit cell parameters are: rhombohedral *R3m*, *a*-axis 15.9670(6) Å, *c*-axis 7.1749(3) Å, and volume 1578.2(2) $Å^3$, respectively. Trace element concentrations of dravite tourmaline were measured with a PhotonMachines Analyte 193H, which is a 193-nm ArF excimer laser system coupled with a ThermoScientific ElementXR single-collect or magnetic sector ICP-MS. The instrument was calibrated with a SRM 610 trace element glass from NIST, and Al was used as the internal standard. The following trace elements were measured: Cr 215 ±19, V 336 ±32, Li 18 ±4.0, Ti 474 ±53, Ca 2183 ±597, and K, Fe, and Mn are below detection limits (all numbers in ppm). Hence, our single-crystal X-ray results combined with our trace element analysis indicate that our sample is nearly an endmember composition dravite tourmaline, and all high-pressure structures can thus be modeled as endmember dravite.

5.2.2 Luminescence spectroscopy

Luminescence spectra were collected from 650-800 nm (15380-12500 cm^{-1}) with a Horiba LabRAM HR Evolution Raman spectrometer with a spectrometer focal length of 800 mm. Spectra were collected to a pressure of ~65 GPa and on

decompression at 300 K using an excitation wavelength of 532 nm. A symmetric type DAC with 200 µm type-Ia diamonds was used in all high-pressure luminescence experiments, and single crystals of the sample and at least two ruby spheres (Chervin et al. 2001) were loaded into the sample compartment. Either 4:1 methanol:ethanol mixtures or Ne was used as the pressure medium depending on the target pressure range of the experiment. An Olympus BXFM-ILHS microscope with a 50x long working distance objective was used to focus the laser beam onto the sample. An 1800 lines/mm grating with a corresponding spectral resolution of ~1 cm^{-1} (or, equivalently, ~0.05 nm) was utilized. Combinations of Gaussian and Lorentzian functions were fit to the luminescence spectra with Horiba Labspec6 software.

5.2.3 High-pressure single crystal diffraction

High-pressure single-crystal measurements were carried out using a (DESY) BX90 (Kantor et al. 2012) type diamond anvil cell (DAC) equipped with type Ia 500 µm culet Boehler-Almax (Boehler and De Hantsetters 2004) geometry diamond anvils with 85^{o} angular access. Rhenium gaskets with a 250 µm hole were used to contain the samples. Gasket holes were cut using an Oxford Instruments laser mill at the Advanced Light Source, Berkeley, CA. Single crystals of dravite tourmaline and two ruby spheres were loaded into the sample compartment with neon as the pressure medium. The standard ruby fluorescence gauge was used to determine pressure (Mao et al. 1986). Neon was loaded using the gas loading apparatus at the

Advanced Light Source. Neon remains hydrostatic up to ~15.0 GPa, and above that pressure the pressure gradients remain small (Klotz et al. 2009).

High-pressure single-crystal X-ray diffraction measurements were conducted at Beamline 12.2.2 at the ALS. Measurements were taken at various pressures up to ~22.6 GPa at room temperature. The DAC was mounted on a Huber sample stage, and shutterless single-crystal diffraction data were collected on a Perkin Elmer amorphous silicon detector using synchrotron radiation monochromated by silicon(111) to a wavelength of 0.49594 Å (25 keV). Distance and wavelength calibrations were done using a NIST single crystal ruby diffraction standard. Phi scans were employed to measure across both diamonds with a 0.25° image width.

5.2.4 Data processing

Image masks, to avoid integrating signal from detector regions obscured by the DAC, were created using the program ECLIPSE (Parsons 2010). The data were integrated using the program SAINT v8.34A. A multi-scan correction for absorption was applied using the program SADABS-2014/11. Structures were solved by dual space methods (SHELXS-97/ SHELXT) and refined by full-matrix least-squares on F^2 (SHELXL-2014) (Sheldrick 2008) using the graphical user interface *ShelXle* (Hübschle et al. 2011). All atoms in the room pressure structure were refined anisotropically, and the atoms in the high-pressure structures were refined isotropically. Complete crystallographic information files (CIFs) for each structure can be found in supplementary material, as well as a discussion on the selection of

our unit cells.

5.3 Results and discussion

5.3.1 Ambient pressure luminescence spectra

The luminescence spectrum of dravite is characteristic of d^3 configuration ions (e.g. Cr^{3+}, V^{2+}) in an intermediate strength crystal field (Tanabe and Sugano 1954) and both sharp and broad emission bands are observed at room temperature and 77 K (Figure 5.2). Considering the similar concentrations of Cr and V in our sample (e.g. Cr: 215 ±19 ppm, V: 336 ±32 ppm), it is reasonable to assume that our steady state luminescence spectra contain overlapping bands from the emission of both Cr and V. This is commonly observed in emerald, which is the Cr and V rich variety of beryl (Ollier et al. 2015; O'Bannon and Williams 2016b). The intense and relatively sharp emission bands are commonly referred to as the R-lines and are associated with the spin-forbidden ^2E-$^4A_2$ transition, with the $^4A_2$ state being the ground state and the ^2E state being split in non-cubic environments (Syassen 2008), and the broad band emission is assigned to the spin-allowed $^4T_2$-$^4A_2$ transition (Sugano and Tanabe 1958; Burns 1993; Gaft et al. 2005).

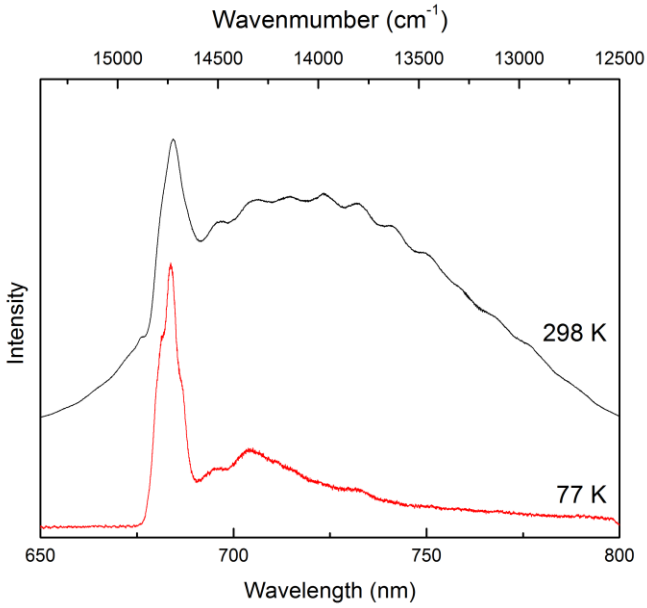

Figure 5.2. Steady state luminescence spectra of dravite tourmaline at 300 and 77 K using 532nm excitation. Note that the thermally populated $^4T_2$ bands are not entirely quenched at 77K. The modulation in the broad band emission band at 300 K is an artifact.

At 300 K, three bands can be fit under the sharp emission bands and two can be fit under the broad portion of the spectrum at room temperature (Figure 5.3a). At 77 K, the broad thermally populated $^4T_2$ –associated bands are not entirely quenched (Figure 5.3b) and four bands can be fit under the ^2E sharp emission bands. Dravite has two crystallographically unique octahedral sites, Al and Mg, and emission bands from both sites would likely be observed in steady state luminescence spectra. The simplest way for Cr^{3+} and V^{2+} to substitute into dravite is through an isovalent substitution (e.g. Cr^{3+} into Al^{3+} site and V^{2+} into Mg^{2+}). The four deconvolved components in Figure 5.3b can be attributed to two sets of R-lines, one from Cr^{3+} and one from V^{2+}. The Al site in dravite is less distorted than the Mg site

(Hawthorne et al. 1993, and this study), which would be expected to give rise to a narrower R-line splitting. Taking into account the likely relative intensities of R_1 and R_2, the following assignments are proposed: the Cr^{3+} R_1 band is likely located at 683.7 nm, with its R_2 band at 681.4 nm, and the V^{2+} R_1 band is at 686.4 nm and its associated R_2 band at 679.8 nm. This results in an R-line splitting of ~50 cm^{-1} for Cr^{3+} and ~143 cm^{-1} for V^{2+}. For comparison, ruby [Al_2O_3:Cr] has an Al-site that is close to an ideal octahedron with a slight trigonal distortion, and has an R-line splitting of ~29 cm^{-1} (Syassen 2008), while zoisite [$Ca_2Al_3Si_3O_{12}(OH)$] which has a highly distorted Al-site has an R-line splitting of ~340 cm^{-1} (Koziarska et al. 1994). The distortion of the Al and Mg sites in dravite falls intermediate between the distortions of the Al sites in ruby and zoisite, so these R-line splittings seem plausible. In order to unambiguously assign these emission bands, luminescence lifetime measurements would likely be required.

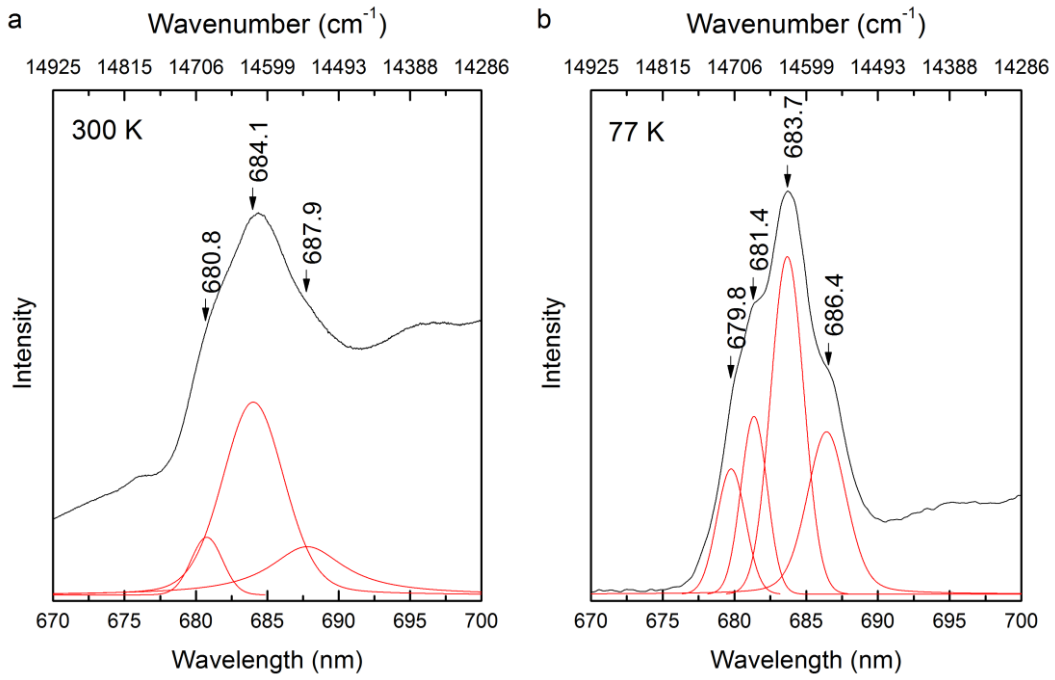

Figure 5.3. Fits to the ^2E -> $^4A_2$ region of the luminescence spectra of dravite (a) 300 K and (b) 77 K.

5.3.2 High-pressure luminescence spectra

High-pressure luminescence spectra are shown in Figure 5.4. Under compression the intensity of the R-lines decreases: this is likely primarily associated with the transition metal absorption bands migrating away from our excitation wavelength of 532 nm. Moreover, the disappearance of the broad $^4T_2$-associated band shows that a transition from an intermediate to strong crystal field occurs in the first few GPa of compression, which is consistent with previous observation in other Cr-bearing oxides (Dolan et al. 1986; de Viry et al. 1987; Hommerich and Bray 1995; Grinberg and Suchocki 2007; O'Bannon and Williams 2016a, 2016b). As with at 300 K, it is difficult to fit four bands under the ^2E region under compression, so we fit

our spectra with three bands: based on our 77 K assignments, these are associated with the R_1 and R_2 peaks of Cr^{3+} and the R1 peak of V^{2+}. Near 6.0 GPa, the primary peak that was fit by three bands now is clearly separated into individual peaks that can be easily seen by the eye (Figure 5.4).

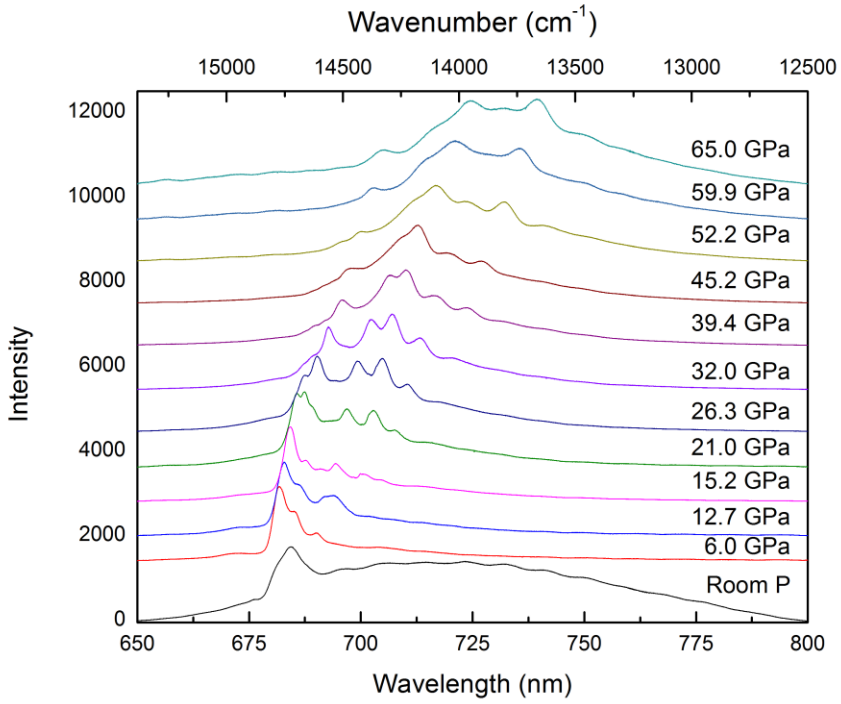

Figure 5.4. High-pressure luminescence spectra of dravite tourmaline up to 65 GPa in a Ne pressure medium. Note the transition from intermediate to strong crystal field between room pressure and ~6.0 GPa.

The pressure shift of two of the original three bands that were fit at room pressure and temperature shift negligibly--essentially by 0 nm/GPa [I would give these in cm-1/GPa as well] up to ~9 GPa, while the other band shifts positively by 0.50 ±0.02 nm/GPa up to the same pressure (Figure 5.5a). The observation of effectively stationary emission bands under compression is without precedent

among Cr^{3+} emission in oxides (e.g., Dolan et al. 1986; Mao et al. 1986; de Viry et al. 1987; Hommerich and Bray 1995; Grinberg and Suchocki 2007; O'Bannon and Williams 2016a, 2016b). Above ~9.0 GPa all observed bands shift positively in wavelength, towards lower energies (Figure 5.5b). It is likely that the two bands that shift by 0 nm/GPa belong to one octahedral site while the other band is associated with the other octahedral site. This is in accord with our assignment of the former two bands to emission from Cr^{3+} substituting into the Al^{3+} site. Four separate experiments were conducted in the ≤ 10.5 GPa range to assess the reproducibility of this unusual observation. It is completely reproducible, and no hysteresis is observed on decompression from ~10.5 GPa. The ~0 nm/GPa pressure shift suggests that the crystallographic site this band is emitting from is not changing volume under compression, or that there is a complex trade-off between electron density and volumetric change within the site. In a complex structure such as dravite tourmaline, it is possible that one octahedral site is rotating or tilting in such a way that the net volume change of the site is small, and that above ~9.0 GPa, this compression mechanism changes. The splitting between these two bands also does not change on compression, suggesting that the site distortion is unchanged, as well. The change in slope at 9 GPa is likely not an indicator of a phase transition, but may represent a change in the compression mechanism. Moreover, the other observed emission band shifts positively in wavelength, consistent with the volume of this site decreasing with increasing pressure. Since we cannot deconvolve the other

component of this band in this pressure range it is difficult to know if this site becomes more or less distorted. However, the peakwidth of the positively shifting band slightly narrows under compression to ~9.0 GPa, which suggests that its site becomes less distorted under compression.

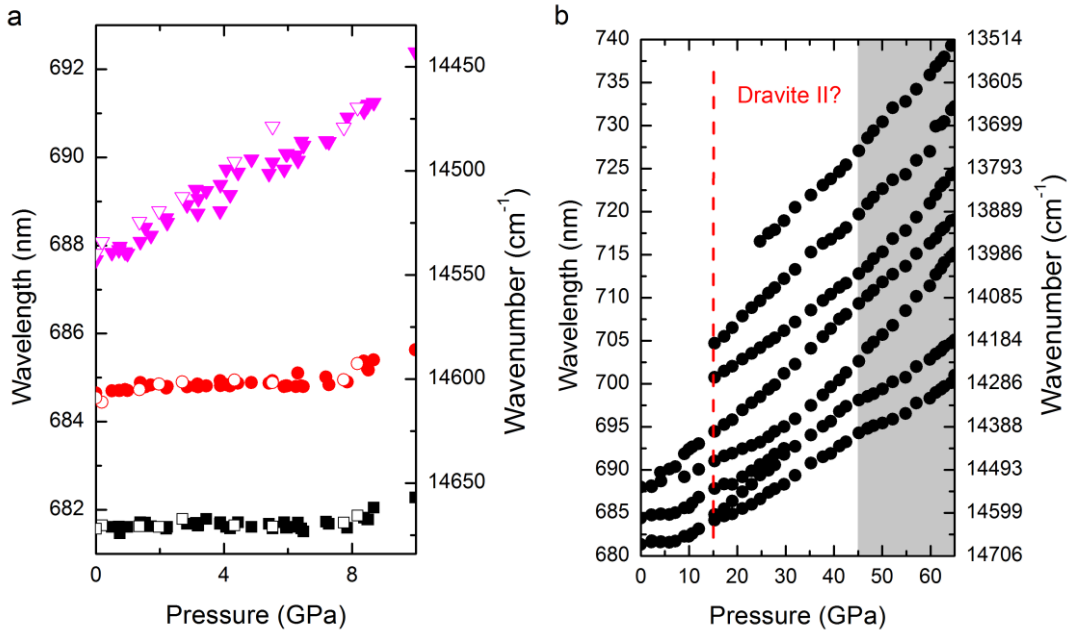

Figure 5.5. Pressure shift of the observed luminescence bands in dravite (a) low pressure region detailing the essentially 0 nm/GPa pressure shift of two of the emission bands and (b) up to 65 GPa. Grey box represents a possible change in compression mechanism. Closed symbols are data collected on compression, and open symbols are on decompression. Error bars are smaller than the symbols.

In the higher pressure regime, peak splitting is observed near 15 GPa, and new emission bands are observed, and at pressures above 45 GPa non-linear pressure shifts are observed (Figure 5.5b). No hysteresis is observed on decompression from 65 GPa, and the Raman spectrum of the decompressed sample is identical to the starting material. Peak splitting of emission bands under

compression has been shown to be an indicator of a phase transition (O'Bannon and Williams 2016a,b), and particularly in cases where multiple octahedral environments arise due to decreased symmetry at high pressures. For example, in the ring silicate beryl, the Cr^{3+} R-lines split into two sets of R-lines near 14.7 GPa (O'Bannon and Williams, 2016b) which agrees well with a theoretically predicted ~15 GPa soft-mode transition (Prencipe et al. 2011), as well as high-pressure single crystal diffraction studies which show that the Al-site splits into two crystallographically unique sites near 15 GPa (Personal communication M. Merlini). The peak splitting observed in dravite tourmaline (Figure 5.6) under compression provides clear evidence that one of the octahedral sites splits into two unique sites. Moreover, the additional new bands that appear at the same pressure (Figure 5.4, 5.5b) are likely neighbor lines that are due to paired Cr-Cr emission. These bands probably become resolvable for two reasons: (1) the intensity of the broad $^4T_2$ transition has decreased substantially by this pressure and alternate mechanisms for emission are enhanced, and/or (2) there is a change in the nearest neighbor configuration due to the splitting of one of the octahedral sites into two unique sites that produces configurations that favor the magnetic interactions that generate emission from pairs (O'Bannon and Williams 2017).

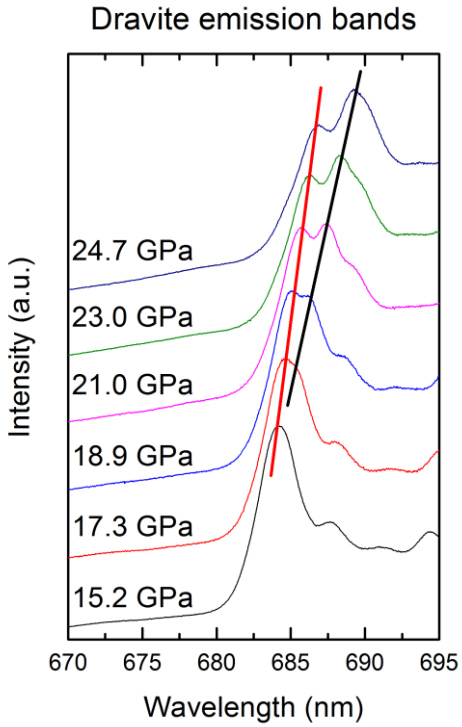

Figure 5.6. Detail of dravite emission band showing the splitting that is observed under compression.

Aside from the change in pressure shift near 9.0 GPa and the peak splitting and increased intensities of new peaks observed at ~15 GPa, the luminescence spectra do not show any other major changes. The lack of hysteresis on decompression from ~10.5 to 65 GPa suggests that any phase transition associated with these changes is second order in nature. We do not believe that the change observed at 9.0 GPa is produced by a pressure-induced structural phase transition, but is likely generated by either a change in compression mechanism or a progressive change in the electron density associated with the site. The changes observed at ~15 GPa are, however, consistent with a phase transition that involves a subtle distortion of the overall structure of dravite tourmaline that splits the Al-site

into two unique sites. By analogy to high-pressure phase transitions in cordierite and beryl (Prencipe et al. 2011; Miletich et al. 2014; Finkelstein et al. 2015; O'Bannon and Williams 2017), the structural change likely involves a modest distortion of the Si_6O_{18} ring away from hexagonal symmetry. Importantly, the overall topology of the structure appears to be preserved and a lowering of symmetry from rhombohedral is unlikely. The presence of such a modest structural change implies that dravite tourmaline's metastability under room temperature compression to 65 GPa is generated by the notable stability of tis Si_6O_{18} ring, with only modest modifications. Moreover, a structural transition that involves a modest distortion of the Si_6O_{18} ring with no change in crystal system would be difficult to constrain with powder diffraction techniques (e.g., Li et al. 2004; Xu et al. 2016).

5.3.3 High-pressure single-crystal diffraction

In order to characterize the changes observed using luminescence spectroscopy, X-ray diffraction measurements were done at various pressures up to ~15.4 GPa. Dravite tourmaline indexes to a rhombohedral unit cell across the pressure range of the single-crystal measurements. Structures solved as rhombohedral *R3m* up to ~15 GPa, and above this pressure the space group changed to *R3*. In the following sections, we discuss (1) the equation of state (EOS) for the low pressure phase of dravite tourmaline and compare it to the previous studies of schorl and uvite tourmaline (Li et al. 2004; Xu et al. 2016), (2) high-pressure crystal structures, and (3) the nature of the high-pressure phase transition of tourmaline.

5.3.4 Dravite tourmaline equation of state

Dravite tourmaline shows highly anisotropic compression (Figure 5.7), with the *c*-axis being substantially more compressible than the *a*-axis, which is in good agreement with the previous studies of schorl and uvite tourmaline (Li et al. 2004; Xu et al. 2016). Notably, the lattice parameters and unit cell volumes reported by Li et al. (2004) are relatively scattered. The reason for the scatter in their data is not clear, but could be a result of non-hydrostatic conditions of methanol:ethanol mixtures above ~10.5 GPa. We fit our pressure volume data using the EOSFit7GUI (Angel et al. 2014), and our results are shown in Table 5.1. Our results indicate that dravite tourmaline is more compressible than uvite tourmaline. For comparison, the uvite sample measured by Xu et al. (2016) is not an endmember, but has ~10 % Na in the X-site, and pure uvite is likely less compressible than their measurements. The relatively large value for K_o reported for schorl tourmaline by Li et al. (2004) does not appear compatible with our results nor those of Xu et al. (2016).

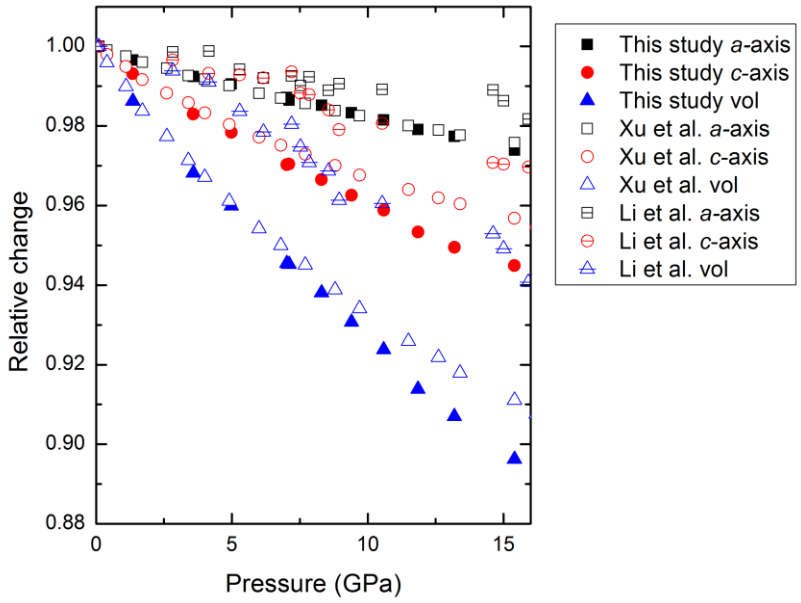

Figure 5.7. Relative change of lattice parameters and unit cell volume for schorl (Li et al. 2004), uvite (Xu et al. 2016), and dravite (this study). Error bars for our study are smaller than the symbols.

Sample	V_0 (Å^3)	K_0 (GPa)	K'_0 (GPa)	Method	Reference
Na-Fe	1595.52(1.98)	183.5(4.2)	4(fixed)	Powder XRD	Li et al. (2004)
Ca-Mg	1537.1(11)	96.6(9)	12.5(4)	Powder XRD	Xu et al. (2016)
		120(2)	4(fixed)	Powder XRD	Xu et al. (2016)
Na-Mg	1578.21(17)	111.3(1.0)	4.3(4)	Single crystal	This study
		112.1(0.2)	4(fixed)	Single crystal	This study

Table 5.1. Pressure-volume data fit up to ~15 GPa using both 2nd and 3rd order finite strain equations.

5.3.5 High-pressure crystal structures

Structures were solved at various high pressures, and results of the structure refinements are shown in Table 5.2. The site volumes as a function of pressure show that the Na site is the most compressible (Figure 5.8). The Si site is the least compressible, while the two octahedral sites are essentially identical to one another

and are intermediate in their compressibility. There is no indication that either octahedral site volume is constant under compression. So, the unusual observation of a negligible pressure shift of two of the luminescence bands cannot be explained by a site volume argument alone: a more nuanced explanation for the shift of the energy levels, involving a shift in covalency/electron density of the site that counterbalances the volumetric compaction, appears necessary. The anisotropic compression of dravite tourmaline can be straightforwardly explained by the location of the Na site in the dravite structure and its large volume change under compression (Figure 5.8). Speculatively, the large volume change in the Na site could produce a reduction in the electron density around the Al-sites, such that their electron density remains fairly constant under compression up to ~9.0 GPa.

Pressure (GPa)	0.0001	1.4(1)	3.6(1)	5.2(1)	7.2(1)
Temperature (K)	298(2)	298(2)	298(2)	298(2)	298(2)
Space group	*R3m*	*R3m*	*R3m*	*R3m*	*R3m*
a (Å)	15.9370(6)	15.8818(8)	15.8165(7)	15.7860(7)	15.7323(7)
c (Å)	7.1749(3)	7.1257(4)	7.0528(3)	7.0198(3)	6.9617(4)
Volume (Å^3)	1578.19(14)	1556.53(18)	1527.96(15)	1514.95(15)	1492.21(16)
R_1 (%)	2.06	3.39	4.54	4.40	5.44
wR_2 (%)	5.66	8.77	11.28	11.36	14.33
Goodness-of-fit	1.177	1.206	1.136	1.307	1.126
No. refined parameters	88	44	44	44	44

8.4(1)	9.8(1)	10.8(1)	11.9(1)	13.2(1)	15.1(1)
298(2)	298(2)	298(2)	298(2)	298(2)	298(2)
R3m	*R3m*	*R3m*	*R3m*	*R3m*	*R3m*

15.8818(8)	15.6711(7)	15.6418(10)	15.592(2)	15.5767(14)	15.521(2)
7.1257(4)	6.9066(4)	6.8794(5)	6.8253(11)	6.8127(7)	6.7796(11)
1556.53(18)	1468.91(16)	1457.7(2)	1436.9(4)	1431.5(3)	1414.5(4)
3.28	3.28	4.57	4.03	4.63	3.12
7.21	7.21	11.11	8.92	9.30	8.71
1.068	1.068	1.195	1.181	0.775	0.789
44	44	44	44	44	44

Table 5.2. Crystal structure refinement details for dravite tourmaline at various pressures.

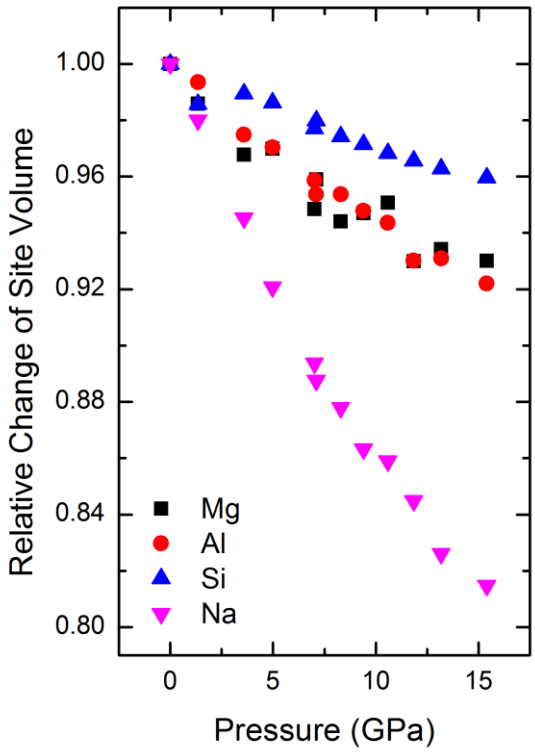

Figure 5.8. Site volumes in dravite tourmaline as a function of pressure. Note the large difference in compressibility between the Na site and the Si, Al, and Mg sites.

We calculate the distortion parameters for the octahedral and tetrahedral sites as a function of pressure, and these are shown in Figure 5.9. Interestingly, the quadratic elongation (QE) and angle variance (AV) of the Mg site both decrease under compression, indicating that this site becomes less distorted under

compression. The Al site distortion changes by very little, and the Si site becomes slightly more distorted under compression. The Al-site distortion change is negligible, which provides confirmation for our assignment of the two emission bands with invariant positions that also show no change in their splitting up to ~9.0 GPa to this site. Moreover, given the decreases in both the QE and AV of the Mg site, the assignment of the third emission band with a slight narrowing of the peak width under compression to ~9.0 GPa to this site also is compatible with the structural trends that we observe.

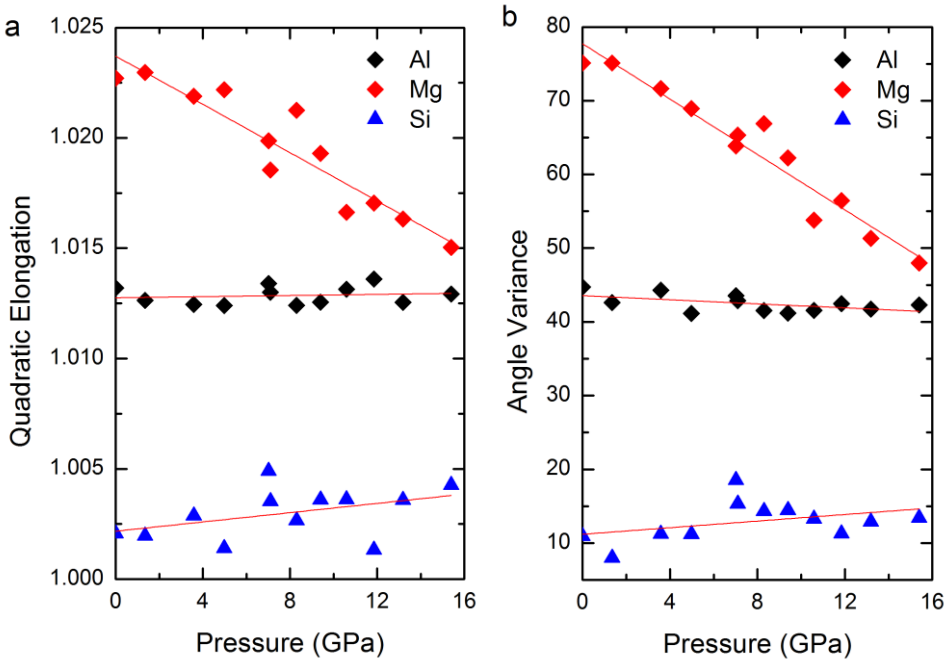

Figure 5.9. Quadratic elongation (QE) and angle variance (AV) of the Al, Mg, and Si sites in dravite tourmaline. An ideal octahedron or tetrahedron has a QE of 1 and an AV of 0. QE and AV are calculated using the equations below (Robinson et al. 1971).

The X-site in tourmaline (the Na site in dravite) is typically considered a 9-fold coordinated site. Among the bond lengths of this site as a function of pressure

(Figure 5.10), there are two unique bonds between the Na and the Si_6O_{18} ring, and there is one unique bond between the Na and the Mg octahedra. There is also a potential 10^{th} coordinating oxygen atom, which is also shown in Figure 5.10 (O10), and which may become a bond at higher pressures. Interestingly, the two unique Na-O bonds to the Si_6O_{18} ring show different behaviors. Under compression to ~15 GPa, one of the Na-O-Si bonds changes by ~0.05 Å while the other Na-O-Si bond changes by 0.25 Å. Across the same pressure range, the Na-O-Mg bond changes by ~0.11 Å. In this sense, the Na site appears to undergo the bulk of its compaction through six neighbors: three bonds into the Si_6O_{18} ring and three bonds into the Mg octahedra. This pseudo-six-fold behavior, with compacting connections to both the Mg polyhedra and the Si-ring, also sets up a natural way to distort the Si_6O_{18} ring away from hexagonal.

The distance to the potential 10th oxygen decreases by ~0.43 Å, and the pressure dependence of its distance is constant to 15 GPa. If a bonding interaction initiates between the Na and this 10th oxygen, it likely has a formal onset at pressures greater than 15 GPa, or distances shorter than 2.8 Å. The topology of the structure indicates that this additional interaction provides the only straightforward means to further polymerize this structure. Speculatively, the non-linear pressure shift of the luminescence bands above 45 GPa may be an indication that the Na site has changed coordination, producing a change in the compressional mechanism of the structure. The BO_3 groups change very little under compression and approach a

symmetrization of their bond length under compression (Figure 5.11). The error bars on the B-O distances are large; this is not surprising, considering the small scattering cross section of boron. There is no indication that the BO_3 groups deviate from a planar configuration up to at least 15 GPa.

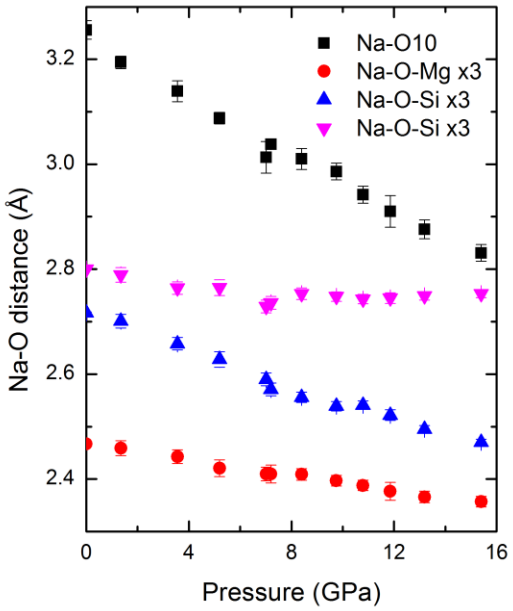

Figure 5.10. Na-O bond lengths of dravite tourmaline as a function of pressure.

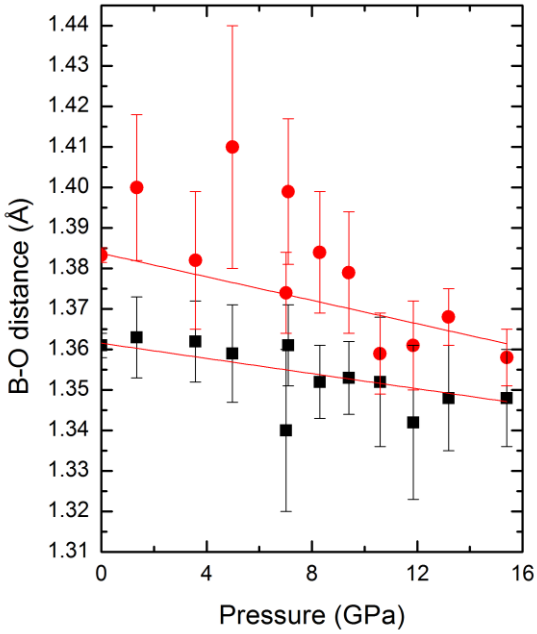

Figure 5.11. B-O bond lengths as a function of pressure. The BO_3 group shows an approach towards bond length symmetrization under compression.

5.3.6 High-pressure phase transition

At pressures above 15 GPa, dravite tourmaline is solved as rhombohedral R3. The only difference in symmetry associated with this transition is the loss of a mirror plane in the high-pressure structure. The net result is that the Si_6O_{18} ring distorts away from hexagonal to more of a ditrigonal configuration (Figure 5.12). This splits the Si site into two unique Si sites, as well as splitting the Al sites into two unique sites. Since the 3-fold rotation axis is preserved across this phase transition there is no change in the Mg, Na, or B sites. Importantly, this subtle crystallographic change is consistent with our luminescence observations of a second order phase transition occurring near ~15 GPa. Interestingly, this slight distortion of the Si_6O_{18} ring preserves the overall topology of the tourmaline structure, while providing a new

deformation mechanism for the high-pressure phase. Our luminescence data shows that this high-pressure phase is metastable under room temperature compression up to at least 65 GPa.

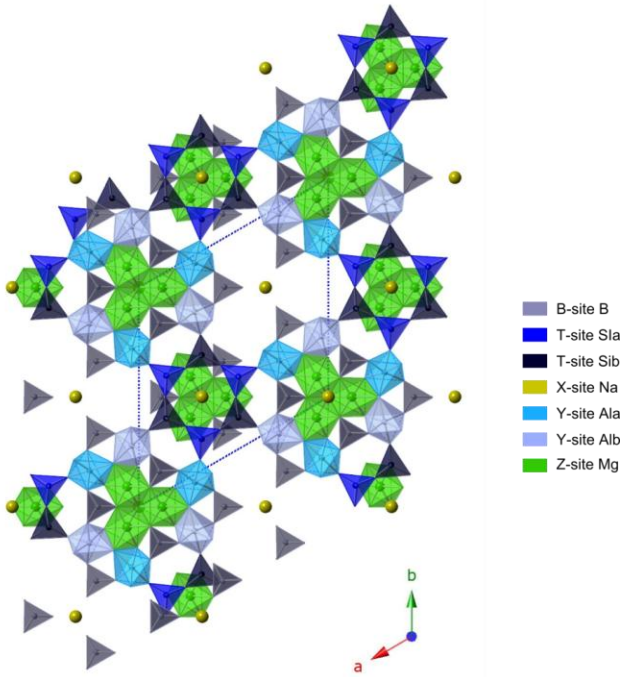

Figure 5.12. Crystal structure diagram of rhombohedral *R3* dravite tourmaline at 16.7 GPa. Note the Si_6O_{18} rings are distorted away from hexagonal, and two unique Si and Al sites are present in the high-pressure phase of dravite tourmaline.

Notably, there is no way to unambiguously distinguish between spacegroups *R3m* and *R3* by using systematic absences of reflections. Thus, caution is motivated when proposing that such a transition is occurring. This is especially true when dealing with high-pressure single-crystal data, which are often incomplete. For dravite, we believe this change in symmetry is robust for the following reasons: (1) structure solution of the complete room pressure data (and our data to 15 GPa) as rhombohedral *R3* results in an Si_6O_{18} ring that is hexagonal, (2) our luminescence

data indicate that a subtle second order phase transition occurs near this pressure, (3) there are no indicators that suggest that the different Al or Si sites are highly correlated in our results below 15 GPa, implying that our structural model is not missing any symmetry elements, and (4) structure solution of the 13.2 GPa structure as rhombohedral *R3* results in a slightly distorted Si_6O_{18} ring, with an R_1 value that is similar to the *R3m* solution. However, the Al and Si sites show correlations using the *R3* symmetry that indicate that we are missing a symmetry element at this pressure. In contrast, we can solve the ~15.1 GPa structure as either *R3m* or *R3,* with both solutions having similar refinement parameters. This suggests that the transition occurs between ~13.2 and 15.1 GPa (in accord with our luminescence results). Notably, by 16.7 GPa, the structure can no longer be solved as *R3m*: *R3* is required.

5.4 Conclusions

The basic compressional mechanisms of dravite tourmaline can be understood through the topology of the tourmaline structure. Tourmaline does not have open channels in its structure, and the Si_6O_{18} rings are stabilized by bonding with a large cation (e.g. Na, Ca, K), and there is typically very little substitution of other elements into the Si site. The tourmaline structure is, in effect, a more polymerized relative of the beryl and coriderite structures. Compression is accommodated by a large decrease in volume of the large cation X-site, contraction of the Al-O bond lengths with no change in Al-site distortion, a contraction of the Mg-O bond lengths and tilting of the Mg sites which results in a decrease in the Mg

site distortion, and an approach towards symmetrization of the BO_3 bond lengths. Hence, under compression to ~15 GPa, the Si_6O_{18} ring cannot easily distort away from hexagonal symmetry due to the cation bound into the ring: this contrasts with beryl and cordierite, which have an open channel within the ring. Under compression, the silicate rings in both beryl and cordierite distort away from hexagonal and become more oval shaped (Miletich et al. 2014; Finkelstein et al. 2015; O'Bannon and Williams 2016b). Essentially, cordierite and beryl evolve towards a more polymerized structure under compression.

Other compositions of tourmaline that are rhombohedral R3m at room temperature and pressure will likely behave similarly under compression. The main difference will be the pressure at which the distortion of the Si_6O_{18} ring from hexagonal occurs. Tourmaline is a complex group of minerals, and the high-pressure behavior of tourmalines with extensive Li, Cr, or V substitution into the Y and Z sites, Pb substitution into the X-site, or Al, Li substitution into the T-sites could be quite different than that of tourmalines with predominantly Al and Mg in their Y and Z sites. Nevertheless, the main control over the pressure at which this transition occurs is likely the identity of the cation in the X-site. Here, the simplest systematics would indicate that a larger cation would generate this distortion at lower pressure conditions. Thus, the pressure of this transition in uvite variety tourmaline $[Ca(Mg_3)MgAl_5(Si_6O_{18})(BO_3)_3(OH)_3(OH)]$ and maruyamaite variety tourmaline $[K(MgAl_2)(Al_5Mg)(BO_3)_3(Si_6O_{18})(OH)_3O]$ would be lower than in dravite tourmaline.

Chapter 6

Beryl-II, a high-pressure phase of beryl: Raman and luminescence spectroscopy to 16.4 GPa

6.1 Introduction

Beryl is a beryllium ring silicate that crystallizes in the hexagonal crystal system with *P6/mcc* symmetry (Figure 6.1). Emerald ($Be_3Al_2Si_6O_{18}$:Cr) is a chromium-bearing variety of beryl, and most emerald samples also contain hundreds to thousands of ppm of vanadium (Ollier et al. 2015). Ring silicates have attracted considerable interest due to their unusual thermal expansion behavior, as well as the ability for their zeolite-like channels to contain a wide range of volatiles (e.g. H_2O, CO_2, etc.). For example, the structurally-related ring silicate cordierite ($(Mg,Fe)_2Al_4Si_5O_{18}$) on being heated to ~800 ^{O}C expands along the *a*-axis, but contracts along the *c*-axis (Milberg and Blair 1977; Hochella and Brown 1986). The high-temperature behavior of beryl is comparable: when heated to ~800 ^{o}C, it behaves much like cordierite. Below ~300 ^{o}C, the *c*-axis contracts with increasing temperature, but expands at higher temperatures (Morosin 1972; Fan et al. 2015). Interestingly, the high-temperature behavior of emerald shows a shallower minimum in the *c*-axis contraction with temperature, and the minimum distance is shifted to temperatures of ~100°C by only 0.5 wt% Cr-substitution into the Al^{3+} sites (Morosin 1972). This has been attributed to expansion of the unit cell of emerald relative to end-member beryl, since Cr^{3+} has a larger ionic radius than Al^{3+}. Ring silicates such as cordierite have widespread industrial uses as ceramic materials, but the industrial applications of beryl have been more limited, and are usually highly specialized due

to the toxicity associated with beryllium (Hochella and Brown 1986). Emerald has attracted more interest as a tunable laser material (Buchert et al. 1983; Lai 1987), and has also been mined as a gem since before the start of the Egyptian Ptolemaic Kingdom.

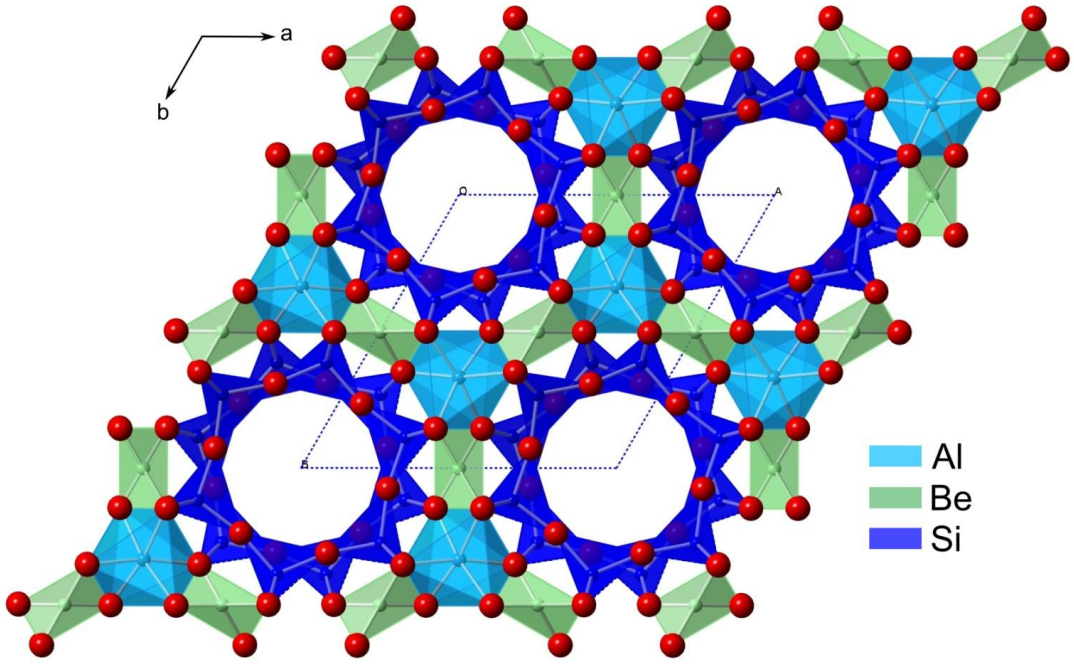

Figure 6.1. Crystal structure of beryl looking down the *c*-axis. Structure after Gibbs et al. (1968). Dashed line indicates the unit cell. Crystal structure diagram generated using v8.7.6 CrystalMaker®.

The high-pressure behavior of ring silicates such as cordierite and tourmaline has also attracted interest due to their occurrence in subduction zone environments and their widespread industrial uses (Likhacheva et al. 2012; Miletich et al. 2014a; Miletich et al. 2014b; Finkelstein et al. 2015; Xu et al. 2016). Experimental high-pressure investigations of beryl are limited to X-ray diffraction studies and one luminescence study. Early high-pressure single-crystal work on a synthetic

chromium-bearing beryl sample by Hazen and Finger (1986) extended to ~5.7 GPa. Hazen and Finger (1986) reported high-pressure structures up to a maximum pressure of 5.7 GPa, and did not observe any phase transitions. Qin et al. (2008) conducted high-pressure powder diffraction on natural beryl up to ~19.2 GPa and did not observe a phase transition, but the composition of their sample is unknown. More recently, Fan et al. (2015) conducted both powder diffraction to 16.7 GPa and single crystal diffraction to 9.5 GPa on a natural colorless gem quality beryl sample of unknown composition. They did not report high-pressure crystal structures, and also did not observe a phase transition. Prencipe et al. (2005) conducted single-crystal high-pressure X-ray diffraction on natural colorless beryl to ~6.3 GPa in order to obtain accurate unit cell parameters as a check on their theoretical calculations. A previous high-pressure study of Cr^{3+} luminescence spectra of emerald up to ~5.0 GPa reports that the pressure-induced red shift of the main R-line differs by ~20% between natural and synthetic samples of emerald (Sánchez-Alejo et al. 2011). To our knowledge, high-pressure vibrational spectroscopic studies of beryl have not been reported. On the theoretical side, ab initio calculations on high pressure, high-temperature behavior and the mechanics of the compression of beryl have been conducted (Prencipe and Nestola 2005, 2007; Prencipe et al. 2011). Prencipe et al. (2011) predict that a second order, soft-mode induced phase transition occurs at ~14 GPa, with a lowering of symmetry from hexagonal *P6/mcc* to triclinic $P\bar{1}$. A private communication is quoted from M. Merlini in Prencipe et al. (2011) that preliminary high-pressure single crystal and polycrystalline measurements on beryl of unknown

composition indicate that the symmetry may lower at pressures near 14 GPa. However, the interpretation of these results was complex because of the possible presence of twinning (Prencipe et al. 2011), and these experimental results have not yet been published.

We utilize the fluorescence of chromium and vanadium to probe the high-pressure behavior of natural emerald. Investigations of the high-pressure behavior of Cr^{3+} or V^{2+} luminescence have largely been restricted to relatively simple oxides and rare-earth bearing garnets (Chopelas and Nicol 1982; Kottke and Williams 1983; Wamsley and Bray 1994; Jovanić 1997, 2000; Jovanić et al. 2010). Of these, the most well-characterized material is ruby (Al_2O_3:Cr), whose role as a pressure calibrant is well-known (Piermarini et al. 1975; Mao et al. 1986). Ruby is also the model system through which much of crystal field theory was developed (Sugano and Tanabe 1958; Burns 1993). The materials that have had their luminescent behavior probed under pressure share a few general properties: they are simple oxide systems, they are not hydrated, and they all have Al-sites that are close to ideal octahedra. High-pressure investigations of Cr^{3+} luminescence from more distorted Al-sites in silicates and oxides are limited (e.g., O'Bannon and Williams 2016a). And, high-pressure studies of the simultaneous emission of two or more luminescent centers in oxides have been largely confined to studies on charge transfer between transition metal elements and rare earth elements in garnets (Shen et al. 2000).

Since both Cr^{3+} and V^{2+} have a d^3 configuration, their luminescence spectra are quite similar. The main differences lie in the intensity, wavelength, and lifetime of

emission associated with these transition metals. The emission of Cr^{3+} and V^{2+} is typically characterized by relatively narrow intense R-lines associated with the spin-forbidden ^2E-$^4A_2$ transition, with the $^4A_2$ state being the ground state and the ^2E state being split in non-cubic environments (Syassen 2008). At high field strengths, the narrow band ^2E-$^4A_2$ emission typically dominates the fluorescence spectrum, while at low crystal-field strengths the generally broader (and spin-allowed) $^4T_2$-$^4A_2$ emission dominates the emission spectrum, and at intermediate field strengths both can occur together (Sugano and Tanabe 1958; Burns 1993; Gaft et al. 2005). In samples with significant Cr^{3+} or V^{2+} substitution, sharp neighbor lines (N-lines) generated by shared excitations between neighboring Cr^{3+} or V^{2+} centers can also be observed. These bands tend to be complex, since a wide variety of potential neighbor interactions exist (especially in complex crystal structures). If their assignments are known, their pressure-dependence can be used to estimate changes in magnetic interactions between chromium centers (Williams and Jeanloz 1985). In addition to these electronic transitions, vibronic bands are also observed. These phonon-associated sidebands are offset from the R-lines by the frequency of a lattice phonon or a local vibrational mode.

Here, we use Raman spectroscopy to probe the bonding environment of beryl up to ~15 GPa, and Cr^{3+} and V^{2+} luminescence to probe the Al site in emerald ($Be_3Al_2Si_6O_{18}$:Cr,V) under compression up to 16.4 GPa. The Cr^{3+} luminescence spectrum of emerald under compression has been previously reported but was characterized only to ~5.0 GPa (Sánchez-Alejo et al. 2011). They reported solely the

pressure dependence of the R1 line, although the emission spectrum also contains the Cr^{3+} $^4T_2$ emission, the R2 band, linewidths, and, for some compositions, V^{2+} emission. With respect to the vibrational spectra, high-pressure Raman spectroscopic studies on beryl appear not to have been previously conducted. Thus, our experiments are oriented towards: (1) probing the local bonding environment and of the Si_6O_{18} rings and Al/Be sites to constrain their high-pressure behavior, (2) resolving the ^2E and $^4T_2$ emission bands from both Cr^{3+} and V^{2+} in the same crystal structure under compression, (3) determining whether any phase transition occurs, such as the soft-mode transition that has been proposed to be present near ~14 GPa as predicted by theory (Prencipe et al. 2011), (4) determining how the crystal field strength in emerald changes under compression, and (5) examining how the symmetry of the Cr-substituted Al sites might change under compression by examining shifts in splitting and linewidths of luminescence peaks.

6.2 Experimental Methods

The beryl samples are from Rabenstein, Zwiesel, Lower Bavaria, Germany (UCSC sample # 6533), and the emerald samples are from the Boyacá Department, Columbia. Both beryl and emerald sample purity was confirmed by Raman, infrared, and luminescence spectroscopy, each of which were in good agreement with previous studies (Wood and Nassau 1967; Hofmeister et al. 1987; Hagemann et al. 1990; Sánchez-Alejo et al. 2011). Moreover, both samples consisted of gem quality euhedral single crystals with typical beryl crystal habit. The beryl sample is light green in color, while the emerald sample is a characteristic emerald/deep green color.

The beryl sample was selected for the Raman measurements due to its low luminescence background, and the emerald sample was selected for the relatively high amplitude of its narrow band (R-line) emission relative to broad-band emission. Trace element concentrations of the beryl and emerald were measured with a PhotonMachines Analyte 193H, which is a 193 nm ArF excimer laser system coupled with a ThermoScientific ElementXR single-collect or magnetic sector ICP-MS. The instrument was calibrated with a SRM 610 trace element glass from NIST, and Al was used as the internal standard. The results are shown in Table 6.1.

Sample	Mg	Na	Ti	Mn	V	Cr	Fe
beryl	1243 (±34)	2938 (±68)	13 (±6)	31 (±4)	-	-	3471 (±217)
emerald	1826 (±91)	1430 (±415)	-	-	760 (±75)	1235 (±105)	265 (±45)

Table 6.1. Trace element concentrations of beryl and emerald. All measurements are given in ppm, and dashes indicate that the concentration was below the detection limits of out method.

High static pressures were generated using a Merrill-Bassett type diamond anvil cell (DAC) equipped with 16 sided type 1a 500 μm culet diamond anvils. A spring steel gasket with a 200 μm hole was used as the sample compartment. Experiments were carried out with a methanol:ethanol 4:1 mixture as the pressure media, which yields hydrostatic conditions up to ~10.5 GPa (Piermarini et al. 1973; Fujishiro et al. 1982; Klotz et al. 2009). Single crystals of both the sample and ruby were loaded into the sample compartment, and to prevent contamination of the sample luminescence spectra by the intense ruby luminescence, the small ruby crystals (ca. 2 μm diameter), and the emerald were spatially separated within the

sample. The standard ruby fluorescence method was used to determine the pressure (Mao et al. 1986). For the low temperature, ambient-pressure measurements, the sample was immersed in liquid nitrogen.

High-pressure Raman spectra were collected using a 600 lines/mm grating and 633 nm excitation between 75 and 1200 cm^{-1}, while high-pressure luminescence spectra used a 1800 lines/mm grating with 532 nm excitation from 650-800 nm (15380-12500 cm^{-1}). Both Raman and luminescence spectra were measured using a Horiba LabRAM HR Evolution Raman spectrometer with a spectrometer focal length of 800 mm. An Olympus BXFM-ILHS microscope with a 50x long working distance objective was used to focus the laser beam onto the sample. Raman spectra were collected to a pressure of ~15 GPa, and luminescence spectra were collected to a pressure of ~16.4 GPa and on decompression to room pressure at 298 K. Infrared spectra were collected from 400-8500 cm^{-1} using a Bruker Vertex 70v evacuated Fourier transform infrared spectrometer (FTIR) equipped with a globar source, KBr-beamsplitter, and a liquid-N_2 cooled mercury-cadmium-telluride (MCT) detector. Infrared spectra have a resolution of 4 cm^{-1}. Vibrational and luminescence spectra were fit using a combination of Gaussian and Lorentzian functions with either Horiba Labspec6 software or Bruker OPUS6.5 software.

6.3 Results and discussion

6.3.1 Room pressure luminescence and vibrational spectra

Raman spectra of beryl and emerald under 532 nm excitation are shown in Figure 6.2a and are in excellent agreement with previous studies (Wood and Nassau

1967; Hofmeister et al. 1987; Hagemann et al. 1990). Due to the broad luminescence background of Cr^{3+} and V^{2+} emission, the Raman active H_2O modes in the ~3600 cm^{-1} range of emerald could not be resolved. Mid-infrared absorption spectra of the emerald show that both type I and II water are present within the channels (e.g., Wood and Nassau 1967). H_2O combination bands and the 1st overtone of H_2O are also present in the spectra (Figure 6.2b). Raman spectrum of the OH region in beryl did not have interference from luminescence, and type I and II water is observed in the channels (Figure 6.2b inset). Very weak Raman modes are observed at ~1385 cm^{-1} in both beryl and emerald, and are due to CO_2 contained in the channels. Assignments and peak positions of observed Raman modes are shown in Table 6.3.

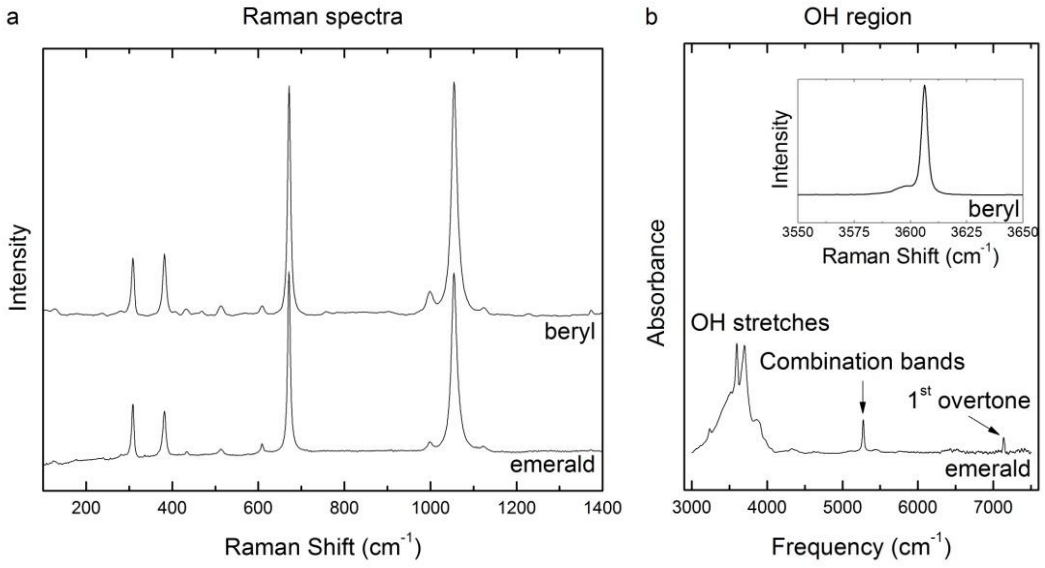

Figure 6.2. Room pressure and temperature (a) Raman spectra of beryl and emerald in the lattice- and ring-vibration region and (b) Raman spectra of the OH-stretch region in beryl and infrared of the OH-stretch and overtone region of the emerald sample.

ν_{0i} (cm^{-1})	Assignment	($d\nu_{0i}/dP$) to 14GPa (cm^{-1}/GPa)	γ_i
138.2	E_{1g}	-4.57 (±0.55)	-5.95
317.6	ring & Al distortion	0.99 (±0.19)	0.56
390.6	ring breathing	0.40 (±0.08)	0.18
440.0	Si & Be bending	1.47 (±0.31)	0.60
520.1	Si & Be bending	3.65 (±0.27)	1.26
678.2	Si & Be bending	2.75 (±0.24)	0.73
1004.8	Si-O2 stretch + O2-Al/Be-O2 deformation	6.93 (±0.28)	1.24
1061.0	Si-O2 stretch + O2-Al/Be-O2 deformation	5.76 (±0.56)	0.98

Table 6.2. Raman modes observed at high pressures (assignments based on Hofmeister et al. 1987 and Prencipe et al. 2006), pressure dependences of peak positions, and calculated mode Grüneisen parameters of beryl.

The assignments and deconvolution of the emission bands in emerald at room pressure and temperature under 532 nm excitation are shown in Figure 6.3 and listed in Table 6.3. In accord with prior work (e.g., Kisliuk and Moore 1967; Schmetzer and Eysel 1974; Ollier et al. 2015), we assign the sharp narrow emission bands to the transition from the ^2E states to the ground states of Cr^{3+} and V^{2+}: these are typically referred to as the R-lines. The splitting of the ^2E states into two components (R_1 and R_2) is a consequence of the site symmetry of Al in the beryl lattice being slightly distorted from octahedral: its site symmetry is D_3 (e.g., Gibbs et al. 1968). The broad emission bands are assigned to the transition from the $^4T_2$ states to the ground states of Cr^{3+} and V^{2+}. The Cr^{3+} $^4T_2$ emission band's location at 702.3 nm (14239 cm^{-1}) at room pressure and temperature is at substantially longer wavelength than the corresponding absorption of this transition near 615 nm (Kisliuk and Moore 1967).

Thus, the excited state of this transition is Stokes shifted to the long wavelength side of the R-lines, a phenomenon that has been well-documented in emerald (Kisliuk and Moore 1967). The $^4T_2$ emission band of V^{2+}, located at 731.55 nm (13669.6 cm^{-1}), is also Stokes shifted to longer wavelengths relative to its absorption band at ~667 nm (~15000 cm^{-1}) (Schmetzer and Eysel 1974). Our sample is grossly similar in Cr^{3+} and V^{2+} concentration to the Capoeirana, Brazil sample from Ollier et al. (2015), and we fit and assign our spectra similarly to their ambient-pressure study. The previous assignments of the V^{2+} ^2E and $^4T_2$ emission lines are based on lifetime measurements (Schmetzer and Eysel 1974; Ollier et al. 2015).

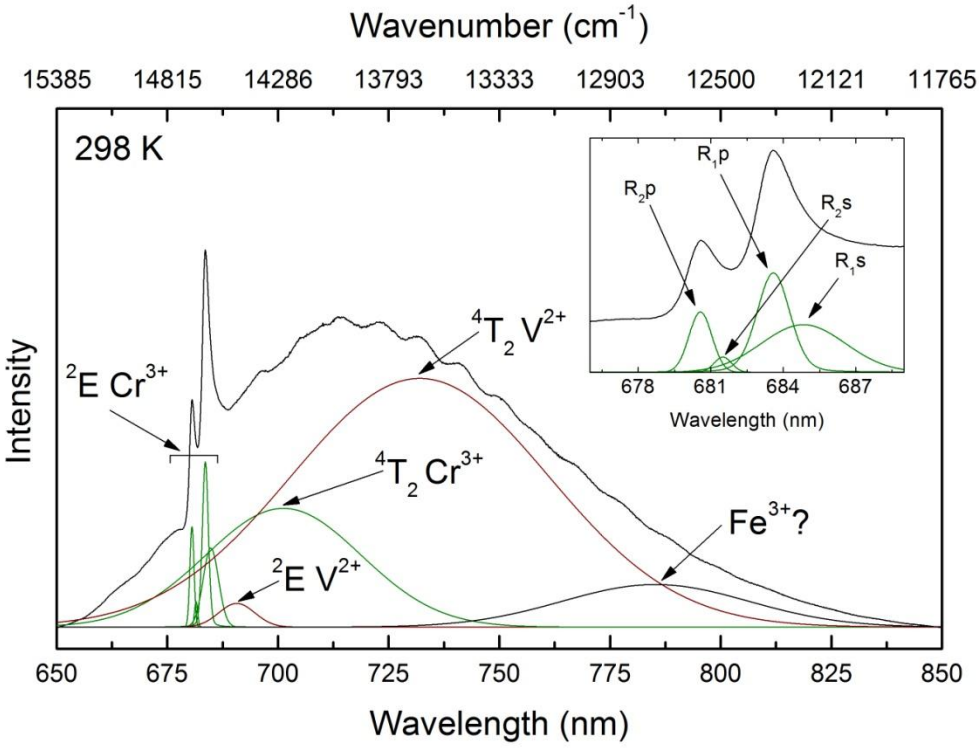

Figure 6.3. Typical deconvolution of emerald emission spectrum using 532 nm excitation. Assignment of emission bands based on Schmetzer and Eysel (1974) and Ollier et al. (2015). Green colored peaks are Cr^{3+} emission and wine colored peaks

are V^{2+} emission. Inset shows detailed ^2E fit with primary (p) and secondary (s) R_1 and R_2 lines. The modulation/fringing on the broad $^4T_2$ emission is an artifact.

Assignment	λ (nm)	ν (cm^{-1})	Low P phase dv/dP (cm^{-1}/GPa)	High P phase dv/dP (cm^{-1}/GPa)
R_2 Cr^{3+} primary	680.52	14694.7	-10.2 (±0.2)	-4.4 (±0.4)
R_2 Cr^{3+} secondary	681.83	14676.1	-10.0 (±0.4)	-9.8 (±0.4)
R_1 Cr^{3+} primary	683.58	14628.9	-10.7 (±0.2)	-3.0 (±0.4)
R_1 Cr^{3+} secondary	684.41	14611.1	-10.5 (±0.4)	-9.2 (±0.5)
R_1 V^{2+}	691.13	14469.1	-6.5 (±0.3)	-20.7 (±7.0)
$^4T_2$ Cr^{3+}	702.31	14238.7	12.5 (±1.6)	-12.7 (±4.6)
$^4T_2$ V^{2+}	731.55	13669.6	26.3 (±1.5)	-13.2 (±5.8)
Fe?	785.26	12732.6	-	-

Table 6.3. Assignment, position in wavelength and wavenumber, and pressure shift of emission bands in both emerald phases.

Unlike Ollier et al. (2015), we observe both the R_1 and R_2 lines from Cr^{3+} under steady state excitation (they observe R_2 only in time-delayed spectra), and we fit two components to each Cr^{3+} R-line (Figure 6.3 inset). The lower intensity component/shoulder of each R-line is located to the long wavelength side of the more intense component of the R-lines, and the presence of these additional components suggests that there are likely two modestly different Cr^{3+} sites, with most of the Cr^{3+} being present in the site represented by the more intense bands. We refer to the most intense component of the Cr^{3+} R-lines as the primary R-lines and the lower intensity components as the secondary R-lines. The origin of the secondary Cr^{3+} R-lines might be associated with local shifts in bonding associated with channel constituents. Certainly, the shift in energy of the secondary lines from the primary R-lines is slight, and water as a channel constituent affects the bonding of the adjoining silica tetrahedra (e.g., Fridrichova et al. 2016), and hence proximity to a water molecule in

a channel may modestly alter the charge density of the Al/Cr site and give rise to the secondary bands. Peak asymmetries, and the necessity of fitting absorption bands with two peaks of markedly different intensities, have also been noted in the absorption spectrum of emerald (Parkin and Burns 1980; Taran et al. 1994), and additional R-lines from separate Cr-sites (albeit on the short wavelength side of the primary R-lines) have been observed in very Cr-rich emerald (3 at%: Quarles et al. 1988).

The tandem of Cr^{3+} and V^{2+} can account for all of the emission bands observed, except for the broad low intensity band located at ~785 nm. Ollier et al. (2011) discuss the possibility that this broad low intensity band might be due to the ^2E to $^2T_2$ transition of Ti^{3+}, but note that this valence state is unlikely in geologic materials. They suggest that emission from ferric iron is the probable origin, due to the large full width at half maximum (FWHM) of the ~785 nm emission band. Moreover, a broad Fe^{3+} emission band near 770 nm has been reported in ruby doped with both Cr^{3+} and Fe^{3+} (Snytnikov et al. 2008). Hence, we tentatively assign the emission band at ~785 nm observed in our room-pressure and temperature measurements to Fe^{3+}, since the Ti concentration in our sample was below detection limits. Under compression, the intensity of this band decreases dramatically and becomes unresolvable, so the deconvolutions of our high pressure spectra do not include this feature.

The 77 K luminescence spectrum of emerald is shown in Figure 6.4. At 77 K and room pressure, the ^2E transition of Cr^{3+} and V^{2+} and pair emission lines of Cr^{3+}

and V^{2+} are the primary features in the spectrum. At 77 K, the Cr^{3+} R-lines shift to lower wavelength by ~1 nm and the splitting between R_1 and R_2 is lowered to 62.9 cm^{-1}, which is in accord with previous studies (Ohkura et al. 1987; Skvortsova et al. 2015). At low temperature (77 K), the broad thermally populated $^4T_2$ emissions of Cr^{3+} and V^{2+} are quenched. The secondary R- lines are still observed at 77 K (Inset in Figure 6.4), indicating that they are not populated by thermal effects, and supporting their origin as being derived from a separate Cr^{3+} site. Peak positions of Cr^{3+} neighbor lines are assigned after Ohkura et al. (1987) and shown in Figure 6.4 (dashed vertical lines). Neighbor-lines (N-Lines) are emission lines that are generally located to the longer wavelength side of the R-lines (lower energy) and are attributed to paired ion emissions. Interestingly, the previously assigned neighbor lines account for less than half of the observed sharp emission lines in the sideband region (indeed, many bands were not assigned by Ohkura et al., 1987). This demonstrates that this region consists of complex pair emission lines due to neighbor interactions from Cr^{3+} and probably V^{2+}–associated pairs.

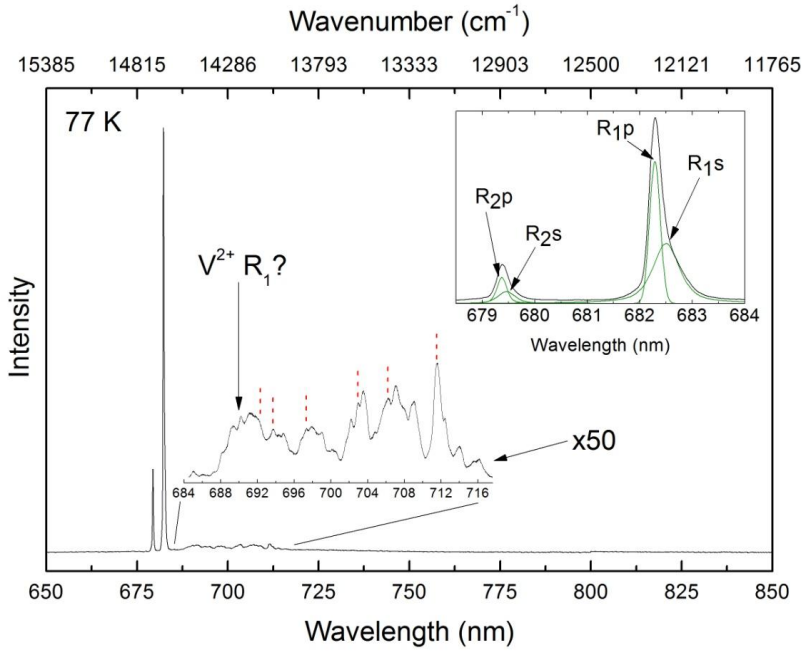

Figure 6.4. Representative room pressure 77 K luminescence spectra of emerald using 532nm excitation. The sharp emission lines in the x50 spectrum at low temperature are assigned to paired emissions of Cr and/or V (N-lines). Vertical red dashed lines are the subset of Cr N-lines that were assigned by Ohkura et al. (1987).

6.3.2 High-Pressure Raman Spectra

Representative high-pressure Raman spectra are shown on compression and decompression in Figure 6.5, and the pressure shifts of the Raman modes are shown in Figure 6.6. The assignments, pressure shift, and mode Grüneisen parameters of beryl are tabulated in Table 6.2. The assignments of the Raman modes of beryl have attracted interest (Hofmeister et al. 1987; Hagemann et al. 1990; Prencipe et al. 2006): for reference, there are 36 Raman-active modes of beryl predicted by factor group analysis (e.g., Prencipe et al. 2006). Most of the modes resolved in this study are assigned to either Si/Be-O stretching or bending vibrations, or ring breathing/distortions. Notably, the E_{1g} mode located at 138 cm^{-1} has a rapid negative

shift under compression. However, we do not resolve this band above ~5 GPa due to our lower frequency cut-off of ~100 cm^{-1}. Nevertheless, its negative pressure shift appears to become larger with increasing pressure, and a polynomial extrapolation of this mode to 0 cm^{-1} indicates that a soft-mode transition should occur near 12 GPa (Figure 6.6a). The calculations of Prencipe et al. (2011) indicated that this mode would be soft, and suggested that its pressure shift should induce a second-order, soft-mode transition near 14 GPa. Thus, given the pressure range over which we resolve this band, the agreement with theory (Prencipe et al. 2011) on both the shift and inferred pressure of a soft-mode transition in beryl/emerald is excellent (Figure 6.6a). The other Raman modes shift monotonically and positively up to ~11.2 and at 15.0 GPa, all observed Raman modes undergo discontinuous shifts, dramatic drops in intensity and broadening. On decompression, we do not observe hysteresis in the transition, although our bounds on the precise pressure of the transition in the Raman spectra are not tight.

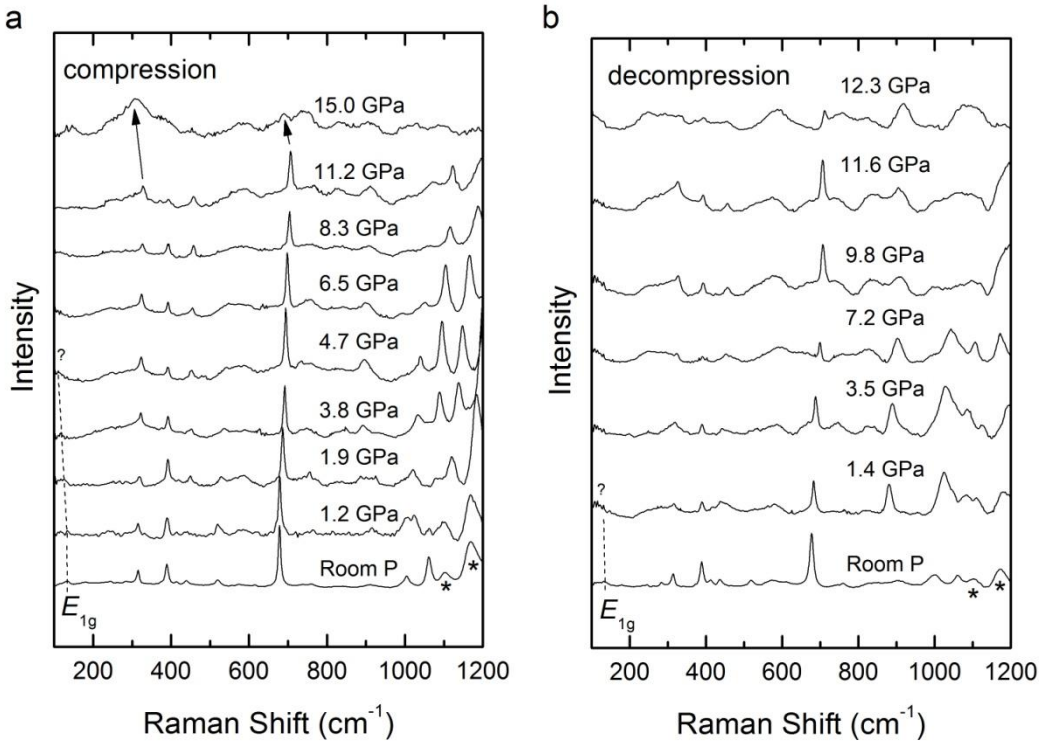

Figure 6.5. High-pressure Raman spectra of beryl under 633 nm excitation on (a) compression and (b) decompression. Asterisks indicate the position of Cr^{3+} R-lines in the beryl sample.

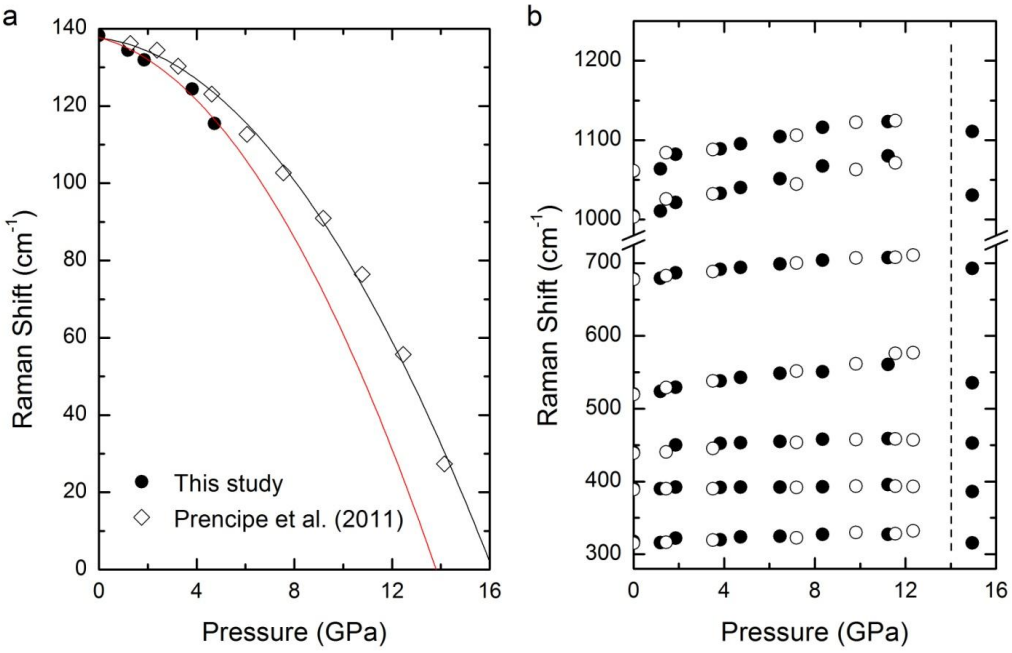

Figure 6.6. Raman mode shifts of (a) the low frequency E_{1g} mode, including from the calculation of Prencipe et al. (2011) and (b) the higher frequency lattice and silicate ring and Be modes.

We assign our modes in more detail using the calculated isotopic shifts of the Raman modes of Prencipe et al. (2006). The Si & Be bending modes at 440, 520, and 678 cm^{-1} have variable pressure shifts; of these, the 678 cm^{-1} mode has the largest degree of Be-motion, while the 520 cm^{-1} band predominantly involves Si and O motion, and the 440 cm^{-1} mode involves both Si- and Al-motion in addition to O, and its displacement appears to involve more of a bulk rotation of the silica tetrahedron (Prencipe et al. 2006, with its web link to mode displacements[1]). The smaller pressure shift of the 440 cm^{-1} band relative to the other two bands suggests that the internal tetrahedral deformational vibrations stiffen more rapidly under pressure than deformational vibrations associated with the rings: in this sense, the behavior of the

440 cm^{-1} band may more closely resemble that of the ring distortion and ring deformation vibrations at 318 and 391 cm^{-1}. Interestingly, the pressure shifts of the Si-O2 stretching and O2-Al/Be-O2 deformational vibrations at 1005 and 1061 cm^{-1} are quite rapid, indicating that vibrations associated with the O2 atom are particularly responsive to pressure. The idea that the O2 atom may play a key role in the high-pressure deformational behavior of beryl is precedented: Prencipe et al. (2006) note that the mechanics of compression of beryl primarily involve movement of the O1 and O2 atoms.

While we could detect no evidence of Cr^{3+} luminescence from this beryl under 532 nm excitation, under 633 nm excitation low intensity Cr^{3+} R-lines are observed (Figure 6.5a, 6.5b). This indicates that the ability to excite the R-lines in Cr-poor beryl is minimal at 532 nm, while at 633 nm the strong $^4A_{2g}$ -> $^4T_{1g}$ derived absorption band pumps the R-lines. Within Cr-rich emerald, the high-energy tail of this absorption band is sufficient to excite the R-line fluorescence. The emission lines in beryl are observed as contaminants in the Raman spectrum across the pressure range of this study and their pressure shifts, as described below, are essentially identical to the pressure shift observed in our emerald sample. The pressure shift of R_1 in our beryl sample is -10.5 (±0.5) cm^{-1}/GPa and for R_2 is -10.1 (±0.3) cm^{-1}/GPa. A more complete discussion of emerald Cr^{3+} R-line pressure shifts follows the next section.

[1] http://www.crystal.unito.it/vibs/beryl

6.3.3 Mode Grüneisen parameter

Using the pressure shift of a vibrational frequency ν_i for a mode *i*, ($d\nu_i/dP$), a mode Grüneisen parameter (γ_i) can be calculated using $\gamma_i = K_0/\nu_{0i}$ ($d\nu_i/dP$). Here, K_0 is the bulk modulus of beryl, for which we used a value of 180 (±2) GPa (Fan et al. 2014). Two previous studies reported indistinguishable values of K_0 of 179 (±1) and 181 GPa (Yoon and Newnham 1973; Prencipe and Nestola 2005), while Hazen and Finger (1986), in their single crystal study to 5.7 GPa, reported a value of K_0 of 170 (±5). The ν_{0i} values were determined by Raman spectroscopy at room temperature and pressure (Figure 6.2), and the calculated $d\nu_i/dP$ and γ_i are listed in Table 6.2. Notably, the E_{1g} mode at 138 cm^{-1} has a large negative Grüneisen parameter, which is in good accord with the calculated Grüneisen parameters reported by Prencipe at al. (2011). For comparison, the thermodynamic value of the Grüneisen parameter can be determined using the thermal expansion reported by Morosin (1972), coupled with the bulk modulus of 180 GPa (Fan et al. 2015), and the heat capacity at 300 K (Hemingway et al. 1986) using $\gamma_i = \alpha K_0/\rho C_p$. The calculated thermodynamic Grüneisen parameter is 0.27: this small value is a consequence of the relatively low thermal expansion of beryl at 300 K (3.26×10^{-6}/K: Morosin 1972). Our overall average mode Grüneisen parameter for the Raman bands in Table 6.2 is -0.05. This discrepancy is certainly associated with our sampling of the Raman modes of beryl being highly biased by a single, low-frequency, highly negative Grüneisen parameter soft mode.

6.3.4 High-Pressure Luminescence

In order to probe the effect of polymorphism on the luminescent spectrum, emerald was probed at high pressures through the transition observed using Raman spectroscopy. Representative high-pressure luminescence spectra on both compression and decompression are shown in Figure 6.7, and the pressure shifts of the Cr^{3+} and V^{2+} emission lines are plotted in Figure 6.8. The assignments and pressure shifts of the Cr^{3+} and V^{2+} emission bands are tabulated in Table 6.3. The primary and secondary Cr^{3+} R-lines shift smoothly and to lower energy under compression up to ~13.7 GPa where the primary lines split. Above ~13.7 GPa, the two components of the R_1 and R_2 bands have different pressure shifts (Table 6.3) which, in combination with their splitting, suggests that a phase transition has occurred. The splitting is clearly manifested in the R_1 band (Figure 6.9), while two overlapping (but deconvolvable) components are present in the R_2 band. Hysteresis of these splittings is not observed on decompression: they are fully reversible, which indicates that this transition is second order in nature. The pressure shift we observe up to 13.7 GPa of the primary R_1 line is similar to that of the previous study of Sánchez-Alejo et al. (2011) to 5.2 GPa. Their pressure shift of the R_1 band in a natural sample up to ~5 GPa was -11.3 (±0.3) cm^{-1}/GPa in their study, in comparison to our value of -10.7 (±0.2) cm^{-1}/GPa.

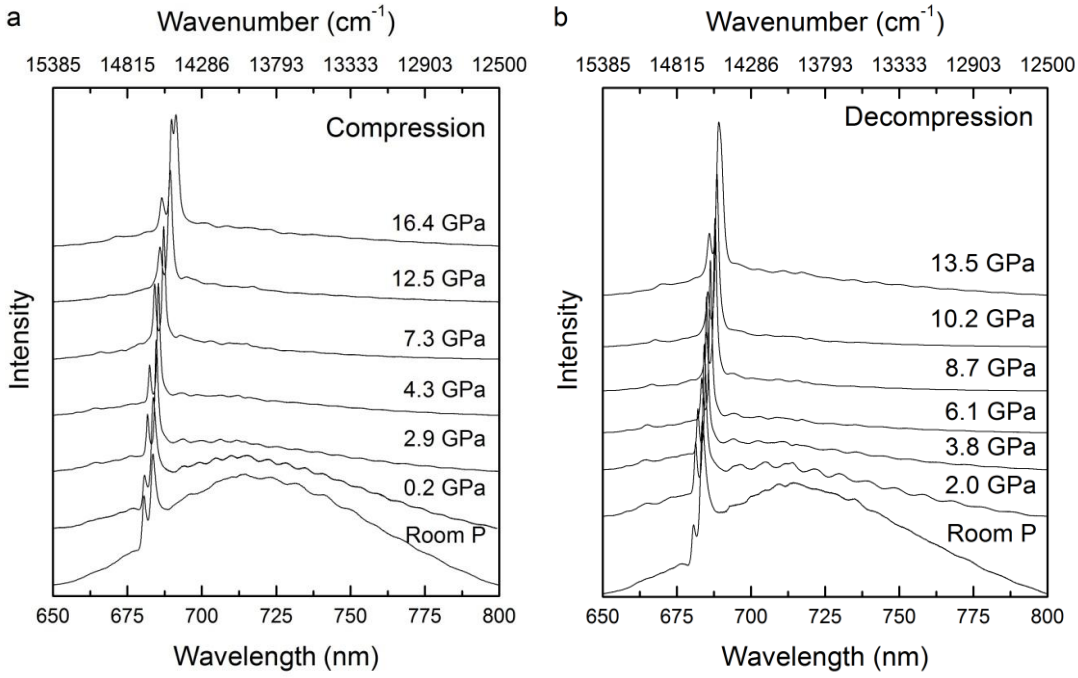

Figure 6.7. High-pressure luminescence spectra of emerald under 532 nm excitation (a) compression (b) decompression. Notably, the broad-band $^4T_2$ emission from Cr^{3+} and V^{2+} decreases in intensity rapidly under compression.

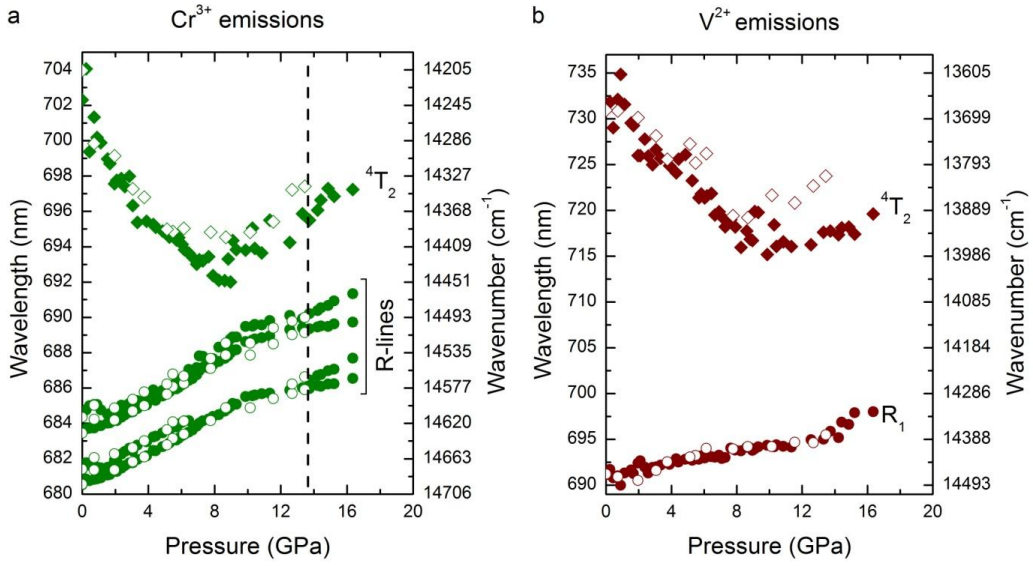

Figure 6.8. Pressure shift of emerald R-lines and $^4T_2$ bands of (a) Cr^{3+} and (b) V^{2+}. Primary and secondary R-lines are labeled with a p and s respectively. Vertical dashed line indicates the high-pressure phase transition. Closed symbols are

compression, open symbols are decompression, and error bars are smaller than the symbols.

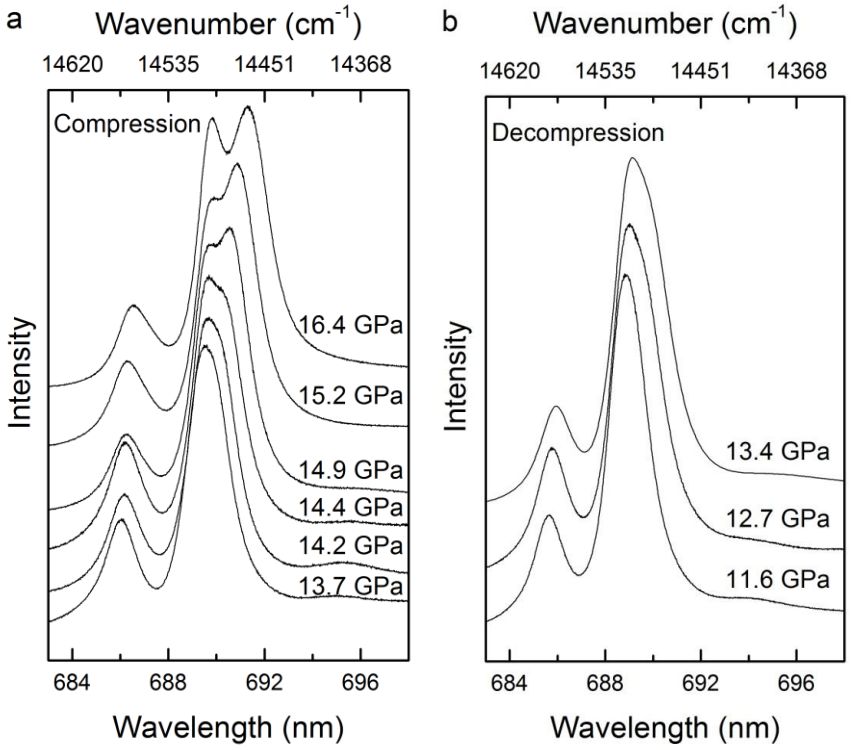

Figure 6.9. Detail of the Cr^{3+} R-line region showing the splitting that occurs in the high pressure phase of emerald on (a) compression and (b) decompression.

The pressure shift of the V^{2+} R-line in emerald is -6.5 (±0.3) cm^{-1}/GPa. There are few previous studies of the pressure shift of V^{2+} R-Lines. Chopelas and Nicol (1986) report that the pressure shift of the V^{2+} R_1 in MgO:V^{2+} is ~12 cm^{-1}/GPa and Jovanic et al. (2010) report that the pressure shift of V^{2+} R_1 in $LaMgAl_{11}O_{19}$:V^{2+} is essentially 0 cm^{-1}/GPa. In the case of MgO, the pressure shift of V^{2+} is roughly two times larger than that of Cr^{3+} in MgO (Chopelas and Nicol 1982). The opposite seems to be the case for V^{2+} in emerald (our observed V^{2+} R_1 pressure shift is about half of the Cr^{3+} R_1 pressure shift in emerald). One key difference between the MgO study and our study is that we are characterizing the pressure shift of Cr^{3+} and V^{2+}

simultaneously in the same material under compression. The unexpected smaller shift of the R-line of the larger V^{2+} ion may be associated with the effects of local charge balance on the environment surrounding this non-isovalent substitution: two V^{2+} substitutions are plausibly accompanied by an oxygen vacancy which, if the vacancy is local to the vanadium ion, may induce a markedly different local compressibility.

The $^4T_2$ transitions of Cr^{3+} and V^{2+} shift to higher energy up to ~8 GPa where their pressure shifts decrease, shifting only slightly to lower energy up to the maximum pressure of this study (Figure 6.8a and 6.8b). The intensities of these transitions also markedly decrease under compression. The shift to higher energy, and their decrease in intensity indicates that the crystal field strength changes from an intermediate strength field to a stronger field under compression to ~16.4 GPa. The shift of the $^4T_2$ emission to higher energies while the ^2E shifts to lower energies under compression has been reported in materials doped with d^3 ions (Jovanić et al. 2010). The change in crystal field strength appears to occur continuously and across the pressure range to ~10 GPa in emerald.

The $^4T_2$ transition corresponds to the difference in energy between the split *d* orbitals of the chromium ion, and is represented as 10Dq. If we assume, in accord with an octahedral crystal-field point-charge model, that the energy of the $^4T_2$ transition scales as $R^{-5}_{Cr\text{-}O}$ (Zheng 1995; Bray 2001), then we derive a compressibility of -4.67×10^{-4} GPa^{-1} for the Cr^{3+} sites. This result is substantially smaller than the calculated the compressibility of -9.36×10^{-3} GPa^{-1} for the Al-sites using the high-pressure single crystal results of Hazen and Finger (1986). The poor

performance of the point-charge model is likely associated with the local relaxation associated with Cr substitution for Al in emerald. Gaudry et al. (2007) find that the Cr-O bond lengths in emerald are almost 4% longer than the Al-O bond lengths: hence, the compaction undergone locally by the Cr-ion probably does not reflect the compression of the Al-site within the bulk lattice. We did not attempt the same calculation using the pressure shift of the $^4T_2$ emission of V^{2+}, since it is not isovalent with Al^{3+} and hence we expect simple crystal field scaling rules to break down even more severely than for isovalent substitutions. In addition to local relaxation, the roles of site distortion from an octahedral environment, pressure-induced shifts in site-geometry, potential complex deformation mechanisms, and spin-orbit coupling, as well as possible admixture between the $^4T_2$ and ^2E levels, further render such octahedral point charge-based scaling results suspect for emerald. In contrast to the ^2E emission, the pressure shift of the V^{2+} $^4T_2$ is more than twice the pressure shift of the Cr^{3+} $^4T_2$ emission in emerald, suggesting that sites with V^{2+} may be more compressible than Cr^{3+} sites in emerald.

The intensity of the Cr^{3+} and V^{2+} ^2E transitions increases under compression (Figure 6.10a) relative to the intensity of the Cr^{3+} and V^{2+} $^4T_2$ transitions (Figure 6.10b). Under compression, the energy of the $^4T_2$ transition shifts to higher energy and moves closer in energy to the ^2E transition. Indeed, by ~10 GPa, the $^4T_2$ emission of Cr^{3+} lies within 5 nm of the primary R_1 band. Hence, mixing between these two transitions is enhanced under compression. This increase in mixing and near-energetic equivalence likely contributes to the increase in intensity of the ^2E transition

under compression. It is also possible that the increase in relative intensity could be caused by the pressure shift of an absorption band relative to the wavelength of excitation: unfortunately, no optical absorption measurements of emerald have been conducted at high pressures, although significant shifts in emerald's crystal field absorptions are observed as a function of temperature (Parkin and Burns 1980; Taran et al. 1994). Above ~10 GPa, the relative intensity of the ^2E transition begins to decrease and the intensity of the $^4T_2$ increases slightly up to the maximum pressure of this study. This observation is unusual, and could be due to (1) a decrease in mixing between the $^4T_2$ and ^2E; (2) an unconstrained shift of an absorption band above 10 GPa; or (3) a significant change in the interaction between the two states across the high-pressure phase transition. By analogy with $Gd_3Sc_2Ga_3O_{12}:Cr^{3+}$ (Hoemmerich and Bray 1995), there could be a tendency towards anticrossing behavior of the $^4T_2$ and ^2E states in emerald under compression which starts to prevent mixing of the $^4T_2$ and ^2E near 10 GPa.. With respect to pressure shifts of Cr^{3+} absorption bands, a shift to shorter wavelength of ~100 nm under compression to ~13.5 GPa has been reported in kosmochlor ($NaCrSi_2O_6$) (Taran et al. 2011). If such a pressure shift is present in emerald, the shape of the emerald absorption spectrum (Taran et al. 1994) is such that under compression the absorption bands of emerald could shift so that 532 nm excitation is absorbed less by the low energy tail of the $^4T_1$ absorption, and more by the high energy side of the $^4T_2$ absorption. Lastly, the absorption spectrum of the high-pressure phase may be significantly different than that of the low pressure phase. However, we do not anticipate that two Cr-sites that have R_1 emission lines separated

by only ~33 cm^{-1} would generate a dramatically different absorption spectrum from the low-pressure phase.

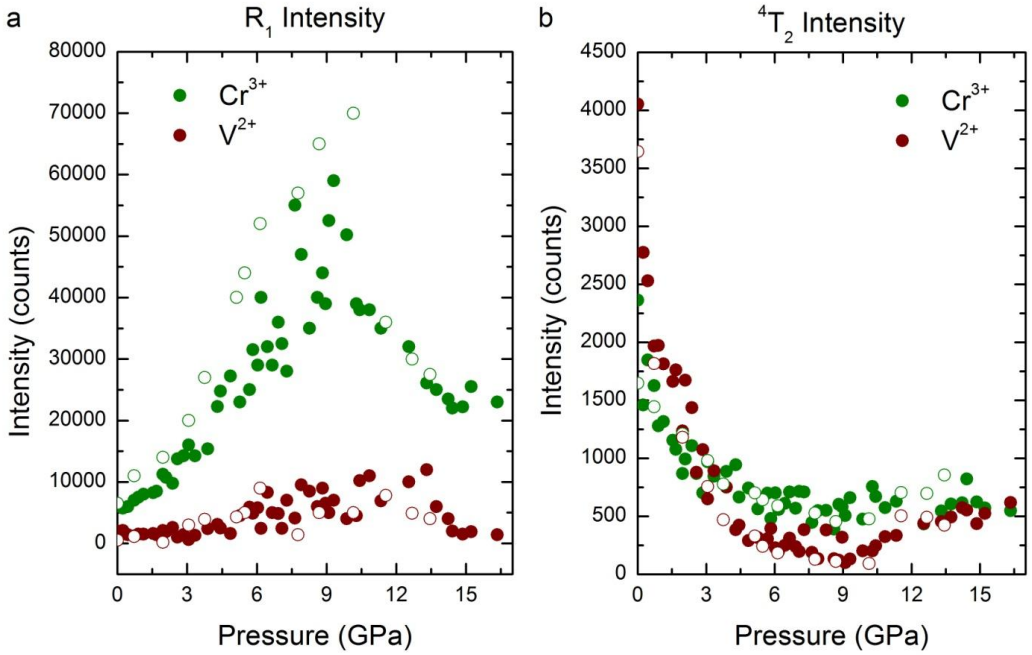

Figure 6.10. Pressure dependence of Cr^{3+} and V^{2+} (a) R_1 emission and (b) $^4T_2$ emission. R_1 intensity is normalized to the $^4T_2$ intensity and the $^4T_2$ intensity is normalized to the R_1 intensity. Closed symbols are compression, open symbols are decompression, and error bars are smaller than the symbols.

6.3.5 R-line splitting and FWHM

The R-line splitting is viewed as a primary manifestation of the distortion of the Al-site, with the larger the splitting, the more distorted that the Al-site is from an ideal octahedron. For example, ruby has a close-to-ideal Al-site (with a modest trigonal distortion) and has an R-line splitting of ~29 cm^{-1} (Syassen 2008), while zoisite ($Ca_2Al_3Si_3O_{12}(OH)$) has a highly distorted Al-site and has an R-line splitting of ~350 cm^{-1} (Koziarska et al. 1994). Emerald has a mildly distorted Al-site with an R-line splitting of ~65 cm^{-1}, and under compression to ~6.0 GPa the R-line splitting

decreases by ~5 cm^{-1}, indicating that the Al-site becomes less distorted (Figure 6.11a). Indeed, high-pressure single-crystal structural refinements confirm that the Al-sites become mildly less distorted up to ~5.7 GPa (Hazen et al. 1986). Above ~6.0 GPa the Cr^{3+} R-line splitting rapidly increases up to ~13.7 GPa, suggesting that the Al-sites become more distorted in this pressure interval as the high-pressure phase transition is approached. The R-line splitting of the secondary Cr^{3+} R-lines shows similar behavior under compression, but the data are more scattered because the second component of the R_2 line is difficult to deconvolve. Indeed, the secondary R_2 peak becomes impossible to resolve between ~6.5 GPa and 13.7 GPa. Also, only the R_1 component of the V^{2+} emission lines could be reliably fit across the pressure range of this study, and so the V^{2+} R-line splitting as a function of pressure was not characterized.

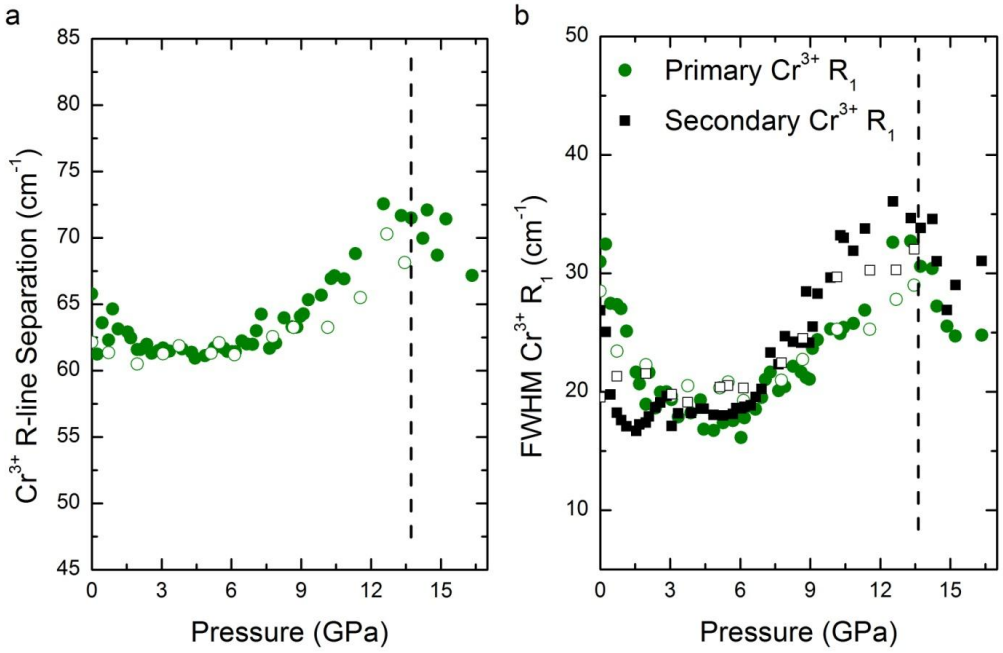

Figure 6.11. Pressure dependence up to ~16.4 GPa of the primary Cr^{3+} R-line components (a) R-line separation (b) FWHM circles (green) are R_1 and squares (black) are R_2. Vertical dashed line indicates the high-pressure phase transition. Closed symbols are compression, open symbols are decompression.

After the phase transition at ~13.7 GPa, a second component of the Cr^{3+} R_2 band again becomes resolvable, since the two components of each of the R-lines have different pressure shifts in the high-pressure phase. The pressure dependence of the Cr^{3+} R-line splitting changes sign and decreases above the 13.7 GPa transition (Figure 6.11a). This marked change in splitting indicates that the Al-sites in the high-pressure phase become less distorted under compression to the maximum pressure of this study. These variations in R-line separations are largely reversible on decompression, with the R-lines being perhaps slightly more closely separated between 13.7 GPa and ~10 GPa on decompression relative to on compression (Fig. 6.6a): we have no simple explanation for this difference.

The FWHMs of the primary and secondary Cr^{3+} R_1 bands as a function of pressure are shown in Figure 6.11b. The FWHM of the R_1 band decreases up to ~6.0 GPa, and from ~6.0 GPa to ~13.7 GPa phase transition, the FWHM of both the R_1 and R_2 bands increases. Above the transition, the FWHMs decrease up to the maximum pressure of 16.4 GPa. On decompression, the FWHMs of the R-lines generally follow the same trend as they did during compression, although the scatter is substantially greater, possibly due to the effects of residual strain following decompression. The Cr^{3+} R-line FWHM begins to increase at ~6.0 GPa, well below the pressure of the glass transition in methanol:ethanol mixtures (Piermarini et al. 1973; Klotz et al.

2009), and thus the broadening cannot be attributed to non-hydrostaticity. This trend of decreased splitting and FWHM above 13.7 GPa of the R-lines is thus robust: as such, the decreases in these parameters following the transition reflect a fundamental shift in the response to pressure of the Al/Cr site within the high-pressure phase.

The pressure-dependence of the FWHM of the V^{2+} R_1 line is challenging to resolve from our peak fits, and this peak may include diffcult-to-deconvolve components of the $^4T_2$ emission bands of both Cr^{3+} and V^{2+}. The room pressure and temperature FWHM of the V^{2+} R_1 that we determine from our deconvolution is ~200 cm^{-1}. This is extremely wide for a V^{2+} R_1 emission line (for example, the FWHM of the V^{2+} R_1 line in MgO is ~7 cm^{-1} at room pressure and temperature: Imbusch et al. 1964), and may reflect an association of this band with a vacancy, or a structurally distorted environment. The pressure-dependence of the linewidth of R-lines can be modeled using a Debye-based model (Kottke and Williams 1983), which is modified from the formulation for the temperature-dependence of the R-line widths (Imbusch et al. 1964). Since vibronic modes and neighbor lines could not be resolved across the pressure range of these measurements (due to the broad $^4T_2$ emission bands of both Cr^{3+} and V^{2+}), we do not know the rates at which vibronic modes shift, and whether they are anticipated to interact more or less strongly with the R-lines at high pressures. Moreover, our high-pressure Raman experiments provide the only experimental constraints on beryl's phonon spectrum under pressure. The vibronic modes that primarily couple with the R_1-lines to generate their width may initially shift at rates faster than the R-lines, which would generate the initial decrease in R-

line widths under compression to ~6.0 GPa. The decrease in peak widths above the transition may reflect either a structural effect (a more symmetric environment of the multiple Cr/Al sites within a different phase, and hence a smaller intrinsic peakwidth), or a shift in phonon coupling in the high-pressure phase, or a complementary combination of these two effects.

6.3.6 High-Pressure Phase Transition

Dramatic changes in the Raman spectra at ~14 GPa, a negative pressure shift of the E_{1g} mode, and splitting of the Cr^{3+} R-lines at ~13.7 GPa all indicate that beryl undergoes a phase transition to beryl-II near 14 GPa. The absence of hysteresis in both the Raman and luminescence spectra indicate that this transition is in second order in nature. This appears to be the first experimental evidence of the predicted 14 GPa soft-mode transition proposed by Prencipe et al. (2011). Our Raman data also confirm that this transition is a soft-mode transition (Figure 6.6a). Our spectroscopic data allow us to make some general comments on the high-pressure deformation of beryl up to and above the transition to beryl-II. Indeed, the detailed changes in the Si_6O_{18} ring and Al/Be polyhedra under compression were only characterized up to 5.7 GPa in single-crystal diffraction measurements by Hazen and Finger (1986).

Our Raman and luminescence data indicate that the crystal structure of beryl accommodates initial compression with little or no distortion of the Si_6O_{18} rings. Indeed, our high-pressure Raman and luminescence data (the pressure shift of emission lines, R-line splitting, and FWHM) suggest that the compaction mechanism of beryl involves primarily compression of the Al and Be sites up to ~6.0 GPa. Above

~6.0 GPa, the deformation mechanism may include compaction of the Si_6O_{18} rings, based on the changes observed in R-line splitting and FWHM of the Cr^{3+} R-lines. However, the deformation of the Si_6O_{18} rings above ~6.0 GPa is still likely minimal since no obvious changes in the Raman spectra are observed until above ~12 GPa. High-pressure single-crystal structure of beryl up show that the components of the rigid Si_6O_{18} rings do not significantly distort under compression, as indicated by the quadratic elongations (Robinson et al. 1971) of the Si-tetrahedra reported by Hazen and Finger (1986) which do not change up to ~5.7 GPa. This is in contrast to the quadratic elongation of the Al/Be sites reported by Hazen and Finger (1986). The increased distortion of the Al/Cr sites manifested by the shift near 6 GPa in the splitting and FWHM luminescence data indicate that the onset of larger degrees of distortion of the Al polyhedra may be associated with the initiation of deformation of the tetrahedra of the Si_6O_{18} rings (Fig. 6.1). The deformation of the rings above ~6.0 GPa likely includes mild distortions of the Si-tetrahedra (changes in bond angles or movement of the Si atom) but these changes do not generate a change in symmetry. Our luminescence data thus suggest that a change in the compressional mechanism of emerald occurs at ~6.0 GPa, with the Al-sites becoming increasingly distorted up to 13.7 GPa. Notably, quantum mechanical calculations on the compression of beryl up to 28.4 GPa show that the O2 atoms (which link the Al and Be sites) move away from the Si atoms and closer to the Al and Be atoms, while the O1 atoms, located on the inside of the Si_6O_{18} rings, move in the *ab* plane towards the center of the Si_6O_{18} rings (Figure 6.1; Prencipe and Nestola 2005).

At 13.7 GPa, the Cr^{3+} R_1 band becomes asymmetric (Figure 6.9), and a change in the pressure dependence of the V^{2+} R-line is observed (Fig. 6.8b). On increasing pressure above ~13.7 GPa, the Cr^{3+} R_1 line clearly splits into two components, and the Cr^{3+} R_2 line also becomes asymmetric. Dramatic changes in the trends of the FWHM as well as a splitting of the Cr^{3+} R-lines also occur at ~13.7 GPa (Fig. 6.11). Our Raman spectra show discontinuous shifts of all of the observed Raman modes as well as a dramatic decrease in intensity and FWHM of all observed Raman modes. Clearly, a phase transition that shifts the geometry and response to pressure of the Cr/Al site has taken place, as well as a change in the local bonding environment of the Si tetrahedra. This transition appears to be second order in nature, since no significant hysteresis of either the luminescent bands or Raman spectra is observed on decompression. The different pressure shifts of the two components of the Cr^{3+} R-lines in the high-pressure phase strongly suggests that there are two crystallographically distinct Al-sites with different responses to pressure in the high pressure phase. These observations of a phase transition near 13.7 GPa are in agreement with the proposed soft mode-associated high-pressure transition predicted by Prencipe et al. (2011). Our Raman data, with a strongly negative shift of a low-frequency band, are in full accord with this predicted soft-mode transition. The similarity of the decreases in R-line splitting and FWHM between 0 and 3 GPa, and above 13.7 GPa, suggests that the initial deformation mechanism of the Al-sites in the high pressure phase of emerald may be generally similar to that from room pressure to ~3.0 GPa. Hence, following the deformation of the Al-sites above ~6 GPa

accompanied by ring deformation, the combination of deformation of the components of the rings, and the evolution of two Al sites may allow for deformation to primarily be accommodated by the Al and Be sites. This deformation results in the Al-sites become more regular up to the maximum pressure of this study, as shown by the decreases in R-line separation and FWHM above ~13.7 GPa.

The hybrid Density Functional Theory (DFT) calculations of Prencipe et al. (2011) predict that a transition near 14 GPa from hexagonal to triclinic symmetry involves splitting the single Si site in hexagonal beryl to three Si sites in the high-pressure triclinic beryl. Our high-pressure Raman spectra do not evolve additional peaks in the high-pressure beryl-II spectra, although pervasive peak broadening is observed (Figure 6.5). Thus, the bonding environment of the three Si sites is likely similar in beryl-II.

The ring silicate cordierite ($(Mg,Fe)_2Al_4Si_5O_{18}$) shows potentially analogous behavior under compression: recent high-pressure single crystal structure determinations show that extensive deformation of cordierite's silicate rings occurs when orthorhombic cordierite transforms to triclinic cordierite at ~7.5 GPa (Miletich et al. 2014; Finkelstein et al. 2015). Rings become more oval shaped, and the Si sites not only split into multiple sites, but coordination changes in the octahedral and tetrahedral sites between the silicate rings may also occur. The changes occurring in emerald at ~13.7 GPa are not as dramatic as those that occur in cordierite. No changes in coordination of the Al-sites are observed: these would be expected to produce dramatic changes in the character of the Cr^{3+} luminescence. Changes in the

coordination of the Si sites are also not occurring in beryl-II. The notably different high-pressure behavior of these two ring silicates is thus likely related to the octahedrally coordinated Al in beryl being more stable under compression than the tetrahedrally coordinated Al in cordierite. Hence, the Si_6O_{18} ring of beryl is stable to higher pressures than the Si_6O_{18} ring of cordierite, and changes in coordination of Al, Si, or Be are not likely up to ~16.4 GPa. Hence, H_2O and other volatiles would remain stable inside the channels of beryl to higher pressures than in cordierite. It is also is clear that disordering does not take place in emerald to 16.4 GPa: in silicate glasses, R-lines are broadened, merged into one emission peak, shifted in wavelength, and the broad $^4T_2$ emission dominates the spectrum (Yamaga and Henderson 1991). Even in these disordered environments, Cr^{3+} strongly prefers octahedral coordination due to its high stabilization energy (Shinn and Tesar 1992). Thus, even in these extreme examples, Cr^{3+} emission occurs from a site that is six-fold coordinated, and the emission spectrum still has the characteristic features of Cr^{3+} in octahedral coordination. Hence, changes in coordination of the Al/Cr site and the Si site do not occur across the observed ~13.7 GPa phase transition in emerald.

6.4 Previous high-pressure powder diffraction

Two high-pressure powder diffraction studies have reached pressures in excess of ~14 GPa, and no high-pressure phase transitions have been reported (Qin et al. 2008; Fan et al. 2015). It is possible that, since the thermal expansion of different beryl compositions can depend strongly on their impurity content (Morosin 1972; Schlenker et al. 1977; Hochella and Brown 1986), minor compositional differences

may play a role in the high-pressure polymorphism of this material. However, the effect of a few thousand ppm of Cr and V would be far more likely to simply offset a phase transition to modestly higher (or lower) pressures. A more likely possibility is that the transition in beryl involves twinning (e.g., Prencipe et al. 2011) or a transition to a mildly modulated structure. A drop from hexagonal to triclinic symmetry would likely result in extensive twinning, and often in powder diffraction patterns this twinning may appear to resemble the higher symmetry lattice. Hence, without the correct twin law, these patterns could be refined within a hexagonal crystal system.

The refinement of incommensurately modulated structures from powder diffraction data is difficult, and usually single-crystal data are required to accurately determine the full symmetry of modulated phases. Also, overexposure techniques would need to be employed in order to properly resolve the intensities of satellite peaks. Satellite peaks can be missed if the assumption is made that no change from hexagonal symmetry occurs across the pressure range of the experiment. Limitations in angular access of typical diamond anvil cells may render detection of a transition to a modulated structure difficult to detect using standard Le Bail refinement techniques. Such modulated structures are precedented in ring silicates: cordierite undergoes a transition from orthorhombic to hexagonal at high-temperature (1450^{o}C) via a continuous mechanism that involves a metastable short-range-ordered modulated structure (Putnis and Bish 1983). Moreover, the E_{1g} mode at 138 cm^{-1} involves a dynamic wave-like distortion of the entire structure of beryl (again see animations on

the CRYSTAL web site[1]). It is likely that the soft mode transition *freezes* in this distortion, which could lead to a modulated structure.

6.5 Conclusions

High-pressure Raman and luminescence spectra have been collected for beryl and emerald up to a maximum pressure of ~16.4 GPa. Using both techniques we have characterized the high-pressure behavior of the Al, Be, and Si sites within beryl under compression and decompression. Our high-pressure Raman spectra show that an E_{1g} symmetry mode located at 133.6 cm^{-1} under ambient conditions shifts negatively under compression. Both our observations, and an extrapolation of this band's mode shift agrees well with the pressure shift of this soft mode calculated by Prencipe et al. (2011). Hence, our Raman data provide the first experimental evidence of the proposed soft-mode transition, and our luminescence data confirm that a modest structural change occurs near 14 GPa. Both sharp line and broad-band Cr^{3+} and V^{2+} luminescence are observed and characterized at both ambient and high-pressure conditions. The pressure shifts of Cr^{3+} and V^{2+} differ under compression, and this difference is likely related to the different valence states and local charge compensation associated with these two transition metal elements. The Al-sites likely undergo increasing distortion above ~6.0 GPa, as manifested by shifts in R-line splitting and FWHM near this pressure. Splitting of luminescent bands and changes in the sign of trends in FWHM are associated with a second order phase transition at ~13.7 GPa. Our Raman and luminescence results are in good agreement with the second order, soft-mode phase transition from *P*6/*mcc* to $P\bar{1}$ predicted by ab initio

calculations near ~14 GPa by Prencipe et al. (2011), and possibly observed by Merlini (based on a private communication quoted by Prencipe et al. (2011)): we designate the new phase beryl-II. The chemical composition (and particularly the level of Cr-substitution) is known to change the high-temperature behavior of beryl, but it does not appear that the level of Cr-substitution dramatically changes the high-pressure behavior of beryl, since the transition was observed at similar pressures in emerald (in luminescence) and beryl (in Raman spectra). Twinning may occur across this transition, and the transition might also be to a mildly modulated structure. The high-pressure phase of beryl might have interesting lasing properties, since Cr^{3+} is in a strong crystal field in the high-pressure phase. The intense Cr^{3+} R_1 emission line has two components separated by 1.60 nm (33.5 cm^{-1}) at ~16.4 GPa, and at higher pressures these bands likely become increasingly separated. Hence, these emission lines could be selectively excited across a modest wavelength range.

Chapter 7

A Cr^{3+} luminescence study of spodumene at high pressures: Effects of site geometry, a phase transition and a level-crossing

7.1 Introduction

Spodumene ($LiAlSi_2O_6$) is a lithium bearing pyroxene that crystallizes in the monoclinic crystal system with *C*2/*c* symmetry. Pyroxenes are major rock-forming minerals in the Earth's crust, and the upper mantle. While spodumene is certainly not abundant in the Earth's crust and upper mantle, understanding high-pressure phase transitions in *C*2/*c* pyroxenes is important for understanding the high-pressure behavior of mantle relevant pyroxenes (e.g. hedenbergite and diopside), and hence the structure of the upper mantle. High-pressure phase transitions in spodumene have been extensively studied (Arlt & Angel 2000; Pommier et al. 2003; Nestola et al. 2008; Ullrich et al. 2009). The first-order displacive *C*2/*c* to $P2_1/c$ phase transition in spodumene occurs at ~3.2 GPa and is generally well agreed upon (Figure 7.1). One study (Pommier et al. 2003) reports a possible higher pressure isosymmetric phase transition in the 7.7-10.5 GPa range based on shifts in the Raman spectra of this phase, and propose this phase transition is associated with a change in the lithium coordination number from five to six.

Arlt and Angel (2000) used single crystal x-ray diffraction and did not report a second phase transition in spodumene up to 8.8 GPa. They do suggest that a second phase transition is likely above 10 GPa based on the high-pressure kink value of the B chain (Figure 7.1). Similarly, Ullrich et al. (2009) performed both single crystal X-ray diffraction and Raman spectroscopy of spodumene up to ~9.24 GPa and concluded

that a second transition at 7.7 GPa is unlikely. Among closely related materials, a Raman and x-ray investigation of $LiFeSi_2O_6$ by Pommier et al. (2005) reported a C2/c to $P2_1/c$ phase transition between 0.7 and 1.0 GPa. They also suggest possible spin crossovers at ~6.0 GPa and propose that the disappearance of several peaks in the Raman spectrum (similar to the disappearance of peaks in the spodumene Raman spectra at high pressure) at ~8.0 GPa is evidence of a $P2_1/c$ to $P2_1/c$ phase transition. Nestola et al. (2008) used x-ray diffraction to examine $Li(Al_{0.53}Ga_{0.47})Si_2O_6$ and $LiGaSi_2O_6$ and found that the C2/c to $P2_1/c$ phase transition occurs between ~1.8 and 2.1 GPa in the mixed sample and between 0.0001 and 0.4 GPa in the Ga end-member. The mixed sample was studied up to ~9.0 GPa and the Ga end-member up to ~7.5 GPa and no higher pressure phase transitions were reported.

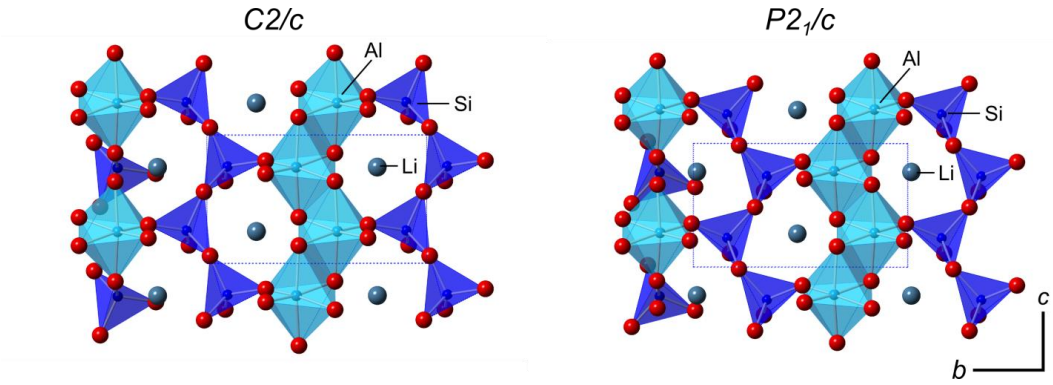

Figure 7.1. Structures of the spodumene C2/c and $P2_1/c$ phases (color online). Notably, the Al-atoms are off-center in their octahedral sites in both phases. The primary difference between these two phases is a distortion of the Li-site, which also leads to a difference in the kink of the B-chain of tetrahedra, Modified from Pommier et al. (2003); crystal structures from Arlt and Angel (2000).

We utilize the fluorescence of chromium to probe the response of spodumene to pressure: such fluorescence under pressure is well-characterized for ruby, whose

role as a pressure calibrant is well-known (e.g. Mao et al. 1986), but few other minerals have had the fluorescence of Cr^{3+} dopants examined under pressure (alexandrite, MgO, and $MgAl_2O_4$ are notable exceptions: Kottke and Williams 1983; Jahren et al. 1992; Chopelas 1996; Jovanić 2000). Notably, most other oxide minerals examined to date under pressure utilizing Cr^{3+} fluorescence have nearly ideal octahedral or only slightly distorted Cr-bearing sites. Spodumene's M1 site is, in comparison, substantially distorted (Clark et al. 1968; Arlt and Angel 2000). Hence, spodumene allows both the interrogation of the fluorescent response of Cr under pressure within a notably distorted site, and also through a phase transition at moderate pressures.

Characteristically, such fluorescence spectra show the strong and relatively sharp R-lines associated with the spin-forbidden ^2E-$^4A_2$ transition, with the $^4A_2$ state being the ground state and the ^2E state being split in non-cubic environments (Syassen 2008). At low crystal-field strengths, (e.g. Tanabe and Sugano 1954), the generally broader $^4T_2$-$^4A_2$ emission may dominate the emission spectrum; at intermediate field strengths, it may be present in the spectrum with the R-lines; and at high field strengths, the narrow band ^2E-$^4A_2$ emission dominates the fluorescence spectrum. In addition, vibronic bands are also observed: these phonon-associated sidebands are offset from the R-lines by the frequency of a coupled vibrational mode. Finally, comparatively sharp (and low amplitude in samples with dilute Cr^{3+} substitution) neighbor lines, generated by shared excitations between neighboring Cr^{3+} centers, are also observed: these bands tend to be complex, since a wide variety

of potential neighbor interactions exist. If their assignments are known, their pressure-dependence can be used to estimate changes in magnetic interactions between chromium centers (e.g. Williams and Jeanloz 1985).

Here, we use Cr^{3+} luminescence as a probe of the Al-site in spodumene under high-pressure. The luminescence spectra of the high pressure phase(s) of spodumene have not been previously reported. Thus, our experiments are oriented towards: (1) determining if luminescence spectra can elucidate high-pressure phase transitions in spodumene (in particular the proposed transition in the 7.7-10.5 GPa range); (2) characterize the luminescence spectra of the high pressure phases of spodumene; and (3) measure the pressure shift of the R-lines and sidebands.

7.2 Experimental Methods

Our sample was a natural light green gem quality spodumene from Minas Gerais, Brazil obtained from the UCSC mineral collection (#6744: colloquially, such a spodumene is often referred to as hiddenite). The sample is a single crystal with dimensions of ~3.0 x 2.0 x 0.5 cm and displays typical 90^o pyroxene cleavage. Sample purity was confirmed by Raman spectroscopy and luminescence spectroscopy, which were in excellent agreement with previous studies (Walker et al. 1997; Pommier et al. 2003). Chromium content was measured with a PhotonMachines Analyte 193H, which is a 193 nm ArF excimer laser system coupled with a ThermoScientific ElementXR single-collector magnetic sector ICP-MS. The instrument was calibrated with a SRM 610 trace element glass from NIST. The average chromium content was found to be 31.0 (±5.1) ppm.

High static pressures were generated using a Merrill-Bassett type diamond anvil cell (DAC) equipped with 16-sided type Ia 500 μm culet diamond anvils. A spring steel gasket with a 200 μm hole was used as the sample compartment. Experiments were carried out with methanol:ethanol:water 16:3:1 and methanol:ethanol 4:1 mixtures as the pressure media, which yield hydrostatic conditions up to the maximum pressure of this study (Piermarini et al. 1973; Fujishiro et al. 1982; Angel et al. 2007; Klotz et al. 2009). One single crystal of spodumene and one single crystal of ruby were loaded into the sample compartment for each experiment. Four experiments were conducted (three in 16:3:1 M:E:W and one in 4:1 M:E) and each experiment consisted of one compression and decompression cycle. Results of the different pressure media are indistinguishable from one another. The standard ruby fluorescence method (Mao et al. 1986) was used to determine the pressure.

For the low temperature measurements, the sample was immersed in liquid nitrogen. For the high-temperature measurements, the sample was heated using a modified DAC external heater previously described in Kraft et al. (1991). Temperatures in the high-temperature experiments were measured using a thermocouple attached directly to the sample with silver paint. This technique yields uncertainties of ±3.0 K.

Luminescence spectra were collected from 650-800 nm (15380-12500 cm^{-1}) with a Horiba LabRAM HR Evolution Raman spectrometer with a spectrometer focal length of 800 mm. Spectra were collected to a pressure of ~15 GPa and on

decompression at 298 K using an excitation wavelength of 532 nm. An Olympus BXFM-ILHS microscope with a 50x long working distance objective was used to focus the laser beam onto the sample. An 1800 lines/mm grating with a corresponding spectral resolution of ~1 cm^{-1} (or, equivalently, ~0.05 nm) was utilized. Combinations of Gaussian and Lorentzian functions were fit to the luminescence spectra with Horiba Labspec6 software.

7.3 Results and discussion

Representative luminescence spectra of spodumene on compression to ~15 GPa and on decompression to room pressure are shown in Figure 7.2. The pressure shifts of the R-lines and sidebands are plotted in Figure 7.3a & 7.3b. In the *C*2/*c* phase, two peaks are fit under each of the primary R_1 and R_2 bands. The more intense of each of the two fit components of the R_1 and R_2 bands lies on the lower wavelength side of the strong R-related peaks observed. The higher wavelength fit components of these peaks are smaller in amplitude and appear as shoulders/asymmetry on the high wavelength side of these bands (Fig. 7.3a).

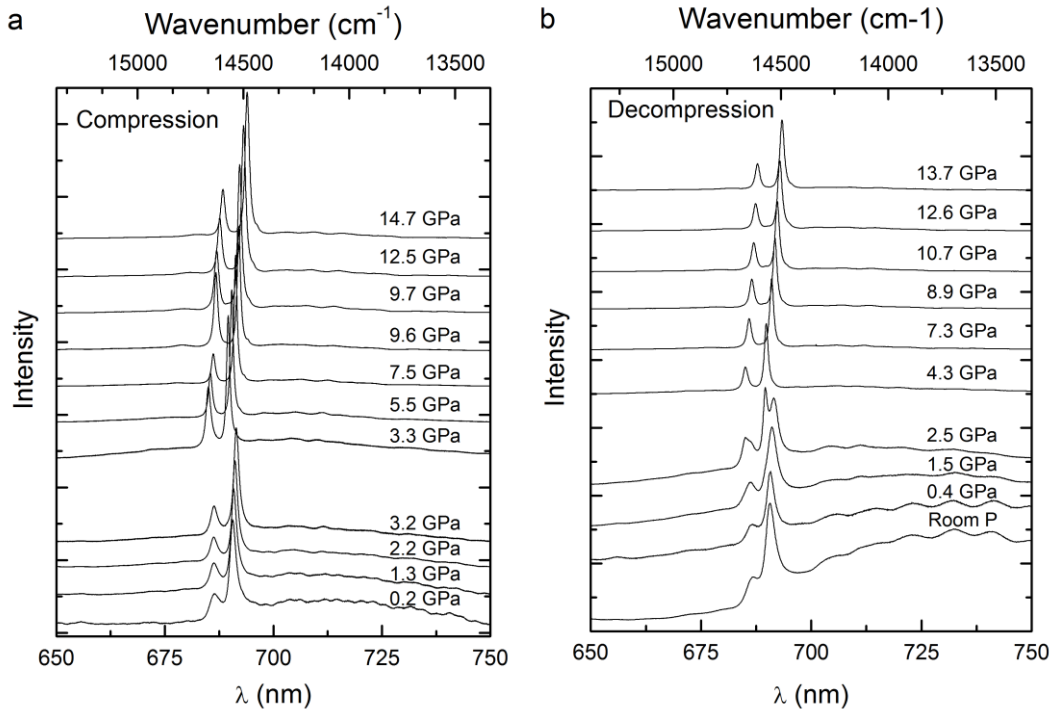

Figure 7.2. Representative luminescence spectra of spodumene on compression (a) to ~15 GPa and on decompression (b) to room pressure. The high-pressure phase transition produces a noticeable change in the luminescence spectra, and hysteresis of the phase transition is observed on decompression (most notably in the 2.5 GPa spectrum).

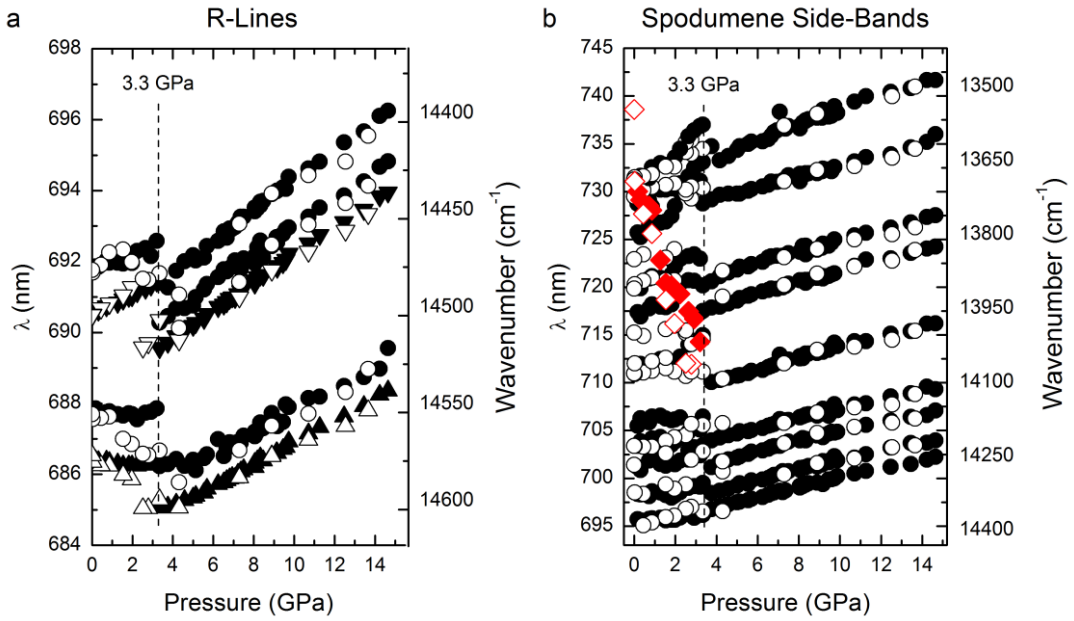

Figure 7.3. Pressure shift of the (a) R-lines (b) side-bands (color online). Note discontinuous shifts at ~3.2 indicating the *C*2/*c* to *P*2$_1$/*c* high pressure phase transition. Closed symbols are data on compression, and open symbols on decompression, and error bars are smaller than the symbols. The main R_1 band is shown by downward facing triangles and the main R_2 band by upward facing triangles. Diamond symbols (red in on-line version) represent the $^4T_2$ emission.

In the *P*2$_1$/*c* phase, three peaks are fit under the R_1 band, and two peaks are fit under R_2. These additional, low amplitude shoulders may be associated with either R-line emissions associated with chrome centers subject to modest lattice distortion accompanying the substitution of a nearby Cr^{3+} ion in the M1-octahedral chains, or be produced by a neighbor line that lies close to the R-line emissions. The latter interpretation plausibly explains the higher wavelength peak associated with the R_1 band in the high-pressure phase: this band becomes visible as the R-lines narrow through the phase transition. Figure 7.3 and Table 7.1 report the pressure shifts of the R-lines and sidebands in each polymorph of spodumene. Both components of the R_1

band shift positively in wavelength up to the 3.2 GPa transition, while both R_2 components shift slightly negatively in wavelength. Both R-lines shift positively in wavelength following the 3.2 GPa transition up to the maximum pressure of the study.

Assignment	λ (nm)	ν (cm^{-1})	Δν from R_1 (cm^{-1})	*dν/dP* (cm^{-1}/GPa)
R_2	686.3 (primary)	14570.2		1.4 (±0.3)
	687.9 (shoulder)	14537.6		0.6 (±0.4)
R_1	690.6 (primary)	14479.9		-5.2 (±0.2)
	691.8 (shoulder)	14454.4		-3.1 (±0.7)
N-Line	695.72	14373.6	106.3	-3.3 (±0.7)
N-Line	698.35	14319.3	160.6	-5.4 (±1.9)
	701.17	14261.9	218.0	-6.5 (±0.7)
	703.39	14216.9	263.0	3.9 (±2.7)
	705.51	14174.1	305.8	-3.8 (±2.9)
N/Vibronic?	711.40	14074.2	405.7	-18.3 (±3.5)
Vibronic	717.39	13955.5	524.4	-26.3 (±3.8)
Vibronic	720.29	13885.4	594.5	-21.9 (±2.7)
	725.73	13779.2	700.7	-37.5 (±3.4)
	728.72	13722.7	757.2	-25.2 (±2.6)
$^4T_2$-$^4A_2$	730.02	13626.4	853.5	+100.5 (±7.2)
	731.48	13670.9	809.0	-33.6 (±3.3)

Table 7.1. Assignment, wavelength and wavenumber of spectral features, offset of sidebands from R_1, and pressure shifts of R-lines, and sidebands which include both vibronic and N-lines (neighbor lines due to Cr-Cr pair emission) in both the *C*2/*c* and $P2_1/c$ phases. *not observed in the C2/c phase, reported wavelength and wavenumber are at ~3.2 GPa.

At 298K, sharp R-line emissions with an R_2 line at 686.54 nm (14565.8 cm^{-1}) and R_1 at 690.55 nm (14481.2 cm^{-1}), a broad $^4T_2$-$^4A_2$ transition at ~730.02 nm (13698.5 cm^{-1}), and phonon sidebands are observed (Figure 7.4). At 77 K, the R-lines shift to 685.14 nm (14595.6 cm^{-1}) for R_2, and 689.40 nm (14505.4 cm^{-1}) for R_1, and the intensity of the $^4T_2$-$^4A_2$ transition drops to unresolvable amplitude, implying that this transition is induced by thermal population of the $^4T_2$ state: this assignment and observation agrees well the ambient pressure spectra and interpretation of Walker et al. (1997). At 373 K, the R_2 band shifts to 686.83 nm (14559.6 cm^{-1}) and R_1 shifts to 691.41 nm (14463.2 cm^{-1}). Even with this modest temperature increase, notable broadening of the R-lines is observed (R_2 becomes a shoulder), and the intensity of the $^4T_2$ transition increases (relative to the R_1 band). This progressive thermally-activated marked growth of the $^4T_2$-$^4A_2$ transition and its coexistence with the R-lines indicate that the ^2E and $^4T_2$ states are reaching thermal equilibrium—a phenomenon observed in other oxides, such as ruby, emerald and topaz (e.g. Kisliuk and Moore 1967; Tarashchan et al. 2006). Moreover, that the energies of the ^2E and $^4T_2$ states lie close to one another indicates that the Cr site in spodumene is in an intermediate strength crystal field environment.

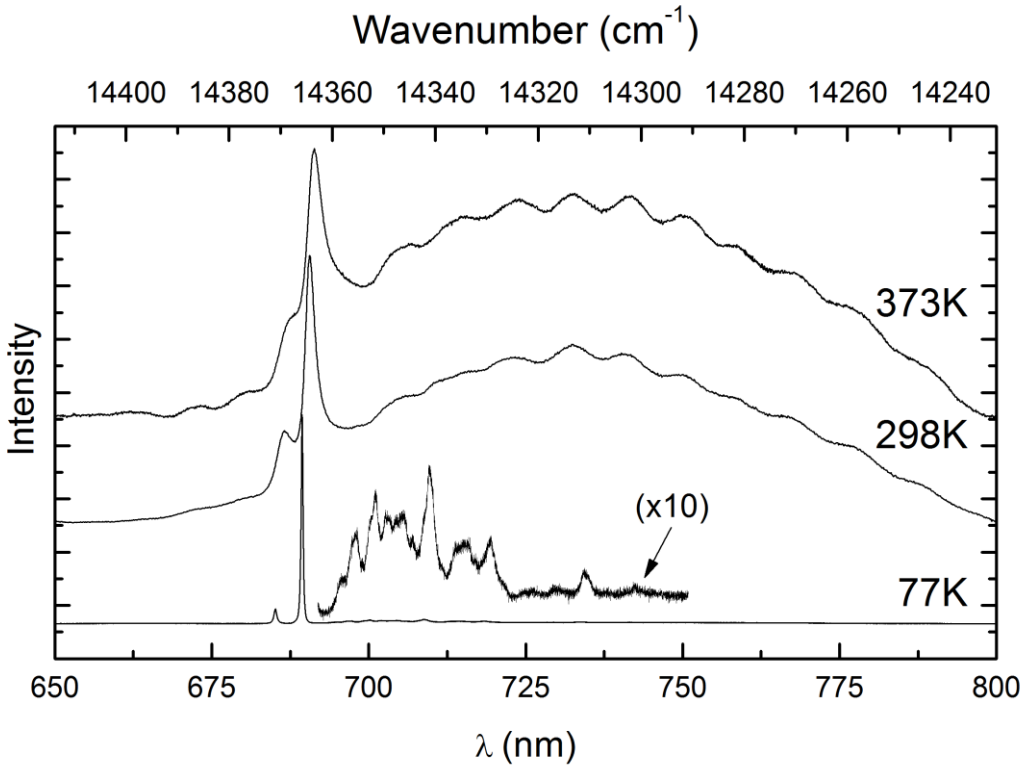

Figure 7.4. Representative luminescence emission spectra of spodumene at various temperatures. The R-lines broaden and shift to longer wavelength (lower energy) and the intensity of the broad $^4T_2$-$^4A_2$ transition (relative to R_1) increases as temperature increases. The low-amplitude sharp features in the 77 K spectra are attributed to neighbor lines, juxtaposed with broader vibronic lines.

Indeed, a similar, but more extreme, temperature dependence of Cr^{3+}-emission spectra has been observed in gadolinium scandium gallium garnet (GSGG). (Henderson et al. 1988) report that below 70K, the ^2E is the lowest excited state of the Cr^{3+} ion, while at 300K the $^4T_2$ level lies lower than the ^2E state by about 150 cm^{-1}. In this case, they propose that it is the thermal expansion that reduces the energy level splitting between ^2E and $^4T_2$ excited states. Comparable effects are observed in this system under compression, as well, as the $^4T_2$ emission is dramatically decreased under compression (Hommerich and Bray 1995). The two key aspects of these strong

temperature and pressure dependences of emission intensities that are relevant to spodumene are that: (1) the ^2E and $^4T_2$ states are strongly spin-orbit coupled, and admixed with one another, due to their close proximity; and (2) the relative amplitudes of emission from the ^2E and $^4T_2$ states varies as $\Delta[E(^4T_2)-E(^2E)]$ (Kisliuk and Moore 1967; Hommerich and Bray 1995). In this difference term, $E(^4T_2, ^2E)$ represent the respective energies of the two electronic states: when Δ is substantially greater than 0, sharp R-line fluorescence predominates and the system is strong field; weak field conditions occur when Δ is less than zero, producing broad-band $4T_2$-related emission.

Although the high temperature behavior of pyroxenes can be complex (e.g., kanoite ($MnMgSi_2O_6$) undergoes a $P2_1/c$ to $C2/c$ transition at ~240 ^oC: Arlt and Armbruster 1997), spodumene is known to remain in the $C2/c$ structure when heated to at least 760 ^oC (Cameron et al. 1973). Hence, high temperature phase transitions do not play a role in the high temperature luminescence behavior. Notably, the $^4T_2$ band's location at ~730.02 nm at room pressure and temperature is at substantially longer wavelength than the corresponding absorption of this transition near 628 nm (Khomenko and Platonov 1985). Thus, the excited state of this transition is Stokes shifted to the long wavelength side of the R-lines, a phenomenon that is well-documented in, for example, both emerald and ruby (Kisliuk and Moore 1967).

The $^4T_2$-$^4A_2$ emission intensity decreases in amplitude dramatically under compression, and shifts to higher frequency/lower wavelength rapidly (at ~100 cm^{-1}/GPa: Figure 7.5). Its broad emission is resolvable up to the ~3.2 GPa transition on

compression, but becomes difficult to resolve in the $P2_1/c$ phase. This transition corresponds to the difference in energy between the split *d* orbitals of the chromium ion, and is represented as 10Dq. If we assume, in accord with an octahedral crystal-field point-charge model, that this scales as $R^{-5}_{Cr\text{-}O}$ (e.g., Zheng, 1995; Bray, 2001), then we derive a contraction in the $R_{Cr\text{-}O}$ distance of ~0.5% at 3 GPa. This result is in gross accord with the ~0.7% decrease observed for the Al-O distances by Arlt and Angel (2000) between 0 and 3 GPa. However, the roles of site distortion/deviation from an octahedral environment, pressure-induced shifts in site-geometry (including changes in off-centeredness of ions within the site), and spin-orbit coupling and admixture between the $^4T_2$ and ^2E levels render such octahedral point charge-based scaling results suspect for spodumene.

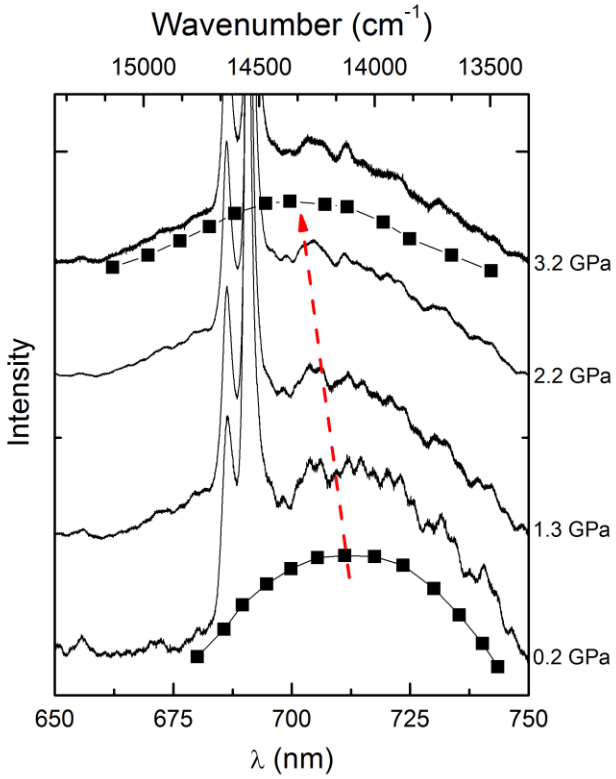

Figure 7.5. Fit of broad-band emission from the $^4T_2$ band as a function of pressure (color online). Note that it shifts to shorter wavelength (higher energy) and the intensity rapidly decreases as pressure increases dashed arrow (red in on-line version).

The decrease in intensity of the $^4T_2$-$^4A_2$ emission is clearly due to a transition in the crystal field strength from intermediate to strong, as manifested by the energetic cross-over of the $^4T_2$ and ^2E (Gaft et al. 2005 and Figure 7.6). Such a transition from predominantly broad-band to narrow-band fluorescence has been previously characterized in a number of Cr^{3+}-bearing materials under pressure, and particularly fluorides and gallium-based garnets (e.g. Dolan et al. 1986; de Viry et al. 1987; Freire et al. 1994; Hommerich and Bray 1995; Grinberg and Suchocki 2007; Sanz-Ortiz et al. 2010). This transition, in which spodumene starts in an intermediate crystal-field strength state (as indicated by both the close proximity of the $^4T_2$-$^4A_2$ and ^2E-$^4A_2$ emission peaks and the coexistence of their respective broad-band and narrow-band emissions), proceeds towards a strong-field strength state relatively rapidly under pressure. By 3 GPa, the markedly lower amplitude $^4T_2$ state has nearly crossed-over in energy with the ^2E state (Figures 7.5 and 7.6). We are unaware of any other reports of such a pressure-induced level cross-over in an oxide mineral, and these results illustrate the ability to, under appropriate circumstances, precisely locate the strength and pressure-dependence of crystal-field strength utilizing fluorescence spectra under pressure.

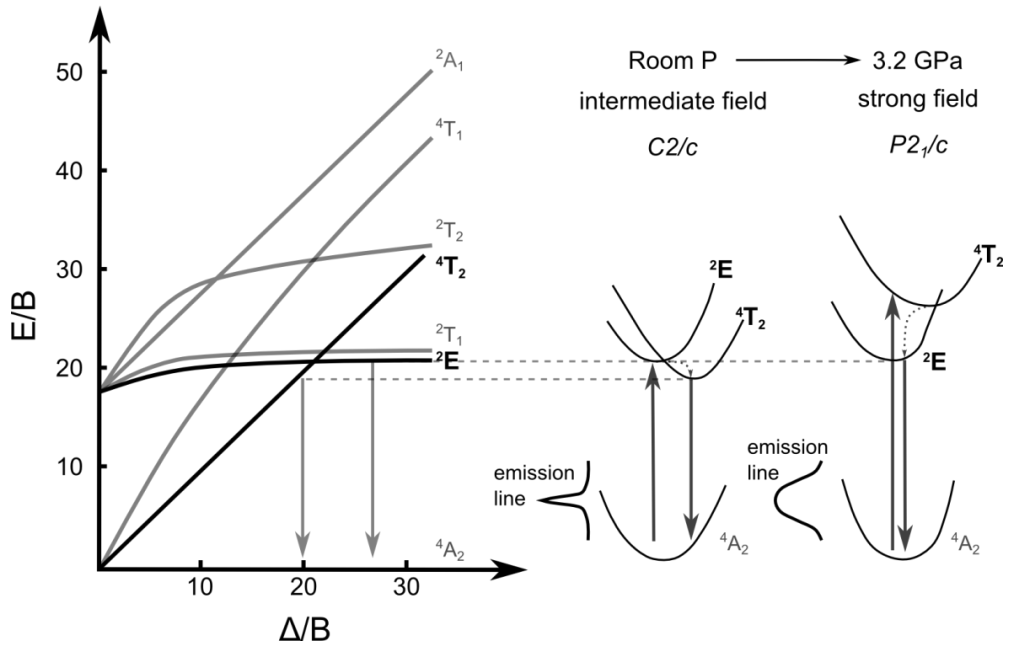

Figure 7.6. Tanabe-Sugano diagram for d^3 electron configuration of Cr^{3+} in octahedral symmetry showing the energy levels in weak and strong crystal fields. Cr^{3+} in spodumene is in a weak to intermediate strength field in the *C*2/*c* phase and in a strong crystal field in the $P2_1/c$ phase. Axes labels are incorporate the ligand field splitting parameter Δ (or 10 Dq), the Racah parameter B, and E is energy. Modified from Gaft et al. (2005) and Tanabe and Sugano (1954).

In the sideband region (Figure 7.3b), twelve bands can be resolved up to the ~3.2 GPa transition, and above the transition nine bands can be resolved up to the maximum pressure of this study. Within the *C*2/*c* phase, all the sidebands shift initially negatively in energy, with a decrease in the absolute values of their shifts starting at ~1.2 GPa, followed by a change in sign at ~2.2 GPa (Fig. 7.3b). These indications of non-linearities in some of the sideband mode shifts in the region below 3 GPa are likely associated with the migration of the $^4T_2$ state through this spectral region: complex Fano-type resonances have been observed to occur associated with the pressure-induced interaction of the $^4T_2$ state with lower-lying electronic states

(Sanz-Ortiz et al., 2010). At the phase transition at ~3.2 GPa, all of the sidebands shift discontinuously to shorter wavelength (higher energy). After the ~3.2 GPa transition, the sidebands shift positively in wavelength (to lower energy) and linearly up to ~15 GPa. On decompression, all sidebands show hysteresis across the ~3.2 GPa transition, providing additional confirmation that this transition is first-order in character (Arlt and Angel 2000; Ullrich et al. 2009).

7.4 3.2 GPa transition

Both components of the R-lines in the *C*2/*c* phase undergo discontinuous shifts (Figure 7.3a) to higher energy at ~3.2 GPa. The R_1 band shifts by -1.88 nm (+39 cm^{-1}) and R_2 shifts by -1.26 nm (+27 cm^{-1}). Arlt and Angel (2000) investigated this phase transition with single crystal X-ray diffraction and reported that the *a*- and *c*- unit cell parameters decrease in length while the *b*- unit cell parameter increases in length across this transition. The net result is a decrease in volume of the unit cell with an increase in the volume of the Al-octahedron. The shifts of the R-lines to higher energy, coupled with their negative pressure shifts, are consistent with this increase in volume of the Al-octahedron. Sidebands also undergo a similar discontinuous shift to higher energy (Figure 7.3b) across the transition. On decompression in the 3.2-2.0 GPa range, R-lines from both the $P2_1/c$ and *C*2/*c* spodumene phases are present in the spectra. This indicates that on decompression across the ~3.2 GPa transition, the low-pressure and high-pressure phases of spodumene coexist in closely juxtaposed sub-domains.

7.5 R-Line Separation and their FWHM

The R-line separation increases markedly as a function of pressure in the *C*2/*c* and $P2_1/c$ phase (Figure 7.7a). Room pressure single crystal x-ray diffraction data indicates that the Al-sites in spodumene are quite distorted (Clark et al. 1968; Cameron et al. 1973; Tribaudino et al. 2003). High pressure single crystal x-ray data indicates that the Al-octahedron may become slightly more distorted up to the 3.2 GPa transition (Arlt and Angel, 2000: Figure 7.7a, inset) and, after the transition, the Al-octahedra become substantially more distorted with pressure, as measured by the quadratic elongation of the octahedron (Robinson et al. 1971). Quadratic elongation is a measure of polyhedral distortion that is independent of the effective size of the polyhedra, and which closely correlates with polyhedral angle variance (Robinson et al. 1971). The splitting of the R-lines is generally viewed in (for example) ruby as being a consequence of the trigonal distortion in the aluminum site in Al_2O_3 (Syassen 2008). Thus, the dramatic increase in R-line separation with pressure in the low-pressure phase appears, given the modest (at best) increase in site distortion in this phase, to be anomalous. Refinements of the M1-site show, however, that the Al^{3+} ion in spodumene is substantially off-center within this site (Figure 7.1), and that the effect of pressure is to enhance this off-centered character via migration of the Al-ion along the *b*-axis of the structure (Arlt and Angel 2000). We anticipate that comparable off-centeredness, and a pressure-induced shift in off-centeredness, may accompany chromium substitution in this site. We therefore propose that the notable change in R-line splitting in the low-pressure phase is due to a pressure-induced shift in the off-centeredness of the chromium ion in this site.

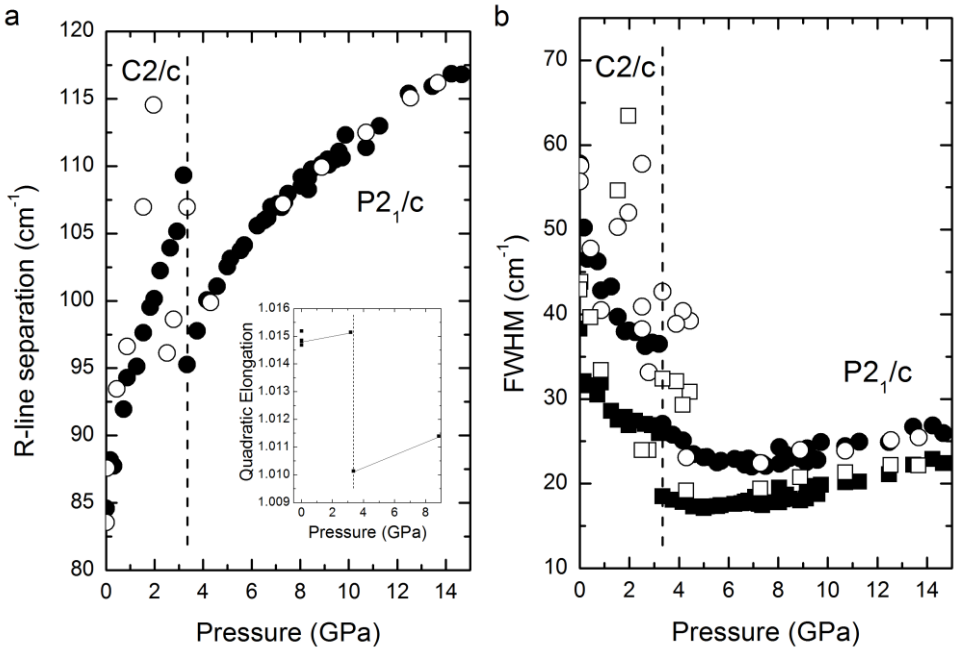

Figure 7.7. (a) R-line separation as a function of pressure. Inset shows the shift in quadratic elongation (Robinson et al., 1971) of the M1 site as a function of pressure, from Arlt and Angel (2000). (b) FWHM of R-lines as a function of pressure (R_2 circles, R_1 squares). Closed symbols are compression and open symbols are decompression, and error bars are smaller than the symbols. The scatter within the FWHM data on decompression in the low-pressure phase may be related to residual strain after the sample has been cycled through the phase transition.

Indeed, Taran et al. (2011) note, based on optical absorption spectra, that a substantial amount of local lattice relaxation appears to accompany Cr substitution into the M1 site of (particularly) Li-pyroxenes. Specifically, the relaxation parameter of chromium in spodumene, ε (Ardit et al. 2014), is defined as $((Cr\text{-}O)^{local}\text{-}(Al\text{-}O)/((Cr\text{-}O)^{endmember}\text{-}(Al\text{-}O))$, where $(Cr\text{-}O)^{local}$ is the bond length of dilute chromium substituents in spodumene as estimated from optical absorption spectra, and $(Cr\text{-}O)^{endmember}$ is that of $LiCrSi_2O_6$. Using data quoted in Taran et al. (2011) and the zero pressure Al-O distance for spodumene from Arlt and Angel (2000), the value of ε for

spodumene is indistinguishable from 1, implying that chromium substitution induces extensive local distortion: it substitutes in at an ionic radius of near 1.99 Å into a site for which the average M1 (Al-O) distance is 1.92 Å. Hence, local distortion is particularly large for Cr-substitution into spodumene, and the Cr^{3+} site itself may have anomalous distortions that are not captured by single-crystal diffraction experiments on spodumene. X-ray absorption experiments are likely required to fully characterize the nature and magnitude of these local distortions and off-centered character, but our luminescence data are most readily explained by a significant pressure dependence of the off-centeredness of chromium.

The FWHM (full width at half-maximum) as a function of pressure is shown in Figure 7.7b. The FWHM of the R-lines in *C*2/*c* phase decreases as pressure increases, and at the 3.2 GPa transition, the FWHM of both R-lines decreases. In the $P2_1/c$ phase, the FWHM of the R-lines initially decreases as pressure is increased up to ~6.0 GPa, and then increases slightly up to the maximum pressure of this study. On decompression, the FWHM of the R-lines follows generally the same trend as they did during compression, although the scatter is substantially greater, possibly due to the effects of residual strain following decompression. As Kottke and Williams (1983) describe, the pressure-dependence of the linewidth of R-lines can be modeled using a Debye-based model, modified from the temperature-dependence of linewidths proposed by Imbusch et al. (1964). The pressure shifts of the vibronic peaks are rapid, with migration rates away from the R-lines (Table 7.1) that are substantially in excess of the rate at which Raman-active modes in spodumene shift with pressure (Pommier

et al. 2003). Although the vibrations coupling with the electronic transition are expected to be of odd parity (Sangster and McCombie 1970), infrared-active vibrations are anticipated to have roughly comparable pressure shifts to the Raman vibrations. This increased separation with pressure implies that the coupling of phonons with the R-lines decreases with pressure over the pressure range of these measurements, which is consistent with our observations of narrowing linewidths under pressure. The underpinning reason for the rapid shifts of the vibronic lines is not entirely apparent. We speculate that the large volume of the Cr^{3+} ion within the M1 octahedral site and associated local distortions (and shifts in off-centeredness) may generate more rapid pressure shifts of vibrations associated with the Cr^{3+} site. This possibility implicitly suggests that the vibronic peaks in spodumene are associated with local vibrational modes rather than vibrational modes of the bulk lattice. This suggestion is in accord with simulations of coupling of vibrations with electronic transitions of isovalent substitutions in MgO (e.g., Sangster and McCombie, 1970).

7.6 Implications

The sensitivity of R-line luminescence to changes in the local bonding environment of the Al-site is clearly demonstrated by the discontinuous shift of the R-lines and sideband features at ~3.2 GPa. No discontinuous changes in the luminescence spectra from 3.2 GPa to ~15 GPa were observed, showing that a second phase transition in the ~7.7-10.5 GPa region is unlikely. We note that if the proposed ~7.7-10.5 GPa transition primarily involves subtle changes in the local bonding

environment of the M2 site (Li-site), and the M1 sites (Al-sites) remain more or less unchanged, this might not substantively change the character of the R-line luminescence. However, given the high sensitivity of R-line emission to subtle changes in Al-site volume, distortion, and/or electron density, a structural change that occurs absent a shift in R-line fluorescence seems unlikely . In summary, the clear discontinuity associated with the phase transition of spodumene within the R-line fluorescence, and the systematic and monotonic behavior of the R-lines and their sidebands at pressures above the transition, demonstrate both the sensitivity of R-lines to structural changes within the crystal, and the (possible meta-) stability of the $P2_1/c$ phase at 298 K to higher pressures than has previously been documented.

These measurements constrain the strength and pressure dependence of the crystal field strength in spodumene. We also demonstrate that pressure induced shifts in the off-centeredness of the chromium ion likely contribute to the increase in R-line splitting in the $C2/c$ phase (shifts in site distortion are not the sole consideration in generating R-line splitting). These observations illustrate the utility of Cr^{3+}-luminescence as a site specific probe in minerals, and specifically the value of high pressure luminescence measurements: even within a highly distorted octahedral site, such as the Al-site in spodumene, constraints on local bonding and crystal field strength can be generated. Finally, such luminescence measurements can expand the known stability (or metastability) range of complex crystalline phases of relevance to the upper mantle, such as the extension of the persistence of the $P2_1/c$ phase of spodumene at 298 K to ~15 GPa.

References

Akaogi, M., Kojitani, H., Yusa, H., Yamamoto, R., Kido, M., and Koyama, K. (2005) High-pressure transitions and thermochemistry of $MGeO_3$ (M=Mg, Zn and Sr) and Sr-silicates: Systematics in enthalpies of formation of A2+B4+O3 perovskites. Physics and Chemistry of Minerals, 32, 603–613.

Akizuri, M., Kuribayashi, T., Nagase, T., and Kitakaze, A. (2001) Triclinic liddicoatite and elbaite in growth sectors of tourmaline from Madagascar. American Mineralogist, 86, 364–369.

Alston, N.A., and West, J. (1928) The structure of topaz $[Al\ (F, OH)]_2SiO_4$. Proceedings of the Royal Society of London. Series A, Containing Papers of a Mathematical and Physical Charater, 358–367.

Anderson, P.W. (1959) New Approach to the Theory of Superexchange. Physical Review, 115.

Angel, R.J., Bujak, M., Zhao, J., Gatta, G.D., and Jacobsen, S.D. (2007) Effective hydrostatic limits of pressure media for high-pressure crystallographic studies. Journal of Applied Crystallography, 40, 26–32.

Angel, R.J., Gonzalez-Platas, J., and Alvaro, M. (2014) EosFit7c and a Fortran module (library) for equation of state calculations. Zeitschrift fur Kristallographie, 229, 405–419.

Ardit, M., Dondi, M., and Cruciani, G. (2014) On the structural relaxation around Cr^{3+} along binary solid solutions. European Journal of Mineralogy, 26, 359–370.

Arlt, T., and Angel, R.J. (2000) Displacive phase transitions in C-centred clinopyroxenes: spodumene, $LiScSi_2O_6$ and $ZnSiO_3$. Physics and Chemistry of Minerals, 27, 719–731.

Arlt, T., and Armbruster, T. (1997) The temperature-dependent $P2_1/c$-C_2/c phase transition in the clinopyroxene kanoite $MnMg[Si_2O_6]$: A single-crystal x-ray and optical study. Eur. J. MIneral., 9, 953–964.

Assefa, Z., Destefano, F., Lacasce, J.H., Ouellete, S., and Nagle, L.J.K. (1991) Photoluminescence and Electronic Structure of $TI[Au(CN)_2]$: Evidence for Relativistic Effects in Thallium-Gold and Gold-Gold Interactions. Inorg. Chem., 4, 2868–2876.

Assefa, Z., Shankle, G., Patterson, H.H., and Reynolds, R. (1994) Photoluminescence studies of lanthanide ion complexes of gold and silver dicyanides: a new low-dimensional solid state class for nonradiative excited-state energy transfer. Inorganic Chemistry, 33, 2187–2195.

Ballaran, T.B., and Angel, R.J. (2003) Equation of state and high-pressure phase transitions in lawsonite. European Journal of Mineralogy, 15, 241–246.

Baur, W.H. (1978) Crystal structure refinement of lawsonite. American Mineralogist, 63, 2–6.

Bebout, G., and Nakamura, E. (2003) Record in metamorphic tourmalines of subduction-zone devolatilization and boron cycling cycling Record in metamorphic tourmalines of subduction-zone devolatilization and boron cycling. Geology, 31, 407–410.

Beny, J.M., and Piriou, B. (1987) Vibrational Spectra of Single-Crystal Topaz. Physics and Chemistry of Minerals, 394, 148–154.

Birgeneau, R.J. (1969) Mechanisms of Energy Transport in Ruby. The Journal of Chemical Physics, 50, 4282.

Boehler, R., and De Hantsetters, K. (2004) New anvil designs in diamond-cells. High Pressure Research, 24, 391–396.

Bonnin, D., Calas, G., Suquet, H., and Pezerat, H. (1985) Sites occupancy of Fe^{3+} in Garfield nontronite: A spectroscopic study. Physics and Chemistry of Minerals, 12, 55–64.

Bradbury, S., and Williams, Q. (2003) Contrasting bonding behavior of two hydroxyl-bearing metamorphic minerals under pressure: Clinozoisite and topaz. American Mineralogist, 88, 1460–1470.

Bray, K.L. (2001) High Pressure Probes of Electronic Structure and Luminescence Properties of Transition Metal and Lanthanide Systems. In Topics in Current Chemistry Vol. 213, pp. 1–94.

Brown, I.D. (1976) On the Geometry of O-H...O Hydrogen Bonds. Acta Cryst, 32, 24–31.

——— (2002) The chemical bond in inorganic chemsitry, 278 p. Oxford University Press.

Buchert, J., Katz, A., and Alfano, R.R. (1983) Laser Action in Emerald. IEE Journal of Quantum Electronics, QE-19, 18–19.

Burnley, P.C., Green, H.W., and Prior, D.J. (1991) Faulting Associated with the Olivine to Spinel Transformation in Mg_2GeO_4 and its implications for Deep-focus Earthquakes. Journal of Geophysical Research, 96, 425–443.

Burns, R. (1993) Mineralogical applications of crystal field theory, 575 p.

Cameron, M., Sueno, S., Prewitt, C.T., and Papike, J.J. (1973) High-Temperature

crystal chemistry of acmite, diopside, hedenbergite, jadeite, spodumene, and Ureyite. American Mineralogist, 58, 594–618.

Chantel, J., Mookherjee, M., and Frost, D.J. (2012) The elasticity of lawsonite at high pressure and the origin of low velocity layers in subduction zones. Earth and Planetary Science Letters, 349–350, 116–125.

Chervin, J.C., Canny, B., and Mancinelli, M. (2001) Ruby-spheres as pressure gauge for optically transparent high pressure cells. High Pressure Research, 21, 305–314.

Chinnery, N., Pawley, A., and Clark, S. (2000) The equation of state of lawsonite to 7 GPa and 873 K, and calculation of its high pressure stability. American Mineralogist, 85, 1001–1008.

Chopelas, A. (1996) The fluorescence sideband method for obtaining acoustic velocities at high compressions: application to MgO and $MgAl_2O_4$. Physics and Chemistry of Minerals, 23, 25–37.

Chopelas, A., and Nicol, M. (1982) Pressure dependence to 100 kilobars of the phonons of MgO at 90 and 295 K. Journal of Geophysical Research, 87, 8591–8597.

Chopelas, A., and Serghiou, G. (2002) Spectroscopic evidence for pressure-induced phase transitions in diopside. Physics and Chemistry of Minerals, 29, 403–408.

Chu, S., Gibbs, H.M., and Passner, A. (1981) Single-ion-pair fluorescence ratios in ruby and Anderson localization. Physical Review B, 24.

Clark, J.R., Appleman, D.E., and Papike, J.J. (1968) Bonding in eight ordered clinopyroxenes isostructural with diopside. Contributions to Mineralogy and Petrology, 20, 81–85.

Comodi, P., and Zanazzi, P.F. (1996) Effects of temperature and pressure on the crystal structure of lawsonite. American Mineralogist, 81, 833–841.

Czaja, M. (2002) Luminescencja jonow chromu w naturalnych krzemionkach. Prace Naukowe Uniwersytetu Slaskiego w Katowicach.

Czaja, M., Kądziołka-Gaweł, M., Lisiecki, R., Bodył-Gajowska, S., and Mazurak, Z. (2014) Luminescence and other spectroscopic properties of purple and green Cr-clinochlore. Physics and Chemistry of Minerals, 41, 115–126.

Daniel, I.S., Fiquet, G.U., Gillet, P.H., Schmidt, M.A.X.W., Hanfland, M.I., and Villeurbanne, F.- (2000) High-pressure behaviour of lawsonite: a phase transition at 8.6 GPa. European Journal of Mineralogy, 12, 721–733.

de Viry, D., Denis, J.P., Tercier, N., and Blanzat, B. (1987) Effect of pressure on trivalent chromium photoluminescence in fluoride garnet $Na_3In_2Li_3F_{12}$. Solid State Communications, 63, 1183–1188.

Dexter, D.L. (1953) A Theory of Sensitized Luminescence in Solids. The Journal of Chemical Physics, 21, 836.

Dobrzhinetskaya, L.F., and Green, H.W. (2007) Experimental studies of mineralogical assemblages of metasedimentary rocks at Earth's mantle transition zone conditions. Journal of Metamorphic Geology, 25, 83–96.

Dolan, J.F., Kappers, L.A., and Bartram, R.H. (1986) Pressure and temperature dependence of chromium photoluminescence in $K_2NaGaF_6:Cr^{3+\cdot}$ Phys. Rev. B, 33, 7339–7341.

Domanik, K.J., and Holloway, J.R. (1996) The stability and composition of phengitic muscovite and associated phases from 5.5 to 11 GPa: Implications for deeply subducted sediments. Geochimica et Cosmochimica Acta, 60, 4133–4150.

Drillon, M., Panissod, P., Rabu, P., Souletie, J., Ksenofontov, V., and Gütlich, P. (2002) Pressure effect on the magnetism of layered copper(II) compounds with interlayer spacing up to 40.7 Å: Nature of the magnetic ordering. Physical Review B, 65, 1–8.

Eggert, J.H., Goettel, K.A., and Silvera, I.F. (1989) Ruby at high pressure. II. Fluorescence lifetime of the R line to 130 GPa. Physical Review B, 40, 5733–5738.

Fan, D., Xu, J., Kuang, Y., Li, X., Li, Y., and Xie, H. (2015) Compressibility and equation of state of beryl ($Be_3Al_2Si_6O_{18}$) by using a diamond anvil cell and in situ synchrotron X-ray diffraction. Physics and Chemistry of Minerals, 42, 529–539.

Faye, G.H. (1968) The Optical Absorption Spectra of Iron in Six-Coordinate Sites in Chiorite, Biotite, Phlogopite and Vivianite. Some Aspects of Pteochroism in the Sheet. Canadian Mineralogist, 9, 403–425.

Finkelstein, G.J., Dera, P.K., and Duffy, T.S. (2015) High-pressure phases of cordierite from single-crystal X-ray diffraction to 15 GPa. American Mineralogist, 100, 1821–1833.

Fonger, W., and Struck, C. (1975) Temperature dependences of Cr^{+3} radiative and nonradiative transitions in ruby and emerald. Physical Review B, 11, 3251–3260.

Freire, P.T.C., Pilla, O., and Lemos, V. (1994) Pressure-induced level crossing in $KZnF_2:Cr^{3+}$. Physical Review B, 49, 9232–9235.

Frondel, C. (1948) Tourmaline pressure gauges. American Mineralogist, 33, 1–17.

Fujimoto, Y., Kono, Y., Hirajima, T., Kanagawa, K., Ishikawa, M., Arima, M., Suetsugu, D., Bina, C., Inoue, T., Wiens, D., and others (2010) P-wave velocity and anisotropy of lawsonite and epidote blueschists: Constraints on water transportation along subducting oceanic crust. Physics of the Earth and Planetary Interiors, 183, 219–228.

Fujishiro, I., Piermarini, G.J., Block, S., and Munro, R.G. (1982) Viscosities and glass transition pressures in the methanol-ethanol-water system. High Pressure Research in Science and Industry: Proceedings of the 8th AIRAPT Conference, 2, 608–611.

Gaft, M., Nagli, L., Reisfeld, R., Panczer, G., and Brestel, M. (2003) Time-resolved luminescence of Cr^{3+} in topaz $Al_2SiO_4(OH,F)_2$. Journal of Luminescence, 103, 349–356.

Gaft, M., Reisfeld, R., and Panczer, G. (2005) Modern Luminescence Spectroscopy of Minerals and Materials, 356 p. Springer.

Gasharova, B., Mihailova, B., and Konstantinov, L. (1997) Raman spectra of various types of tourmaline. Eur. J. Mineral, 9, 935–940.

Gatta, G.D., Nestola, F., and Ballaran, T.B. (2006) Elastic behaviour and structural evolution of topaz at high pressure. Physics and Chemistry of Minerals, 33, 235–242.

Gatta, G.D., Morgenroth, W., Dera, P., Petitgirard, S., and Liermann, H.-P. (2014) Elastic behavior and pressure-induced structure evolution of topaz up to 45 GPa. Physics and Chemistry of Minerals, 41, 569–577.

Gibbs, G., Breck, D., and Meagher, E. (1968) Structural refinement of hydrous and anhydrous synthetic beryl and emerald. Lithos, 1, 275–285.

Goodenough, J.B. (1960) Direct Cation- -Cation Interactions in Several Oxides*. Physical Review, 117, 1442–1451.

Grevel, K., and Nowlan, E. (2000) In situ X-ray diffraction investigation of lawsonite and zoisite at high pressures and temperatures. American Mineralogist, 85, 206–216.

Grinberg, M., and Suchocki, A. (2007) Pressure-induced changes in the energetic structure of the 3d3 ions in solid matrices. Journal of Luminescence, 125, 97–103.

Hagemann, H., Lucken, A., Bill, H., Gysler-Sanz, J., and Stalder, H.A. (1990) Polarized Raman spectra of beryl and bazzite. Physics and Chemistry of

Minerals, 17, 395–401.

Hamburger, G.E., and Buerger, M.J. (1948) The Structure of Tourmaline. American Mineralogist, 33, 532–540.

Hawthorne, F.C., and Henry, D.J. (1999) Classification of the minerals of the tourmaline group. European Journal of Mineralogy, 11, 201–216.

Hawthorne, F.C., Macdonald, D.J., and Burns, P.C. (1993) Reassignment of cation site occupancies in tourmaline: Al-Mg disorder in the crystal structure of dravite. American Mineralogist, 78, 265–270.

Hazen, R.M., and Finger, L.W. (1983) High-pressure and high-temperature crystallographic study of the gillespite I-II phase transition. American Mineralogist, 68, 595–603.

Hazen, R.M., Au, A.Y., and Finger, W. (1986) High-pressure crystal chemistry of beryl (Be3Al2Si6O18) and euclase ($BeAlSiO_4OH$). American Mineralogist, 71, 977–984.

Hemingway, B.S., Barton, M.D., Robie, R.A., and Haselton, H.T. (1986) Heat capacities and thermodynamic functions for beryl, $Be_3Al_2Si_6O_{18}$, phenakite, Be_2SiO_4, euclase, $BeAlSiO_4(OH)$, bertrandite, $Be_4Si_2O_7(OH)_2$, and chrysoberyl, $BeAl_2O_4$. American Mineralogist, 71, 557–568.

Henderson, B., Marshall, A., Yamagatf, M., Donnellt, K.P.O., and Cockayneo, B. (1988) The temperature dependence of Cr^{3+} photoluminescence in some garnet crystals. Journal of Physics C: Solid State Physics, 21, 6187–6198.

Henry, D.J., Novák, M., Hawthorne, F.C., Ertl, A., Dutrow, B.L., Uher, P., and Pezzotta, F. (2011) Nomenclature of the tourmaline-supergroup minerals. American Mineralogist, 96, 895–913.

Hettiarachchi, S.R., Rawashdeh-omary, M.A., Kanan, S.M., Omary, M.A., Patterson, H.H., and Tripp, C.P. (2002) Spectroscopic Studies of " Exciplex Tuning " for Dicyanoaurate (I) Ions Doped in Potassium Chloride Crystals. J. Phys. Chem. B, 10058–10064.

Hirschmann, M.M. (2006) Water, melting, and the deep Earth H_2O cycle. Annual Review of Earth and Planetary Sciences, 34, 629–653.

Hochella, M.F., and Brown, G.E. (1986) Structural Mechanisms of Anomalous Thermal Expansion of Cordierite-Beryl and Other Framework Silicates. Journal of the American Ceramic Society, 69, 13–18.

Hoemmerich, U., and Bray, K.L. (1995) Direct observation of anticrossing behaviour in a luminescent Cr^{3+} - doped system. Physical Review B, 51, 8595–8598.

Hofmeister, A.M., Hoering, T.C., and Virgo, D. (1987) Vibrational spectroscopy of beryllium aluminosilicates: Heat capacity calculations from band assignments. Physics and Chemistry of Minerals, 14, 205–224.

Holland, T., Redfern, S., and Pawley, A. (1996) Volume behavior of hydrous minerals at high pressure and temperature: II. Compressibilities of lawsonite, zoisite, clinozoisite, and epidote. American Mineralogist, 81, 335–340.

Hommerich, U., and Bray, K.L. (1995) High-pressure lase spectroscopy of Cr^{3+}:$Gd_3Sc_2GaO_{12}$ and Cr^{3+}:$Gd_3Ga_5O_{12}$. Physical Review B, 51, 12133–12141.

Hua, H., Mirov, S., and Vohra, Y. (1996) High-pressure and high-temperature studies on oxide garnets. Physical Review B, 54, 6200–6209.

Hübschle, C.B., Sheldrick, G.M., and Dittrich, B. (2011) ShelXle: A Qt graphical user interface for SHELXL. Journal of Applied Crystallography, 44, 1281–1284.

Hughes, J.M., Ertl, A., Dyar, M.D., Grew, E.S., Shearer, C.K., Yates, M.G., and Guidotti, C. V. (2000) Tetrahedrally coordinated boron in a tourmaline: Boron-rich olenite from Stoffhutte, Koralpe, Austria. Canadian Mineralogist, 38, 861–868.

Imbusch, G.F. (1967) Energy transfer in ruby. Physical Review, 153, 326–337.

Imbusch, G.F., Yen, W.M., Schawlow, A.L., McCumber, D.E., and Sturge, M.D. (1964) Temperature dependence of the width and position of the ^2E $^4A_2$ fluorescence lines of Cr^{3+} and V^{2+} in MgO. Physical Review, 133.

Incel, S., Nadege, H., Labrousse, L., Deldicque, D., Ferrand, T., Wang, Y., Renner, J., Morales, L., and Schubnel, A. (2017) Laboratory earthquakes triggered during eclogitization of lawsonite bearing blueschist. Earth and Planetary Science Letters, 459, 320–331.

Ito, T., and Sadanaga, R. (1951) A Fourier analysis of the structure of tourmaline. Acta Crystallographica, 4, 385–390.

Jahren, A.H., Kruger, M.B., and Jeanloz, R. (1992) Alexandrite as a high-temperature pressure calibrant, and implications for the ruby-fluorescence scale. Journal of Applied Physics, 71, 1579–1582.

Jessop, P.E., and Szabo, A. (1980) Resonant optical energy transfer in ruby. Physical Review Letters, 45, 1712–1715.

John, T., Scambelluri, M., Frische, M., Barnes, J.D., and Bach, W. (2011) Dehydration of subducting serpentinite: Implications for halogen mobility in subduction zones and the deep halogen cycle. Earth and Planetary Science Letters, 308, 65–76.

Jovanić, B.R. (1997) High pressure and fluorescence lifetime of the ^{2}E level in MgO: Cr^{3+}. Physica Scripta, 56, 477–479.

——— (2000) Effect of High Pressure on Fluorescence Lifetime and Position for R_1 Line in Synthetic Spinel MgAl2O4:Cr3+. Materials Science Forum, 352, 247–250.

Jovanić, B.R., Viana, B., Radenkovic, B., Despotovic, M., and Panic, B. (2010) High-pressure optical studies of LMA:V^{2+}. Materials Chemistry and Physics, 124, 109–112.

Kamińska, A., Suchocki, A., Kobyakov, S., Arizmendi, L., Potemski, M., and Teran, F.J. (2007) High-pressure and magneto-optical studies of Cr-related defects in the lithium-rich $LiNbO_3$:Cr,Mg crystal. Physical Review B, 76, 144117.

Kantor, I., Prakapenka, V., Kantor, A., Dera, P., Kurnosov, A., Sinogeikin, S., Dubrovinskaia, N., and Dubrovinsky, L. (2012) BX90: A new diamond anvil cell design for X-ray diffraction and optical measurements. Review of Scientific Instruments, 83.

Karickhoff, S.W., and Bailey, G.W. (1973) Optical absorption spectra of clay minerals. Clays and Clay Minerals, 21, 51–57.

Kendrick, M.A., Jackson, M.G., Hauri, E.H., and Phillips, D. (2015) The halogen (F, Cl, Br, I) and H2O systematics of Samoan lavas: Assimilated-seawater, EM2 and high-3He/4He components. Earth and Planetary Science Letters, 410, 197–209.

Khomenko, V., and Platonov, A. (1985) Electronic absorption spectra of Cr^{3+} ions in natural clinopyroxenes. Physics and Chemistry of Minerals, 11, 261–265.

Kisliuk, P., and Moore, C.A. (1967) Radiation from the 4T2 State of Cr3+ in Ruby and Emerald. Physical Review, 160, 307–312.

Kisliuk, P., Chang, N.C., Scott, P.L., and Pryce, M.H.L. (1969) Energy levels of chromium ion pairs in ruby. Physical Review, 184, 367–374.

Kleppe, A., Jephcoat, A., and Welch, M. (2003) The effect of pressure upon hydrogen bonding in chlorite: a Raman spectroscopic study of clinochlore to 26.5 GPa. American Mineralogist, 88, 567–573.

Klotz, S., Chervin, J.-C., Munsch, P., and Le Marchand, G. (2009) Hydrostatic limits of 11 pressure transmitting media. Journal of Physics D: Applied Physics, 42, 75413.

Kolesov, B.A., Lager, G.A., and Schultz, A.J. (2008) Behaviour of H_2O and OH in lawsonite: a single-crystal neutron diffraction and Raman spectroscopic

investigation. European Journal of Mineralogy, 63–72.

Komatsu, K. (2005) Pressure dependence of the OH-stretching mode in F-rich natural topaz and topaz-OH. American Mineralogist, 90, 266–270.

Komatsu, K., Kuribayashi, T., and Kudoh, Y. (2003) Effect of temperature and pressure on the crystal structure of topaz, $Al_2SiO_4(OH,F)_2$. Journal of Mineralogical and Petrological Sciences, 167–180.

Kottke, T., and Williams, F. (1983) Pressure dependence of the alexandrite emission spectrum. Physical Review B, 28, 1923–1927.

Koziarska, B., Godlewski, M., Suchocki, A., Czaja, M., and Mazurak, Z. (1994) Optical properties of zoisite. Physical Review B, 50, 297–300.

Kraft, S., Knittle, E., and Williams, Q. (1991) Carbonate Stability in the Earth's Mantle: A Vibrational Spectroscopic Study of Aragonite and Dolomite at High Pressures and Temperatures. Journal of Geophysical Research, 96, 17997–18009.

Krosse, S. (1995) Hochdrucksynthese, stabilitat und eigenschaften der borsilikate dravit und kornerupin sowie darstellung und stabilitatsverhalten eines neuen Mg-Al-borates.

Kunz, M., and Brown, I.D. (1995) Out-of-Center Distortions around Octahedrally Coordinated d^0 Transition Metals. Journal of Solid State Chemistry.

Kunz, M., Lager, G.A., Bürgi, H.B., and Fernandez-Diaz, M.T. (2006) High-temperature single-crystal neutron diffraction study of natural chondrodite. Physics and Chemistry of Minerals, 33, 17–27.

Lacasce, J.H., Turner, W.A., Corson, M.R., Dolan, P.J., and Nagle, J.K. (1987) Magnetic field effects on the luminescence of $Cs[Au(CN)_2]$ at low temperatures. Chemical Physics, 118, 289–294.

Lai, S.T. (1987) Highly efficient emerald laser. Journal of the Optical Society of America B, 4, 1286–1290.

Laurance, N., McIrvine, E.C., and Lambe, J. (1962) Aluminum Hyperfine Interactions in Ruby. Journal of Physics and Chemistry of Solids, 23, 515–531.

Leger, J.M., Haines, J., and Atouf, A. (1996) The high pressure behaviour of the cotunnite and post-cotunnite phases of $PbCl_2$ and $SnCl_2$. Journal of Physics and Chemistry of Solids, 57, 7–16.

Lehmann, G., and Harder, H. (1970) Optical Spectra of Di- and Trivalent Iron in Corundum. American Mineralogist, 55, 98–105.

Li, H., Qin, S., Zhu, X., Liu, J., Li, X., Wu, X., and Wu, Z. (2004) In situ high-pressure X-ray diffraction of natural tourmaline. Nuclear Tech, 27, 919–922.

Libowitzky, E. (2009) Comment on "'Behaviour of H_2O and OH in lawsonite : a single-crystal neutron diffraction and Raman spectroscopic investigation'" by B.A. Kolesov et al. European Journal of Mineralogy, 21, 915–918.

Libowitzky, E., and Armbruster, T. (1995) Low-temperature phase transitions and the role of hydrogen bonds in lawsonite. American Mineralogist, 80, 1277–1285.

Liebscher, A., Dörsam, G., Franz, G., Wunder, B., and Gottschalk, M. (2010) Crystal chemistry of synthetic lawsonite solid-solution series $CaAl_2[(OH)_2/Si_2O_7]\cdot H2O$-$SrAl2[(OH)_2/Si_2O_7]\cdot H_2O$ and the *Cmcm*-$P2_1/m$ phase transition. American Mineralogist, 95, 724–735.

Likhacheva, A.Y., Goryainov, S. V., Krylov, A.S., Bul'Bak, T.A., and Prasad, P.S.R. (2012) Raman spectroscopy of natural cordierite at high water pressure up to 5 GPa. Journal of Raman Spectroscopy, 43, 559–563.

Lyo, S.K. (1971) Critical Concentration for Single-Ion-Single-Ion Energy Transfer in Ruby. Physical Review B, 3, 3331–3341.

MacCraith, B.D., Glynn, T.J., Imbusch, G.F., Remeika, J.P., and Wood, D.L. (1982) Exchange interaction in nearest-neighbor Cr^{3+} ion pairs in $LiGa_5O_8$:Cr^{3+}. Physical Review B, 25, 3572–3575.

Maiman, T.H. (1960) Stimulated Optical Radiation in Ruby. Nature, 187, 493–494.

Mao, H.K., Xu, J.A., and Bell, P.M. (1986) Calibration of the Ruby Pressure Gauge to 800 kbar Under Quasi-Hydrostatic Conditions. Journal of Geophysical Research, 91, 4673–4676.

Marschall, H.R., Altherr, R., and Rüpke, L. (2007) Squeezing out the slab - modelling the release of Li, Be and B during progressive high-pressure metamorphism. Chemical Geology, 239, 323–335.

McCarthy, P.J., and Gudel, H.U. (1988) Optical spectroscopy of exchange-coupled transition metal complexes. Coordination Chemistry Reviews, 88, 69–131.

Merkel, S., Kubo, A., Miyagi, L., Speziale, S., Duffy, T., Mao, H.K., and Wenk, H. (2006) Plastic deformation of $MgGeO_3$ post-perovskite at lower mantle pressures. Science, 311, 644–646.

Merklei, L.D., Spain, I.L., and Powell, R.C. (1981) Effects of pressure on the spectra and lifetimes of $Nd_xY_{1-x}P_5O_{14}$ and ruby. Journal of Physics C: Solid State Physics, 14, 2027–2038.

Meyer, H.-W., Marion, S., Sondergeld, P., Carpenter, M., Knight, K., Redfern, S., and Dove, M. (2001) Displacive components of the low-temperature phase transitions in lawsonite. American Mineralogist, 86, 566–577.

Mikenda, W., and Preisinger, A. (1981) N-lines in the luminescence spectra of Cr^{3+}-doped spinels (I) identification of N-lines. Journal of Luminescence, 26, 53–66.

Milberg, M.E., and Blair, H.D. (1977) Thermal Expansion of Cordierite. Journal of American Ceramic Society, 60, 7–8.

Miletich, R., Gatta, G.D., Willi, T., Mirwald, P.W., Lotti, P., and Merlini, M. (2014) Cordierite under hydrostatic compression: Anomalous elastic behavior as a precursor for a pressure-induced phase transition. American Mineralogist, 99, 479–493.

Mookherjee, M., Tsuchiya, J., and Hariharan, A. (2016) Crystal structure, equation of state, and elasticity of hydrous aluminosilicate phase, topaz-OH ($Al_2SiO_4(OH)_2$) at high pressures. Physics of the Earth and Planetary Interiors, 251, 24–35.

Morosin, B. (1972) Structure and thermal expansion of beryl. Acta Crystallographica Section B Structural Crystallography and Crystal Chemistry, 28, 1899–1903.

Motida, K., and Miyahara, S. (1970) On the 90° exchange interaction between cations (Cr^{3+}, Mn^{2+}, Fe^{3+} and Ni^{2+}) in oxides. Journal of the Physical Society of Japan.

Nagasundaram, N., Roper, G., Biscoe, J., Chai, J.W., Patterson, H.H., Blom, N., and Ludi, N. (1986) Single-Crystal Luminescence Study of the Layered Compound Potassium Dicyanoaurate. Inorg. Chem., 25, 2947.

Nakano, T., and Nakamura, E. (2001) Boron isotope geochemistry of metasedimentary rocks and tourmalines in a subduction zone metamorphic suite. Physics of the Earth and Planetary Interiors, 127, 233–252.

Navrotsky, A., and Hughes, L. (1976) Thermodynamic relations among olivine, spinel, and phenacite structures in silicates and germanates. V. The system MgO-“FeO”-GeO2. Journal of Solid State Chemistry, 16, 185–188.

Nestola, F., Ballaran, T.B., and Ohashi, H. (2008) The high-pressure *C*2/*c*–*P*2_1/*c* phase transition along the $LiAlSi_2O_6$–$LiGaSi_2O_6$ solid solution. Physics and Chemistry of Minerals, 35, 477–484.

Newton, R.C., and Kennedy, G.C. (1963) Some Equilibrium Reactions in the Join $CaAI_2Si_2O_8$-H_2O. Journal of Geophysical Research, 68, 2967–2983.

O’Bannon, E., and Williams, Q. (2017) Delocalization in Cr^{3+} luminescence of clinochlore: A pressure-induced transition from single-ion emission to pair emission. Journal of Physics and Chemistry of Solids, 109, 89–99.

O'Bannon, E.F., and Williams, Q. (2016a) A Cr^{3+} luminescence study of spodumene at high pressures: Effects of site geometry, a phase transition and a level-crossing. American Mineralogist, 101, 1406–1413.

O'Bannon, E.F., and Williams, Q. (2016b) Beryl-II, a high-pressure phase of beryl: Raman and luminescence spectroscopy to 16.4 GPa. Physics and Chemistry of Minerals.

Oganov, A.R., Gillan, M.J., and Price, G.D. (2005) Structural stability of silica at high pressures and temperatures. Physical Review B, 71, 64104.

Ohkura, H., Hashimoto, H., Mori, Y., Chiba, Y., and Isotani, S. (1987) The Luminescence and ESR of a Synthetic Emerald and the Natural Ones Mined from Santa Terezinha in Brazil. Japanese Journal of Applied Physics, 26, 1422–1428.

Okazaki, K., and Hirth, G. (2016) Dehydration of lawsonite could directly trigger earthquakes in subducting oceanic crust. Nature, 530, 81–4.

Ollier, N., Fuchs, Y., Cavani, O., Horn, A.H., and Rossano, S. (2015) Influence of impurities on Cr^{3+} luminescence properties in Brazilian emerald and alexandrite. European Journal of Mineralogy, 27, 783–792.

Ono, S. (1998) Stability limits of hydrous minerals in sediment and mid-ocean ridge basalt compositions: Implications for water transport in subduction zones. Journal of Geophysical Research, 103, 18253.

Origlieri, M.J., Yang, H., Downs, R.T., Posner, E.S., Domanik, K.J., and Pinch, W.W. (2012) The crystal structure of bartelkeite, with a revised chemical formula, $PbFeGe^{VI}(Ge_2{}^{IV}O_7)(OH)_2 \cdot H_2O$, isotypic with high-pressure $P2_1/m$ lawsonite. American Mineralogist, 97, 1812–1815.

Osmond, W. (1962) Indirect Magnetic Exchange Interactions in α-Fe_2O_3 and Cr_2O_3. Proceedings of the Physical Society, 79, 394.

Ota, T., Kobayashi, K., Katsura, T., and Nakamura, E. (2008) Tourmaline breakdown in a pelitic system: Implications for boron cycling through subduction zones. Contributions to Mineralogy and Petrology, 155, 19–32.

Pagé, L., Hattori, K., de Hoog, J.C.M., and Okay, A.I. (2016) Halogen (F, Cl, Br, I) behaviour in subducting slabs: A study of lawsonite blueschists in western Turkey. Earth and Planetary Science Letters, 442, 133–142.

Parsons, S. (2010) ECLIPSE - Program for masking high-pressure diffraction images and conversion between CCD image formats.

Patterson, H., Roper, G., Biscoe, J., Ludi, A., and Blom, N. (1984) Luminescence

studies of interacting metal complexes in two dimensions. Journal of luminescence, 32, 555–557.

Paul, D.K., Buckley, F., and Nixon, P.H. (1976) Fluorine and chlorine geochemistry of kimberlites. Chemical Geology, 17, 125–133.

Pauling, L. (1929) The principles determining the structure of complex ionic crystals. Journal of the American Chemical Society, 51, 1010–1026.

Pauling, L. (1930) The structure of the chlorites. Proceedings of the National Academy of Sciences, 16, 578–582.

Pawley, A. (1994) The pressure and temperature stability limits of lawsonite: implications for H_2O recycling in subduction zones. Contributions to Mineralogy and Petrology, 99–108.

Pawley, A., Redfern, S., and Holland, T. (1996) Volume behavior of hydrous minerals at high pressure and temperature: I. Thermal expansion of lawsonite, zoisite, clinozoisite, and diaspore. American Mineralogist, 81, 335–340.

Pawley, A.R., and Allan, D.R. (2001) A high-pressure structural study of lawsonite using angle-dispersive powder-diffraction methods with synchrotron radiation. Mineralogical Magazine, 65, 41–58.

Peacock, S. (1990) Fluid processes in subduction zones. Science, 248, 329–337.

Piermarini, G.J., Block, S., and Barnett, J.D. (1973) Hydrostatic limits in liquids and solids to 100 kbar. Journal of Applied Physics, 44, 5377–5382.

Piermarini, G.J., Block, S., Barnett, J.D., and Forman, R.A. (1975) Calibration of the pressure dependence of the R1 ruby fluorescence line to 195 kbar. Journal of Applied Physics, 46, 2774.

Plonka, A.M., Dera, P., Irmen, P., Rivers, M.L., Ehm, L., and Parise, J.B. (2012) β - diopside, a new ultrahigh-pressure polymorph of $CaMgSi_2O_6$ with six-coordinated silicon. Geophysical Research Letters, 39.

Poli, S., and Schmidt, M.W. (1995) H_20 transport and release in subduction zones : Experimental constraints on basaltic and andesitic systems. Journal of Geophysical Research, 299–314.

Poli, S., and Schmidt, M.W. (2002) Petrology of Subducted Slabs. Annual Review of Earth and Planetary Sciences, 30, 207–235.

Pommier, C.J.S., Denton, M.B., and Downs, R.T. (2003) Raman spectroscopic study of spodumene ($LiAlSi_2O_6$) through the pressure-induced phase change from $C2/c$ to $P2_1/c$. Journal of Raman Spectroscopy, 34, 769–775.

Pommier, C.J.S., Downs, R.T., Stimpfl, M., Redhammer, G.J., and Denton, M.B. (2005) Raman and X-ray investigations of $LiFeSi_2O_6$ pyroxene under pressure. Journal of Raman Spectroscopy, 36, 864–871.

Powell, R.C., and DiBartolo, B. (1972) Optical properties of heavily doped ruby. Physica Status Solidi (a), 10, 315–357.

Powell, R.C., Xi, L., Gang, X., Quarles, G.J., and Walling, J.C. (1985) Spectroscopic properties of alexandrite crystals. Physical Review B, 32, 2788–2797.

Prencipe, M., and Nestola, F. (2005) Quantum-mechanical modeling of minerals at high pressures. The role of the Hamiltonian in a case study: The beryl ($Al_4Be_6Si_{12}O_{36}$). Physics and Chemistry of Minerals, 32, 471–479.

——— (2007) Minerals at high pressure. Mechanics of compression from quantum mechanical calculations in a case study: The beryl ($Al_4Be_6Si_{12}O_{36}$). Physics and Chemistry of Minerals, 34, 37–52.

Prencipe, M., Scanavino, I., Nestola, F., Merlini, M., Civalleri, B., Bruno, M., and Dovesi, R. (2011) High-pressure thermo-elastic properties of beryl ($Al_4Be_6Si_{12}O_{36}$) from ab initio calculations, and observations about the source of thermal expansion. Physics and Chemistry of Minerals, 38, 223–239.

Prieto, A.C., Dubessy, J., and Cathelineau, M. (1991) Structure-Composition Relationships in Trioctahedral Chlorites: A Vibrational Spectroscopy Study. Clays and Clay Minerals, 39, 531–539.

Prieto, A.C., Boiron, M.C., Cathelineau, M., Mosser-Ruck, R., Lopez, J.A., and Garcia, C. (2003) Rythmic changes in crystal chemistry of trioctahedral Cr-chlorites and Cr entrapment: a SEM, EM and Raman study. Clay Minerals, 38, 339–352.

Putnis, A., and Bish, D.L. (1983) The mechanism and kinetics of Al, Si ordering in Mg-cordierite. American Mineralogist, 68, 60–65.

Qin, S., Liu, J., Li, H.-J., Zhu, X.-P., and Li, X.-D. (2008) In-situ high-pressure X-ray diffraction of natural beryl. Chinese Journal of high pressure physics, 22, 1–5.

Ransome, F.L. (1895) On lawsonite, a new rock-forming mineral from the Tiburon Peninsula, Marin County. University of California, Department of Geological Science Bull, 1, 301–312.

Rawashdeh-Omary, M.A., Larochelle, C.L., and Patterson, H.H. (2000) Tunable energy transfer from Dicyanoaurate(I) and Dicyanoargentate(I) donor ions to terbium(III) acceptor ions in pure crystals. Inorganic Chemistry, 39, 4527–4534.

Ringwood, A.E., and Seabrook, M. (1963) High-pressure phase transformations in

germanate pyroxenes and related compounds. Journal of Geophysical Research, 68, 4601–4609.

Robinson, K., Gibbs, G.V., and Ribbe, P.H. (1971) Quadratic Elongation : A Quantitative Measure of Distortion in Coordination Polyhedra. Science, 172, 567–570.

Rosenberg, P.E., and Foit, F.F. (1979) Synthesis and Characterization of alkali-free tourmaline. American Mineralogist, 64, 180–186.

Sánchez-Alejo, M.A., Hernández-Alcántara, J.M., Flores Jiménez, C., Calderón, T., Murrieta, H., and Camarillo García, E. (2011) Optical spectroscopy and high pressure on emeralds: synthetic and natural. Proceedings of SPIE, the International Society for Optical Engineering, 8011, 1–6.

Sangster, M.J.L., and McCombie, C.W. (1970) Calculation of phonon sidebands in emission spectra of V^{2+} and Ni^{2+} in MgO. Journal of Physics C: Solid State Physics, 3, 1498–1512.

Sano-Furukawa, A., Kagi, H., Nagai, T., Nakano, S., Fukura, S., Ushijima, D., Iizuka, R., Ohtani, E., and Yagi, T. (2009) Change in compressibility of -AlOOH and -AlOOD at high pressure: A study of isotope effect and hydrogen-bond symmetrization. American Mineralogist, 94, 1255–1261.

Santamaria-Perez, D., Thomson, A., Segura, A., Pellicer-Torres, J., Manjon, F.J., Cora, F., McColl, K., Wilson, M., Dobson, D., and McMillan, P.F. (2016) Metastable structural transformations and pressure-induced amorphization in natural $(Mg,Fe)_2SiO_4$ olivine under static compression: A raman spectroscopic study. American Mineralogist, 101, 1642–1650.

Sanz-Ortiz, M.N., Rodríguez, F., Hernández, I., Valiente, R., and Kück, S. (2010) Origin of the $^2E \leftrightarrow {}^4T_2$ Fano resonance in Cr^{3+} -doped $LiCaAlF_6$: Pressure-induced excited-state crossover. Physical Review B - Condensed Matter and Materials Physics, 81, 1–10.

Sato-Sorensen, Y. (1986) Measurements of the lifetime of the ruby R_1 line under high pressure. Journal of Applied Physics, 60, 2985–2987.

Scheidl, K.S., Gatta, G.D., Pippinger, T., Schuster, B., Trautmann, C., and Miletich, R. (2014) Static elasticity of cordierite I: Effect of heavy ion irradiation on the compressibility of hydrous cordierite. Physics and Chemistry of Minerals, 41, 579–591.

Schlenker, J.L., Gibbs, G.V., Hill, E.G., Crews, S.S., and Myers, R.H. (1977) Thermal expansion coefficients for indialite, emerald, and beryl. Physics and Chemistry of Minerals, 1, 243–255.

Schmetzer, K., and Eysel, H.H. (1974) Absorptions- and emissonsspektrum von V2+ /V3+ in beryllen. Zeitschrift für Naturforschung A, 29, 1458–1460.

Schmidt, M.W. (1995) Lawsonite : Upper pressure stability and formation of higher density hydrous phases. American Mineralogist, 80, 1286–1292.

Schmidt, M.W., and Poli, S. (1994) The stability of lawsonite and zoisite at high pressures: Experiments in CASH to 92 kbar and implications for the presence of hydrous phases in subducted lithosphere. Earth and Planetary Science Letters, 124, 105–118.

——— (1998) Experimentally based water budgets for dehydrating slabs and consequences for arc magma generation. Earth and Planetary Science Letters, 163, 361–379.

Scott, H.P., and Williams, Q. (1999) An infrared spectroscopic study of lawsonite to 20 GPa. Physics and Chemistry of Minerals, 26, 437–445.

Scott, H.P., Liu, Z., Hemley, R.J., and Williams, Q. (2007) High-pressure infrared spectra of talc and lawsonite. American Mineralogist, 92, 1814–1820.

Shapira, Y., and Bindilatti, V. (2002) Magnetization-step studies of antiferromagnetic clusters and single ions : Exchange , anisotropy , and statistics Magnetization-step studies of antiferromagnetic clusters and single ions : Exchange , anisotropy , and statistics. Journal of Applied Physics, 92, 4155–4185.

Shekhar Pandey, C., and Schreuer, J. (2012) Elastic and piezoelectric constants of tourmaline single crystals at non-ambient temperatures determined by resonant ultrasound spectroscopy. Journal of Applied Physics, 111.

Sheldrick, G.M. (2008) A short history of SHELX. Acta crystallographica. Section A, Foundations of crystallography, 64, 112–22.

Shen, Y., Riedener, T., and Bray, K.L. (2000) Effect of pressure and temperature on energy transfer between Cr^{3+} and Tm^{3+} in $Y_3Al_5O_{12}$. Physical Review B, 61, 11460–11471.

Shinn, M.D., and Tesar, A. (1992) Observation of temperature-dependent of Cr^{3+} - Nd^{3+} sensitization in fluoride glasses. Journal of Luminescence, 51, 189–195.

Shtukenberg, A., Rozhdestvenskaya, I., Frank-Kamenetskaya, O., Bronzova, J., Euler, H., Kirfel, A., Bannova, I., and Zolotarev, A. (2007) Symmetry and crystal structure of biaxial elbaite-liddicoatite tourmaline from the Transbaikalia region, Russia. American Mineralogist, 92, 675–686.

Skvortsova, V., Mironova-Ulmane, N., Trinkler, L., and Merkulov, V. (2015) Optical Properties of Natural and Synthetic Beryl Crystals. IOP Conference Series:

Materials Science and Engineering, 77, 12034.

Snytnikov, V.N., Stoyanovskii, V.O., Larina, T. V., Krivoruchko, O.P., Ushakov, V. a., and Parmon, V.N. (2008) Laser-induced luminescence of model Fe/Al_2O_3 and Cr/Al_2O_3 catalysts. Kinetics and Catalysis, 49, 291–298.

Stan, C. V., Dutta, R., White, C.E., Prakapenka, V., and Duffy, T.S. (2016) High-Pressure polymorphism of PbF_2 to 75 GPa. Physical Review B, 94, 24104.

Stan, C. V., Dutta, R., Cava, R.J., Prakapenka, V.B., and Duffy, T.S. (2017) High-Pressure Study of Perovskites and Postperovskites in the $(Mg,Fe)GeO_3$ System. Inorganic Chemistry, acs.inorgchem.7b00774.

Strasser, J., Yersin, H., and Patterson, H.H. (1998) Effect of high pressure on the emission spectrum of single crystals of $Tl[Au(CN)_2]$. Chemical Physics Letters, 295, 95–98.

Sugano, S., and Tanabe, Y. (1958) Absorption Spectra of Cr^{3+} in Al_2O_3 Part A. Theoretical Studies of the absorption Bands and Lines. Journal of the Physical Society of Japan, 13, 880–889.

Syassen, K. (2008) Ruby under pressure. High Pressure Research, 28, 75–126.

Tanabe, Y., and Sugano, S. (1954) On the Absorption Spectra of Complex Ions. I. Journal of the Physical Society of Japan, 9, 753–766.

Tanner, P.A., Zhou, X.J., Wong, W.T., Kratzer, C., and Yersin, H. (2005) Structure and spectroscopy of $Tb\ [Au\ (CN)_2]_3 \cdot 3H_2O$. Journal of Physical Chemistry B, 109, 13083–13090.

Taran, M.N., Langer, K., Platonov, a N., and Indutny, V. V (1994) Optical-Absorption Investigation of Cr^{3+} Ion-Bearing Minerals in the Temperature-Range 77-797-K. Physics and Chemistry of Minerals, 21, 360–372.

Taran, M.N., Ohashi, H., Langer, K., and Vishnevskyy, a. a. (2011) High-pressure electronic absorption spectroscopy of natural and synthetic Cr^{3+}-bearing clinopyroxenes. Physics and Chemistry of Minerals, 38, 345–356.

Tarashchan, A.N., Taran, M.N., Rager, H., and Iwanuch, W. (2006) Luminescence spectroscopic study of Cr^{3+} in Brazilian topazes from Ouro Preto. Physics and Chemistry of Minerals, 32, 679–690.

Tribaudino, M., Nestola, F., Prencipe, M., and Rundlof, H. (2003) A single-crystal neutron-diffraction investigation of spodumene at 54 K. Canadian Mineralogist, 41, 521–527.

Ulian, G., and Valdre, G. (2017) Effects of fluorine content on the elastic behavior of

topaz [$Al_2SiO_4(F,OH)_2$]. American Mineralogist, 102, 347–356.

Ullrich, A., Schranz, W., and Miletich, R. (2009) The nonlinear anomalous lattice elasticity associated with the high-pressure phase transition in spodumene: a high-precision static compression study. Physics and Chemistry of Minerals, 36, 545–555.

Van den Bleeken, G., and Koga, K.T. (2015) Experimentally determined distribution of fluorine and chlorine upon hydrous slab melting, and implications for F-Cl cycling through subduction zones. Geochimica et Cosmochimica Acta, 171, 353–373.

van Gorkom, G.G.., Henning, J.C.M., and van Stapele, R.P. (1973) Optical Spectra of Cr^{3+} Pairs in the Spinel $ZnGa_2O_4$. Physical Review B, 8, 955–973.

Van Uitert, L.G. (1967) Characterization of Energy Transfer Interactions between Rare Earth Ions. Journal of The Electrochemical Society, 114, 1048–1053.

Vink, A.P., Bruin, M.A. de, and Meijerink, A. (2000) Line broadening studies for Cr^{3+} pairs and single ions in different oxide lattices. Journal of Physics: Condensed Matter, 12, 8607–8615.

Vitale Brovarone, A., and Beyssac, O. (2014) Lawsonite metasomatism: A new route for water to the deep Earth. Earth and Planetary Science Letters, 393, 275–284.

Walker, G., Jaer, A. El, Sherlockb, R., Glynnb, T.J., Czaja, M., and Mazurak, Z. (1997) Luminescence spectroscopy of Cr^{3+} and Mn^{2+} in spodumene (LiAlSi2O6). Journal of Luminescence, 74, 278–280.

Walling, J.C., Peterson, O.G., Jenssen, H.P., Morris, R.C., and O'Dell, E.W. (1980) Tunable Alexandrite Lasers. IEEE Journal of Quantum Electronics, 16, 1302–1315.

Wamsley, P., and Bray, K. (1994) The effect of pressure on the luminescence of Cr^{3+}: YAG. Journal of luminescence, 59, 11–17.

Welch, M., and Marshall, W. (2001) High-pressure behavior of clinochlore. American Mineralogist, 86, 1380–1386.

Welch, M.D., and Crichton, W.A. (2005) A high-pressure polytypic transformation in type-I chlorite. American Mineralogist, 90, 1139–1145.

Werding, G., and Schreyer, W. (1996) Experimental studies on borosilicates and selected borates. Reviews in Mineralogy and Geochemistry, 33.1, 117–163.

Williams, Q., and Hemley, R.J. (2001) Hydrogen in the deep Earth. Annual Review of Earth and Planetary Sciences, 29, 365–418.

Williams, Q., and Jeanloz, R. (1985) Pressure shift of Cr^{3+} -ion-pair emission lines in ruby. Physical Review B, 31, 7449–7451.

Wood, D.L., and Nassau, K. (1967) Infrared Spectra of Foreign Molecules in Beryl. The Journal of Chemical Physics, 47, 2220–2228.

Wunder, B., Rubie, D., Ross II, C., Medenbach, O., Seifert, F., and Schreyer, W. (1993) Synthesis, stability, and properties of AlrSiO4 (OH) r: A fully hydrated analogue of topaz. American Mineralogist, 78, 285–297.

Xu, J., Kuang, Y., Zhang, B., Liu, Y., and Fan, D. (2016) Thermal equation of state of natural tourmaline at high pressure and temperature. Physics and Chemistry of Minerals.

Yamaga, M., and Henderson, B. (1991) Line shape and lifetimes of Cr3+ luminescence in silicate glasses. Physical Review B, 44, 4853–4861.

Yersin, H., and Riedl, U. (1995) Extreme pressure-induced shifts of emission energies in $M[Au(CN)_2]$ and $M_2[Pt(CN)_4]\cdot nH_2O$. compounds with low-dimensional and metal-metal interactions. Inorganic Chemistry, 34, 1642–1645.

Yoon, H.S., and Newnham, R.E. (1973) The elastic properties of beryl. Acta Crystallographica Section A, 29, 507–509.

Yu, H., and Clarke, D.R. (2002) Effect of codoping on the R-Line luminescence of Cr3+ -doped alumina. Journal of the American Ceramic Society, 85, 1966.

Zanazzi, P.F., Montagnoli, M., Nazzareni, S., and Comodi, P. (2007) Structural effects of pressure on monoclinic chlorite: A single-crystal study. American Mineralogist, 92, 655–661.

Zhang, R., Liou, J., and Shu, J. (2002) Hydroxyl-rich topaz in high-pressure and ultrahigh-pressure kyanite quartzites, with retrograde woodhouseite, from the Sulu terrane, eastern China. American Mineralogist, 87, 445–453.

Zheng, H., and Bailey, S.W. (1989) Structures of intergrown triclinic and monoclinic IIb chlorites from Kenya. Clays and Clay Minerals, 37, 308–316.

Zheng, W.-C. (1995) Determination of the local compressibilities for Cr^{3+} ions in some garnet crystals from high-pressure spectroscopy. Journal of Physics: Condensed Matter, 7, 8351–8356.